ALMOST DARK GALAXIES IN THE ALFALFA SURVEY

A Dissertation

Presented to the Faculty of the Graduate School

of Cornell University

in Partial Fulfillment of the Requirements for the Degree of

Doctor of Philosophy

by

Lukas Ross Leisman

August 2017

ALMOST DARK GALAXIES IN THE ALFALFA SURVEY

Lukas Ross Leisman, Ph.D.

Cornell University 2017

Star formation laws in galaxies appear to be tied to their available reservoirs of neutral hydrogen (H I). However, gas rich sources that are unable to convert their H I into stars would be difficult to detect in optical surveys, potentially dipping below detectable surface brightness limits in the most extreme cases. Theoretical predictions have been mixed as to whether these potential "(almost) dark," H I rich sources should exist. Thus, one of the main scientific drivers behind blind H I surveys is the search for optically dark, or almost dark, but gas-bearing dark matter halos.

The Arecibo Legacy Fast ALFA blind H I survey (ALFALFA) has detected over 30,000 clearly extragalactic sources, ~99% of which can be readily identified with probable stellar counterparts in public SDSS or DSS2 images. Here we present the results of follow up efforts to understand the other ~300 "dark" systems in ALFALFA, in a search for potential "almost dark" galaxies.

We expect most optically "dark" ALFALFA sources to be H I clouds stripped from galaxies in tidal interactions: tidal interactions are well known to play an important role in galactic evolution in group environments. Indeed, we confirm that over half of the "dark" systems in ALFALFA have a nearby neighbor (projected within 100 kpc and at a similar redshift) or are a clear tidal appendage. However, in at least two cases we found that candidate "dark" sources far from their nearest neighbor, were in fact part of large H I plumes with extents exceeding 1.4 deg (~600 kpc). These "dark" H I plumes constitute up to 40% of the

total H I mass in their host groups, potentially implying significant undetected H I in other groups, and greater prevalence of group scale interactions than previously thought. These observations demonstrate the importance of sensitive, wide field H I surveys in understanding the role of groups in galaxy evolution.

After removing tidal plumes, searching for (almost) dark galaxies requires extensive confirmation observations to remove spurious sources and OH Megamasers (the 18 cm line from rare molecular masers in luminous infrared galaxies redshifted into the ALFALFA bandpass). Further, since Arecibo does not resolve sources with its ~3.5′ beam, determining their nature requires detailed optical and H I follow up observations. Through a series of H I observations with the Jansky Very Large Array (VLA) and the Westerbork Synthesis Radio Telescope (WSRT), and optical observations with the WIYN 3.5m Telescope at Kitt Peak National Observatory, we have imaged 25 of the best ALFALFA (almost) dark candidates.

One early result of this imaging was the discovery of AGC 229385, a bright H I source (log ($M_{HI}/M_{\odot}$) = 8.7 at D=25 Mpc), but dark at the surface brightness limit of SDSS. Deep imaging revealed a very blue optical counterpart, with a peak surface brightness of μ_g = 26.4 mag/arcsec^2, an order of magnitude fainter than low surface brightness (LSB) galaxies detected in SDSS, placing it far off H I-stellar mass scaling relations. AGC 229385 has the largest accurately measured H I mass to light ratio of any known non-tidal, optically detected galaxy, M_{HI}/L_B = 38 $M_{\odot}/L_{\odot}$, and appears to lie far off the Tully-Fisher relation.

The H I and optical follow up observations also reveal that several of the "almost dark" sources are undetectable in current optical surveys not because they do not have stars, but because the stars are too spread out. These sources appear to be "ultra diffuse" galaxies (UDGs) - extreme galaxies with stellar masses

of dwarf galaxies, but radii similar to galaxies as large as the Milky Way. Most previously detected UDGs are in clusters, without detected H I. We broaden our definition of "almost dark" to search for more UDGs in ALFALFA, and present a sample of ~100 isolated ALFALFA galaxies that have similar stellar surface brightnesses, radii, and absolute magnitudes to optically selected UDGs in denser environments. Though these ALFALFA "H I-bearing ultra-diffuse" galaxies have similarly large radii for their stellar mass, they differ from cluster UDGs in that they are richer in atomic gas, bluer, and have more irregular morphologies. We present follow up H I and optical imaging of three of these H I-bearing UDGs, and show significant diffuse optical emission, large H I disks extending well beyond the stellar emission to radii of nearly 20 kpc, and evidence of ordered rotation. Indeed, comparison of this rotation to halo models may suggest that these sources have halo masses more consistent with dwarf galaxies, and may suggest they formed in high angular momentum halos.

BIOGRAPHICAL SKETCH

Lukas (Luke) Leisman grew up in Grand Rapids, Michigan as the oldest of 4. He received his Bachelors of Science in Physics from Calvin College in 2011, and Masters of Science in Astronomy from Cornell University in 2014. As a graduate student at Cornell, he spent most of his time in the "Camuy Cave" as a member of the extragalactic group (EGG) and the ALFALFA team, studying the evolution and origin of galaxies outside of the Milky Way using data from the Arecibo radio telescope in Puerto Rico. He also spent much of his time teaching, including involvement with the Cornell Prison Education Program. When he is not studying astronomy, he spends time with friends, contemplating the meaning of the universe, and exploring gorgeous Ithaca, NY. He also enjoys reading, writing, violin, sports, and understanding the relationship between his science and his Christian faith. He will be continuing his work teaching and studying galaxies as an Assistant Professor of Physics and Astronomy at Valparaiso University starting in the fall of 2017.

For my great cloud of witnesses: Katelyn, my family, and everyone else who kept me sane along the way.

ACKNOWLEDGEMENTS

It is impossible to adequately thank the many family, friends, teachers, and co-workers who have made this thesis possible. I was privileged to have the opportunity to even begin this journey, and have been blessed with a network of supportive individuals who have made this experience a success. To all those who have encouraged and supported me along the way, thank you.

Though this list is woefully incomplete, I would like to specifically acknowledge a number of individuals who have made invaluable contributions to this work:

- Katelyn Leisman – Katelyn is simply the best. From LaTeX help to keeping me on task to her constant encouragement, this thesis is what it is thanks to her.
- Mom, Dad, Hannah, Dorthea, and Hans – It is often said that people make sense in the context of their family. So much of who I am is shaped by their influence, love, and support. I succeed because of my family.
- Martha Haynes – One of the pieces of advice I received most often as a young grad student was that one's advisor makes or breaks one's graduate school experience, so choose wisely. I must say that Martha made my graduate school experience. She was an expert teacher, orchestrator, guide, and advocate. Martha is a skilled mentor who cares about her students – I very much appreciated her ability to guide and aid my thesis while still giving me the freedom to choose my own way, enabling and encouraging my growth as a scientist. I am lucky to have had her as an advisor.
- Riccardo Giovanelli – As my second advisor, Riccardo also helped make my graduate school experience. His thoughtful words of wisdom have

guided my approach to problem solving, and his incisive questions have been instrumental in the success of this work. More, his dry sense of humor and love of football (soccer) were essential components to every group meeting. It is also important to know that Riccardo is also the original discover of HI1232+20 (chapter 4), which we call "Coma P" after him, and deserves extensive credit for making the ALFALFA dataset a reality through his tireless hours of source extraction.

- Mike Jones – Mike and I joined the ALFALFA team at essentially the same time, which was lucky for me. Mike was a constant and patient sounding board for my crazy, stupid, and other ideas, and was an invaluable resource for working through problems. Mike was also an excellent office mate, and a good friend, and I will miss his excellent puns, British accent, and steady encouragement.

- Greg Hallenbeck – Greg has been an excellent mentor, and a great friend. He is the person most responsible for teaching me the ins and outs of H I data analysis, and has shared much code and documentation that were the produces of months and years of work. More, he opened his home to Katelyn and me on short notice, and has been our companion for innumerable board games, library book sales, discussions of the book of Enoch, and much more.

- Becky Koopmann and the undergraduate ALFALFA team –Becky and the other members of the undergraduate ALFALFA team – students and faculty – have been instrumental in my development as a teacher and as a scientist. I have learned so much from them. More, they have contributed significant effort to the analysis of data in this thesis, especially the undergraduate students David Bernal, Tayeb Zaidi, Catie Ball, Quinton Singer,

and Charlotte Martinkus to whom I own much thanks.

- Steven Janowiecki – Steven is quite possibly the person I have exchanged the most emails with over the course of this thesis – excited, frustrated, panicked, grateful – Steven's been the recipient of them all. This work would not be possible without Steven's optical expertise, and the long hours he's put in on ODI images. Chapter four especially would have been impossible without his efforts, which required a full paper's worth of work from both of us.

- The ALFALFA "almost darks" collaboration – the work of this thesis was a fully collaborative effort, and relied heavily on the comments, feedback, and aid of collaborators around the world. Thank you to Gyula (Josh) Józsa, John Cannon, Betsey Adams, John Salzer, Kathy Rhode, Hannah Pagel, Bill Janesh, and Kristy McQuinn for putting up with our monthly telecons and for their invaluable contributions to this work. I would especially like to thank Josh for his significant contribution to the WSRT data reduction, John C. for his constant encouragement and clear scientific thinking, and Betsey for her work on the proposals that shaped this data set, and for sharing helpful code, documentation, and advice.

- Kelley Hess, Kristine Spekkens, Manolis Papastergis, and Shan Huang – Each of these former Cornell EGGs has played a role in this thesis. Much of this thesis stands on Shan's work and Manolis's example. Kelley contributed significantly to chapter 3, and worked with me to derive complimentary science from our similar data. Kristine caught an important error in chapter 5, which resulted in much improved analysis.

- The entire ALFALFA collaboration for their tireless efforts observing, flagging, and extracting sources. My work with ALFALFA was made possible

only because I stand on the shoulders of others.

- The Cornell Astronomy Graduate Students – The Cornell Astronomy Department has been a good place to complete my work, in large part due to the other graduate students, who are great fun to be around and excellent colleagues. From GSPS to summer softball (go Big Bangers!) to random conversations in the hall, I am grateful for their support. I would especially like to give a special call out to Michael L., Riccardo P., Sean M., and Jason H. for their friendship and many useful conversations that contributed to the success of this thesis.
- Don Campbell and Richard Lovelace – I am thankful to Don and Richard for serving on my committee with Martha and Riccardo, and for reading this very long document and providing helpful and insightful feedback.
- NSF and the Brinson Foundation – this research was funded by NSF grants AST-0607007 and AST-1107390 and by grants from the Brinson Foundation.

TABLE OF CONTENTS

LIST OF TABLES

LIST OF FIGURES

CHAPTER 1

INTRODUCTION

Almost all known galaxies follow star formation "laws," that is, they show correlations between their gas content and the rate at which they form stars. These correlations convey important information about how galaxies form stars, constraining the mechanisms and speed with which galaxies can convert their gas into stars (see e.g., Krumholz, 2015).

Gas in galaxies usually is primarily made up of two components: atomic and molecular hydrogen. Atomic hydrogen is directly observable through the 21 cm (1420 MHz) H I spectral line which results from the energy difference between aligned and anti-aligned quantum spins of the electron and proton in hydrogen atoms. Molecular hydrogen (H_2) is rarely directly observable since it lacks a rotational dipole moment and thus is only rotationally excited at very high energies not found in the interstellar medium of galaxies. Instead it is usually observed through emission from a closely related molecule like carbon monoxide.

Observed star formation laws indicate that star formation in galaxies is tied to the amount of neutral hydrogen gas they contain (e.g., Huang et al., 2012a). For example, the total amount of neutral hydrogen gas in a galaxy is correlated with the star formation rate, indicating, unsurprisingly, that larger galaxies are able to form more stars. Further, the mass ratio of atomic hydrogen gas to stars in galaxies is correlated with their star formation rate, indicating that star formation in galaxies depends on the amount of the available gas. Thus, atomic hydrogen plays an important role in regulating star formation since it forms a reservoir of fuel with which to form stars.

However, molecular hydrogen is more directly associated with star formation in galaxies. Most star formation occurs in regions of comparatively high gas density, where the gas is dominated by dense molecular gas. In these regions stars form in giant molecular clouds, complex structures made up of H_2 and other molecules, and the star formation rate density is highly correlated with the molecular gas density (e.g., Kennicutt, 1998). This relationship has impressively little dependence on other factors like the metallicity of the gas or the density of the atomic hydrogen in the region.

However, in regions of comparatively low gas density, the fraction of molecular gas plummets, and the star formation rate appears to begin to depend on the density of atomic hydrogen, as well as a number of other factors, including the metallicity of the gas, the stellar surface density, and the distance from the center of the galaxy. This regime is much less well understood, due to the interdependency between the above factors, and the observational difficulty of observing galaxies at low gas and stellar density. In this low density, atomic hydrogen dominated regime it is not clear if star formation is most directly regulated by a trace amount of molecular gas (see e.g., Krumholz, 2013), or by the dynamics of the gas cloud as a whole (see, e.g., Elmegreen, 2015). Indeed, it is not even clear if stars can form at the lowest densities, or if there is a gas density threshold below which stars cannot form (e.g., Schaye, 2004).

This regime can be studied in the outskirts of galaxies, but is complicated by issues of stellar scattering, and dependency on galactocentric radius (see, e.g., Elmegreen & Hunter, 2016). However, it is perhaps best studied in galaxies that are entirely very low surface density: galaxies with high gas fractions that do not necessarily follow the typical star formation laws of high gas density

environments.

Theoretical models are mixed about the extent to which these low density galaxies should exist, and if they do, the extent to which they would be able to form stars (e.g. Verde et al., 2002; Taylor & Webster, 2005). In the most extreme cases, star formation in some galaxies may be sufficiently suppressed as to render them undetectable in stellar light (Salpeter & Hoffman, 1995). Indeed, recent simulations predict different numbers of optically "dark" galaxies depending on the parameters of their simulations (e.g., Crain et al., 2017).

Observationally, finding atomic hydrogen dominated, but nearly starless galaxies is challenging. Optical and infrared surveys that detect stellar light can be limited both by the lack of stars and low stellar densities. Small and moderate mass galaxies with sufficiently small stellar masses are not bright enough to be detected except in the very local volume. Yet perhaps more importantly, galaxies with sufficiently low stellar densities may escape optical detection if they are sufficiently low surface brightness (LSB), i.e., their stars are sufficiently spread out (e.g., Disney, 1976; Disney & Phillipps, 1983). This can be true even at large stellar masses, like the "crouching giants" Malin 1 (Bothun et al., 1987) and Malin 2 (Bothun et al., 1990) detected in deep photographic plate imaging, which have stellar masses $>10^{10} M_{\odot}$, but are nearly invisible at standard survey surface brightness limits. Indeed, Disney & Lang (2012) argue that we are trapped in a surface brightness window, unable to know whether or not there are substantial populations of highly extended galaxies lurking below optical surface brightness thresholds.

Further, blind surveys that can detect neutral hydrogen gas in galaxies via the 21 cm (1420 MHz) H I spectral line are comparatively limited in volume and

scope, since the collisionally excited hyperfine transition that produces the line only occurs once every ~100 years, and thus requires large gas reservoirs and very sensitive telescopes to be detected.

Moreover, H I observations are complicated by H I clouds that are not galaxies, i.e., that are not associated with dark matter halos. These clouds are commonly formed debris from tidal interaction, and can require expensive, high resolution H I observations to differentiate from candidate "dark" galaxies. Gas clouds detected in H I surveys have been misinterpreted as dark galaxies (see e.g., Minchin et al., 2005; Haynes et al., 2007; Duc & Bournaud, 2008).

In spite of these limitations, it is clear that H I rich, optically "dark" galaxies must be quite rare. More than 25 years after its initial detection, HI1225+01b (e.g Giovanelli & Haynes, 1989; Chengalur et al., 1995) remains the best candidate for an optically dark galaxy. The galaxy is in a binary pair of apparently kinematically independent H I sources of log $M_{\rm H\,I}/M_\odot$ ~9, one of which has a peak optical surface brightness of $\mu_B \sim 24$ mag asec^{-2}, while the other is dark down to a limiting magnitude of 28.3 mag asec^{-2} (Matsuoka et al., 2012). This source is perhaps the prototypical "dark" galaxy, but is complicated in that its relationship to its physically connected companion is somewhat unclear. Further, its origin, and whether it is a single instance or a broader piece of galactic evolution, remains unclear.

Indeed, state of the art blind H I surveys have not turned up substantial additional populations of H I rich "dark" galaxies. Doyle et al. (2005) do not find any clear dark galaxies in the wider area HIPASS survey with the Parkes Telescope in Australia, and Haynes et al. (2011) report that only 1% of detections in the Arecibo Legacy Fast ALFA (ALFALFA) Survey (where ALFA is the Arecibo

L-band Feed Array 7-pixel receiver at Arecibo Observatory) with the Arecibo Telescope in Puerto Rico cannot be readily identified with a clear, well detected stellar counterpart, and most of these are likely tidal debris.

However, a number of these detections without visible stellar counterparts may be gas rich galaxies that do not obey typical star formation laws. Though they are rare, identifying and characterizing these extreme galaxies is important for understanding star formation in atomic hydrogen dominated, low density regimes where well understood star formation laws break down. Thus, the aim of this thesis is to identify and characterize these potential "dark" galaxies in ALFALFA to better understand star formation in atomic hydrogen dominated regimes, and to better understand where star formation laws break down. It examines the contribution of ALFALFA to the search for "dark" and "almost dark" galaxies, and what they tell us about extragalactic star formation.

We note that throughout this thesis we will refer to truly starless galaxies as "dark" galaxies, and galaxies with sufficiently low stellar density so as to be undetectable at current optical and infrared survey limits as "almost dark" galaxies. Further, we distinguish between these and candidate "dark" sources, i.e., H I detections without confirmed stellar counterparts, which are candidates to be either "dark" or "almost dark" galaxies if confirmed.

We also note that in low mass satellite galaxies, the ultraviolet radiation field and feedback processes are expected to effectively quench star formation rendering them optically undetectable. However, some of these lowest mass galaxies may still contain detectable amounts of atomic hydrogen (see e.g., Giovanelli et al., 2010; Adams et al., 2013; Benítez-Llambay et al., 2017). Indeed, blind H I surveys have detected H I in halos with dynamical masses of $\sim 10^7 - 10^8 M_\odot$ near

the edges of the local group (e.g., Giovanelli et al., 2013; Janesh et al., 2017). Galaxies with these masses are too small to be detected beyond the local volume, which means that search for starless minihalos is complicated by the presence of the Milky Way, and that peculiar velocities make determine distances to sources without detected stars impossible. Thus, while this regime of "dark" galaxies constitute an important and active area of study, this thesis will limit its discussion to higher mass halos detectable beyond the local volume.

The thesis is outlined as follows: ALFALFA, the largest blind H I survey to date by volume, is described in more detail in Chapter 2. Chapter 2 also gives an overview of ALFALFA's contribution to the question of "dark" and "almost" dark galaxies. Chapters 3, 4, and 5, then give specific, detailed examples of lessons learned from the study of almost dark follow up observations.

Specifically, in chapter 3 we present ALFALFA H I observations of a well studied region of the Leo Cloud, which includes the NGC 3227 group and the NGC 3190 group. We detect optically dark H I tails and plumes with extents potentially exceeding 600 kpc, well beyond the field of view of previous observations. These H I features contain ~40% of the total H I mass in the NGC 3227 group and ~10% of the NGC 3190 group. We also present interferometric maps which show the complex morphology of the the extended emission in the NGC 3227 group. We comment on previously proposed models of the interactions in these group and the implications for the scale of group processing through interactions. Motivated by the extent of the H I plumes, we place the H I observations in the context of the larger loose group, demonstrating the need for future sensitive, wide field H I surveys to understand the role of group processing in galaxy evolution.

In chapter 4 we describe the discovery and follow-up observations of HI1232+20, a system of three extragalactic ALFALFA "dark" sources. We present deep optical imaging and H I synthesis maps of this system, which show that the source with the highest H I flux (AGC 229385) is associated with a very low surface brightness optical counterpart (peak surface brightness of ~26.4 mag/arcsec^2 in g'), while the other two sources have no detected optical counterparts. AGC 229385 has the largest well measured H I mass-to-light ratio of an isolated object: $M_{HI}/L_{g'}$=46 $M_\odot/L_\odot$, and has an H I mass of $7.2\times10^8 M_\odot$. The other two H I sources (with H I masses 2.0×10^8 and $1.2\times10^8 M_\odot$) without optical counterparts have upper limit surface brightnesses of 27.9 and 27.8 mag/arcsec^2 in g', and lower limits on their gas mass-to-light ratio of $M_{HI}/L_{g'}$ >57 and >31 $M_\odot/L_\odot$. The system appears to be quite isolated; though it lies relatively close in projection to the Virgo Cluster, velocity flow models indicate that it is located substantially beyond Virgo. We discuss a variety of possible formation scenarios for the HI1232+20 system, and suggest that these H I sources may represent both sides of the threshold between "dark" starless galaxies and galaxies with stellar populations.

In chapter 5 we present a sample of 115 very low optical surface brightness, highly extended, H I-rich galaxies carefully selected from the ALFALFA survey that have similar optical absolute magnitudes, surface brightnesses, and radii to recently discovered "ultra-diffuse" galaxies (UDGs). However, these systems are bluer and have more irregular morphologies than other UDGs, are isolated, and contain significant reservoirs of H I. We find that while these sources have normal star formation rates for H I selected galaxies of similar stellar mass, they have very low star formation efficiencies. We further present deep optical and H I synthesis follow up imaging of three of these H I-bearing ultra-diffuse

sources. We measure H I diameters extending to ~40 kpc, but note that while all three sources have large H I diameters for their stellar mass, they are consistent with the H I mass - H I radius relation. We further analyze the H I velocity widths and rotation velocities for the unresolved and resolved sources respectively, and find that the sources appear to inhabit halos of dwarf galaxies. We estimate spin parameters, and suggest that these sources may exist in high spin parameter halos, and as such may be potential H I-rich progenitors to the ultra-diffuse galaxies observed in cluster environments.

The thesis then concludes with a summary and discussion of the many future contributions ALFALFA and related follow up efforts can make to the question of the role of "dark" and "almost" dark galaxies in galaxy formation and in the universe as a whole.

CHAPTER 2

ALFALFA'S CONTRIBUTION TO THE SEARCH FOR "ALMOST DARK" GALAXIES

2.1 Introduction

The Arecibo Legacy Fast ALFA Survey (ALFALFA; e.g., Giovanelli et al., 2005; Haynes et al., 2011) is a blind H I survey which aims to provide a census of local H I bearing galaxies using the 305m Arecibo single-dish radio telescope in Puerto Rico. Enabled by the installation of the 7 feedhorn 21-cm Arecibo L-band Feed Array (ALFA), which greatly increased the speed at which Arecibo could map the sky at frequencies corresponding to emission from the H I line, ALFALFA covers ~7000 deg^2 of sky visible to Arecibo ($0^\circ < \delta < 36^\circ$) outside of the galactic plane (over 1/6th of the sky) out to a redshift of 0.06 (which corresponds to a recessional velocity of ~17,000 km s^{-1} or distances of ~250 Mpc). ALFALFA completed survey observations in October 2012 after 4,742 hours of observing over the span of 8 years, and anticipates publication of its final catalog in late 2017.

With over ~30,000 extragalactic detections in its current working catalog (based on 70% of the total survey area), ALFALFA represents a major step forward in blind H I surveys. Prior to ALFALFA, the most recent wide-area blind H I survey was the H I Parkes All-Sky Survey (HIPASS; e.g., Barnes et al., 2001), carried out with the 13-beam Multibeam receiver at Parkes Observatory in Australia. Since the Parkes telescope is fully steerable, HIPASS has the advantage that it covers a significantly large sky area (~21,000° at $\delta < 2^\circ$). However, due to Arecibo's much larger collecting area, ALFALFA represents a factor of 10 in-

crease in sensitivity over HIPASS, and a factor of 4 increase in resolution. Thus ALFALFA samples a larger volume of space, and its final catalog will contain nearly an order of magnitude more than the 4315 extragalactic sources in the final HIPASS catalog.

Thus, as the first blind H I survey to sample a cosmologically significant volume, ALFALFA has produced over 100 peer reviewed publications,[i] providing robust measurements of the number of H I bearing galaxies (the H I mass, width, and diameter functions) and relationships between H I and other properties of H I-bearing galaxies (e.g., Martin et al., 2010; Papastergis et al., 2011; Huang et al., 2012a).

Maximizing the scientific returns from ALFALFA depends on its ability to reliably associate detections with signals at other wavelengths. Importantly, much of the ALFALFA survey area overlaps with the sky coverage of wide field optical surveys like the Sloan Digital Sky Survey (SDSS; York et al., 2000) and the second generation Digitized Sky Survey (DSS2). This, coupled with the large improvement in resolution (3.5′ versus HIPASS's 15′) allows for significantly more accurate identification of H I detections with likely stellar counterparts. More, it allows for much better identification of H I detections without stellar counterparts – potential candidates to be illusive starless or nearly starless "dark" galaxies.

In this chapter we examine the ~1% of clearly extragalactic sources detected by ALFALFA without identified likely stellar counterparts. These turn out to be a heterogeneous collection of sources with a number of different physical origins. We first describe the details of the ALFALFA data and follow up data

[i]See the ALFALFA publications website, `http://egg.astro.cornell.edu/alfalfa/pubs.php`, for a list.

collection, along with the process of identifying stellar counterparts, in section 2.2. We then discuss the details of the ALFALFA "darks" sample in section 2.3, and discuss observational complications related to "dark" sources in section 2.4. We present results from the ALFALFA survey's search from "dark" galaxies in sections 2.5, 2.6, and 2.7, and present a summary of ALFALFA's contribution to the search for "dark" galaxies, in part as motivation for the remaining chapters of this thesis, in section 2.8.

2.2 Observations and Data

2.2.1 ALFALFA Data

We derive the ALFALFA "darks" sample from the 70% ALFALFA catalog (Jones et al., 2016), which contains sources from the first 70% of the ALFALFA observations. A number of other authors have detailed the ALFALFA observations, data reduction, and catalog products (e.g. Giovanelli et al., 2005; Haynes et al., 2011). Here we summarize these, with specific emphasis on the parts of the process relevant to the detection of "dark" sources.

The ALFALFA survey was conducted in "drift scan" mode, with the feed arm positioned at azimuths of ~180° or 360°, in contrast to the traditional total power switching mode used in single pixel confirmation observations (section 2.2.2). The data are bandpass subtracted, and then each beam and polarization are interactively examined to flag radio frequency interference (RFI) and regions characterized by lower quality data due to, e.g., standing waves, receiver instabilities, etc. This labor intensive process is important for creating a clean and

well characterized data set to search for potential optically dark sources.

The flagged drift scans are then gridded into cubes 2.4° on a side, with a spectral bandwidth from -2000 to 18,000 km s^{-1}, with an effective spectral resolution of 10 km s^{-1} after Hanning smoothing (note: the cubes are split into four subcubes of 1024 spectral channels each for easy processing). Each cube is then rebaselined and flat-fielded both spatially and spectrally, accounting for any remaining systematic variations due to, e.g., strong continuum fluctuations.

Sources are extracted in a two step process. Sources are first identified using an automatic matched filtering algorithm (Saintonge, 2007), and then each cube is examined channel by channel to confirm the matched filtering results, check for missed sources, and interactively fit source parameters. This interactive process improves the definition of the source parameters, as well as the reliability and completeness of the catalog over simple automated extraction.

A key aspect of the interactive source fitting is the visual identification of optical counterparts in SDSS and DSS2 images. Visual identification of optical counterparts is necessary due to Arecibo's 3.5′ beam, which is significantly more extended than most galaxies. Further, visual identification is essential, since extended nearby sources are often shredded into a number of sources by the SDSS pipeline, and to prevent misidentifications with stars or distance background sources.

The ALFALFA team member chooses a most likely optical counterpart comparing this publicly available optical data to the ALFALFA H I data, and any other available auxiliary or spectra information in e.g., the NASA Extragalactic Database. The team member considers proximity to the H I centroid, signal-to-

noise, redshift, color, and morphology to inform his or her scientific judgment in assigning the optical counterpart. In most cases the assignment is obvious. In other cases (two nearby galaxies within the beam, significant optical-H I centroid offsets, very low surface brightness sources, etc.) the assignment is less clear (see Haynes et al., 2011 for further detailed discussion and examples). In these cases the source is examined by multiple team members, and discussed to determine the most likely candidate, or if there is not a likely stellar candidate. Thus it is important to emphasize that each cross match is the most likely stellar counterpart, and may be incorrect for any given source. Still, even with this caveat in mind, the ALFALFA team identifies a likely stellar counterpart in ~99% of cases.

2.2.2 LBW Data

In order to confirm the reality and better understand the reliability of ALFALFA "dark" sources, we executed a number of pointed observing programs using the single beam L-band Wide (LBW) receiver (e.g., A2707, A2752, A3067, A3122). These programs used a well established procedure for confirmation of ALFALFA sources, consisting of 3 minute ON-OFF total power pairs with the interim correlator covering a 25 MHz bandwidth with 9-level sampling. We used doppler tracking and center the spectra at the frequency appropriate to each target's ALFALFA redshift. Given the longer integration times and higher sensitivity of the LBW system with respect to ALFA, the corroborating observations yielded S/N ratios 2-3 times higher than that of the ALFALFA observations, definitively determining the reality and H I spectra of the sources.

In total, we observed 265 "dark" candidates, confirming ~65% of sources with no optical counterpart and S/N>6.5 in the ALFALFA survey, but only 4/99 dark sources with S/N<6.5. We discuss these results and the reliability of ALFALFA "dark" sources in detail in section 2.4.1.

In addition to understanding the reliability of the ALFALFA "dark" sources, these observations were important in determining which sources to study in greater detail with high spatial resolution synthesis observations (section 2.2.3). Though ALFALFA detections can be confirmed in a matter of minutes with Arecibo, higher resolution observations with interferometers take several hours per source. For example, AGC 123216 (S/N=7.5 in ALFALFA, Figure 2.1) was confirmed with a 3 minute ON-OFF LBW observation, and then imaged for 24 hours with the Westerbork Synthesis Radio Telescope and 90 minutes with the WIYN 3.5m at KPNO. Thus, LBW confirmation of the best candidates was critical to justify the additional large investment of time with other telescopes to study their nature in greater detail.

2.2.3 H I Synthesis Data

In order to better understand the nature of these sources, we conducted exploratory observations using the Westerbork Synthesis Radio Telescope (WSRT) and the Karl G. Jansky Very Large Array (VLA). Specifically, we observed 15 of the most extreme candidate $M_{\rm H\,I}/{\rm L}$ systems in the 2013 version of the ALFALFA catalog during 2014 and 2015 with WSRT (program R13B/001; P.I. Adams). These sources were selected to cover a range of masses, velocity widths, and environments to better understand the range of potential "dark" sources in

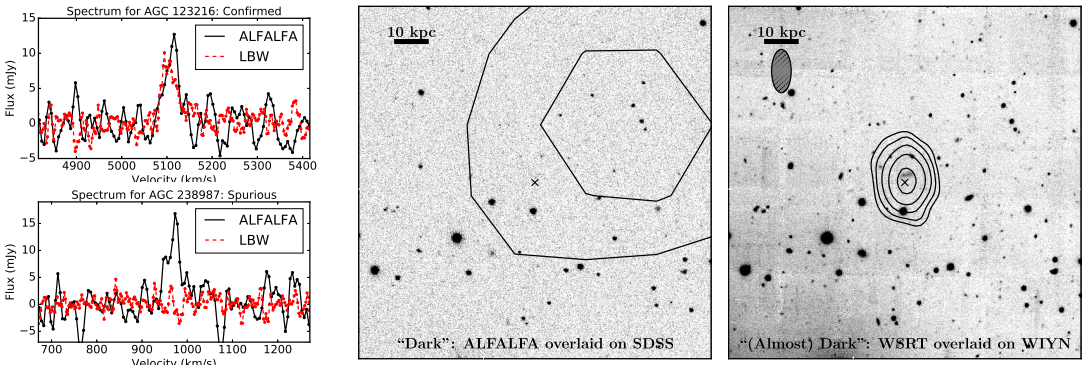

Figure 2.1: The process of finding extremely rare "almost dark," H I rich, vLSB galaxies: Left top: Detection spectra of the ALFALFA "dark" source AGC123216 (S/N=7.5) in black, and the confirming LBW spectrum overplotted in red. The ALFALFA spectrum for this source looks very similar to the spurious ALFALFA detection shown below. Center: ALFALFA flux density contours overlaid on a 5′ square SDSS g-band image of AGC 123216 (centered on the known position from WSRT imaging), showing the lack of visible optical emission, and the size and positional uncertainty of the ALFALFA beam. Right: WIYN 3.5m pODI g-band image of AGC 123216, (45-minute exposure) with WSRT column density contours at 4, 8, 16, 32, 64, and 128 $\times 10^{19}$ cm^{-2} overlaid in black, showing an extended H I disk centered on a barely visible stellar population.

ALFALFA. These sources were observed with on-source integration times of 1-2×12h, a 10 MHz bandwidth centered on the ALFALFA central H I velocity, two polarization products, and 1024 channels. This resulted in a sufficiently broad range of line-free channels for continuum subtraction (about 1900 km s^{-1}) and a minimum velocity resolution of 4.1 km s^{-1} (after Hanning smoothing).

AGC 229398 was discovered shortly after the first proposal was submitted, and was observed with a single 12h pointing and similar configuration under a second program with WSRT (program R14A/015; P.I. Leisman).

We observed five sources with the VLA under a pilot program 13A-028 (legacy ID AC1116; P.I. Cannon), the results of which are discussed in Cannon et al. (2015). We observed one source, AGC 219533 under program 14B-243 (legacy ID AL891; P.I. Leisman) for two 3 hour blocks in C configuration during December 2014. We additionally observed three sources under program 15B-170

(legacy ID AL941; P.I. Leisman) for two hours each in D configuration and two 3 hour blocks each in C configuration in 2015-2016. These observations used the WIDAR correlator in dual polarization mode with a single 1024 channel 8 MHz wide sub-band, giving a native channel width of 1.7 km s^{-1}.

The data reduction processes for both the WSRT and VLA observations are described elsewhere. The WSRT data reduction followed the process described in Janowiecki et al. (2015) and Leisman et al. (2016), using an automated Python pipeline wrapped around the MIRIAD (Sault et al., 1995) data reduction software (see Serra et al., 2012; Wang et al., 2013). After automatic RFI flagging and primary bandpass calibration, the pipeline iteratively deconvolves the data with the CLEAN algorithm in order to apply a self-calibration, and then applies the calibration solution and continuum subtraction in the visibility domain. The data is then inverted and cleaned down to the rms noise.

The VLA reduction process follows standard procedures as detailed in Cannon et al. (2015) and Leisman et al. (2017). We use the CASA (Common Astronomy Software Applications; McMullin et al., 2007) package to flag and calibrate the visibilities, applying continuum subtraction in the uv plane. We image the data using the CASA CLEAN task using a multiscale clean and a Briggs robust weighting of 0.5.

We create moment zero (representing total intensity) and moment one (representing velocity fields) maps of each source by first creating 3σ masks on cubes smoothed to 2x the beam, and applying these masks to the unsmoothed cube. We then sum along the velocity axis or take the peak flux along that axis to find the moment zero and moment one maps respectively.

2.2.4 Optical Data

In addition to studying the H I gas in the ALFALFA "dark" candidates, determining the extent to which they are "dark," requires deep optical observations to search for faint stellar counterparts. We use the one degree imager (ODI) on the WIYN 3.5m at Kitt Peak National Observatory to observe dark sources. Specifically, we observed 15 sources with eight or nine dithered 300 second exposures in both the g' and r' filters during observing runs in October 2013, March 2014, April 2014, and October 2016 (runs during 2015 were clouded out). Five additional sources were recently observed during March 2017, and represent ongoing and future work, as discussed in chapter 7.

During the 2013 and 2014 observing runs the ODI camera was only partially populated and had a significantly restricted field of view. Thus for these runs we refer to the camera as partial ODI or pODI. More recent observing runs involve the fully upgraded camera, and make use of the full field of view. The details of the reduction are described below in section 4.2.2.

2.3 The ALFALFA "Darks" Sample

2.3.1 The Parent "Darks" Sample

The ALFALFA "darks" sample is all ALFALFA sources not identified with SDSS/DSS optical counterparts (OCs) during the initial ALFALFA processing, and with S/N>6.5, i.e., sources identified as "code 1" (most reliable) during the ALFALFA processing. There are 281 "code 1" candidate "dark" sources in the

ALFALFA 70% catalog. However, as discussed in section 2.4.1, the reliability of ALFALFA dark sources as a function of signal-to-noise is significantly worse than for ALFALFA sources with optical counterparts, because most spurious detections do not align with optical counterparts. To date, 60 are confirmed to be spurious by LBW, and another 33 have S/N<9 and still need to be observed by LBW.

For optical uniformity, we removed six sources from the sample that are not within the SDSS footprint. Further, another 11 detections are in optical fields that contain a bright foreground galaxy or a bright star, rendering it impossible to determine if there is a real "dark" source (5 more have a bright star within the beam, but may still be identifiable; given this uncertainty, we have left them in the sample). Six more sources were identified with likely OCs later in processing.

This leaves a sample of 198 real candidate "dark" sources, of which 33 are low S/N and still need to be confirmed. However, counting these sources is not straightforward. The extraction algorithm that produces the ALFALFA catalog is optimized for point sources, and therefore resolves extended features into multiple density peaks. Thus, many of the dark sources in the ALFALFA catalog are not unique sources, but rather are density peaks in extended physical systems. Specifically there are 19 systems containing more than one dark source. These 19 systems contain a total of 108 sources, thus leaving 109 independent "dark" H I systems in ALFALFA. We make use of both methods of counting as appropriate for our analysis.

2.3.2 The Synthesis Sample

With a 3.5′ beam, Arecibo is unable to resolve detected dark sources. Thus, higher resolution observations with interferometers are necessary to confirm the location of the gas, as well as to unambiguously distinguish between ordered, galaxy like gas distributions and messy tidal distributions. Further, high resolution synthesis observations are able to measure the velocity distribution of the gas, constraining whether the gas motions are consistent with the presence of a dark matter halo.

Yet, interferometric observations are expensive, and are thus limited to smaller subsamples, selected to be representative of the larger population of ALFALFA "dark" sources. Given the uncertainties in the nature of these objects, we obtained high resolution observations of "dark" sources through a series of exploratory observations. The sources in these observations were selected to focus on sources that were not clearly tidal in origin, and to cover a wide range of parameter space.

Our initial pilot program with the VLA (program 13A-028) and more comprehensive program with the WSRT (program R13B/001) selected the most extreme $M_{\rm H\,I}$/L sources discovered in the ALFALFA survey (i.e., the brightest sources without optical detections) in a range of environments, including isolated sources, those offset from early type galaxies, and sources that appeared to be companions to other gas bearing galaxies. The sources ranged in H I mass between ~$10^{7.5}$-$10^{10} M_{\odot}$, in redshift between ~1000 and ~8000 km s^{-1}, and in velocity width between ~25 km s^{-1} and 200 km s^{-1} (though most had widths <60 km s^{-1}).

Subsequent observing programs focused on individual interesting sources (VLA program 14B-243 and WSRT program R14A/015), filling out the sample. Program 15B-170 was specifically selected to observe the best, most isolated candidate 'dark" sources, and thus was important for reaching the conclusions discussed in section 2.4.3 and 2.5.

It is important to note that these sources included in the initial exploratory observations were not selected in a complete or uniform way, and depended significantly on telescope availability and available information at the time. Because the ALFALFA "darks" sample is defined based on the initial lack of an OC assignment, some of the objects not identified with OCs during initial processing were, after subsequent examination, later identified with low surface brightness objects. Thus a few objects included in the synthesis samples now have an officially assigned OC in the ALFALFA catalog, but are no longer a candidate "dark" source.

Moreover, each subsequent sample was selected from a dynamic and growing catalog. The initial pilot sample discussed in Cannon et al. (2015) was initially defined from the ALFALFA 40% survey, and the final sample included sources from the ALFALFA 57% catalog. The WSRT (R13B001) sample was selected during the completion of A70.

However, thought the synthesis source selection is neither uniform nor complete, they cover a wide range of parameter space in terms of mass, velocity width, and isolation, thus giving a good picture of the darks population as a whole.

2.4 Special Issues Pertaining to "Dark" Sources

The selection of a small subset of sources without apparent optical counterparts (OCs) from the larger ALFALFA survey necessitates special care in establishing the reality of the detection. Here we address three specific issues that need to be dealt with to establish the candidacy of an ALFALFA "dark" source, namely, the reliability of the sources (section 2.4.1), confusion with spectral lines that are not H I (section 2.4.2), and misidentification due to large centroid offsets (section 2.4.3).

2.4.1 Reliability

One major barrier to analysis of potential "dark" candidates is the issue of reliability, i.e., whether or not the detections are real. Most of the area in a blind survey covering 7000 deg^2 is void of sources at z< 0.1, so spurious noise spikes in the data are most likely unaligned with viable OCs. Thus, sources without OCs need to be treated with extra caution. While the reliability of ALFALFA source extraction via an automatic matched filtering algorithm is ~95% at SN>6.5 (Saintonge, 2007), and visually inspected sources with matching polarizations and a probable optical counterpart are more than ~99% reliable (Haynes et al., 2011), reliability plummets for sources without OCs.

We have carried out a number of confirmation programs with the single pixel LBW receiver at Arecibo (section 2.2.2) to confirm the reality of ALFALFA "dark" sources. We have observed 166 sources with S/N>6.5, and have only confirmed ~65%. Unsurprisingly, the confirmation rate of dark sources in AL-

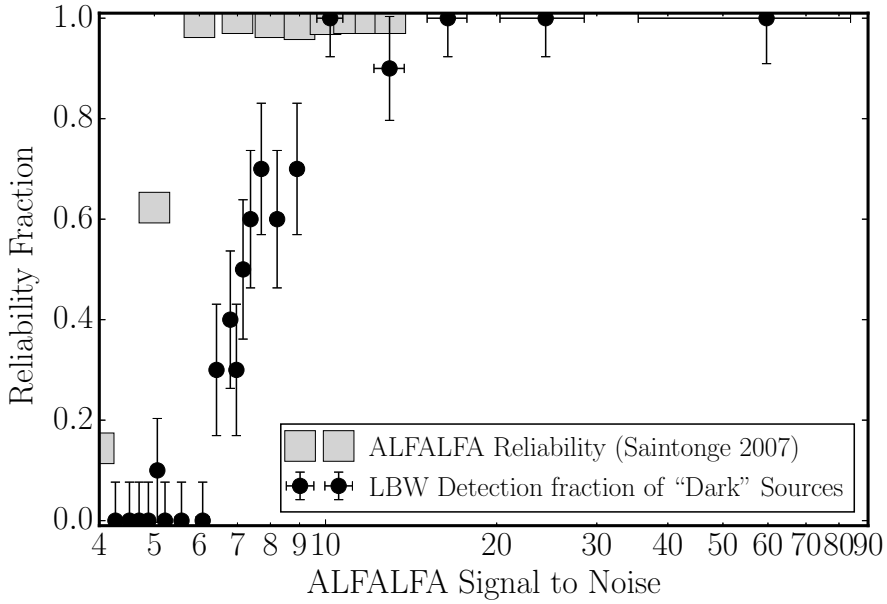

Figure 2.2: Reliability of ALFALFA sources from Saintonge (2007), with the LBW detection fraction as a function of ALFALFA S/N for sources without OCs overplotted as a proxy for reliability. While ALFALFA sources with OCs are highly reliable above SN~6.5, sources without OCs are only highly reliable above S/N~10.

FALFA is a strong function of signal-to-noise. For all LBW observations of ALFALFA galaxies without OCs, we detect 98% sources with ALFALFA S/N >10, 51% for 6.5<S/N<10, and only 4% sources with no OC and ALFALFA S/N<6.5.

Figure 2.2 compares the detected fraction of "dark" sources observed with LBW compared with the reliability of ALFALFA sources from simulations from (Saintonge, 2007), showing the transition between unreliable detections at low signal-to-noise, and reliable detections at high signal-to-noise. While sources with OCs are quite reliable for S/N>6.5, ALFALFA sources without optical counterparts, require a S/N>10 to reach a similar reliability.

We thus restrict our analysis to sources with S/N>10, or sources that have been confirmed with pointed LBW observations.

2.4.2 OH Megamasers

Hydroxel megamasers (OHMs) are strong OH line sources associated with luminous and ultra-luminous infrared galaxies, which are extreme starburst galaxies formed in major galaxy mergers. OHMs are a rare phenomenon in the local universe - only $\lesssim$120 known OHMs at z<0.265 (Darling & Giovanelli, 2002; Suess et al., 2016). The main 18 cm OH line emits at a rest frequency that can redshift into the spectrum of blind H I surveys (Briggs, 1998). Specifically, the 18-cm line occurs at rest frequencies of 1665 and 1667 MHz, which is redshifted into the ALFALFA observing band at redshifts of 0.16<z<0.25 (Haynes et al., 2011). Given the difference in appearance of a galaxy at z~0.2 and z<0.06, coupled with the size of the ALFALFA beam, OHMs can be first identified as "dark" sources in the ALFALFA survey.

Suess et al. (2016) perform optical spectroscopic follow up of 194 ambiguous H I sources in the 40% ALFALFA catalog that are also detected in the Wide Field Infrared Survey Explorer (WISE), and find 6 OHMs in ALFALFA. In addition the ALFALFA "darks" efforts presented here have identified 5-8 sources that are reasonable candidate OHMs, due to their asymmetric line profiles (due to the doublet nature of the 18 cm OH line), and potential optical counterparts that look like z~0.2 galaxies. These candidates will require spectroscopic confirmation, but if confirmed, could better constrain our understanding of the frequency of this rare phenomenon.

Additionally, one source in the WSRT synthesis observations, AGC 249507 appears to be a point source associated with a small, distant looking galaxy. This, coupled with AGC 249507's line profile strongly suggest that AGC 249507 is a OHM.

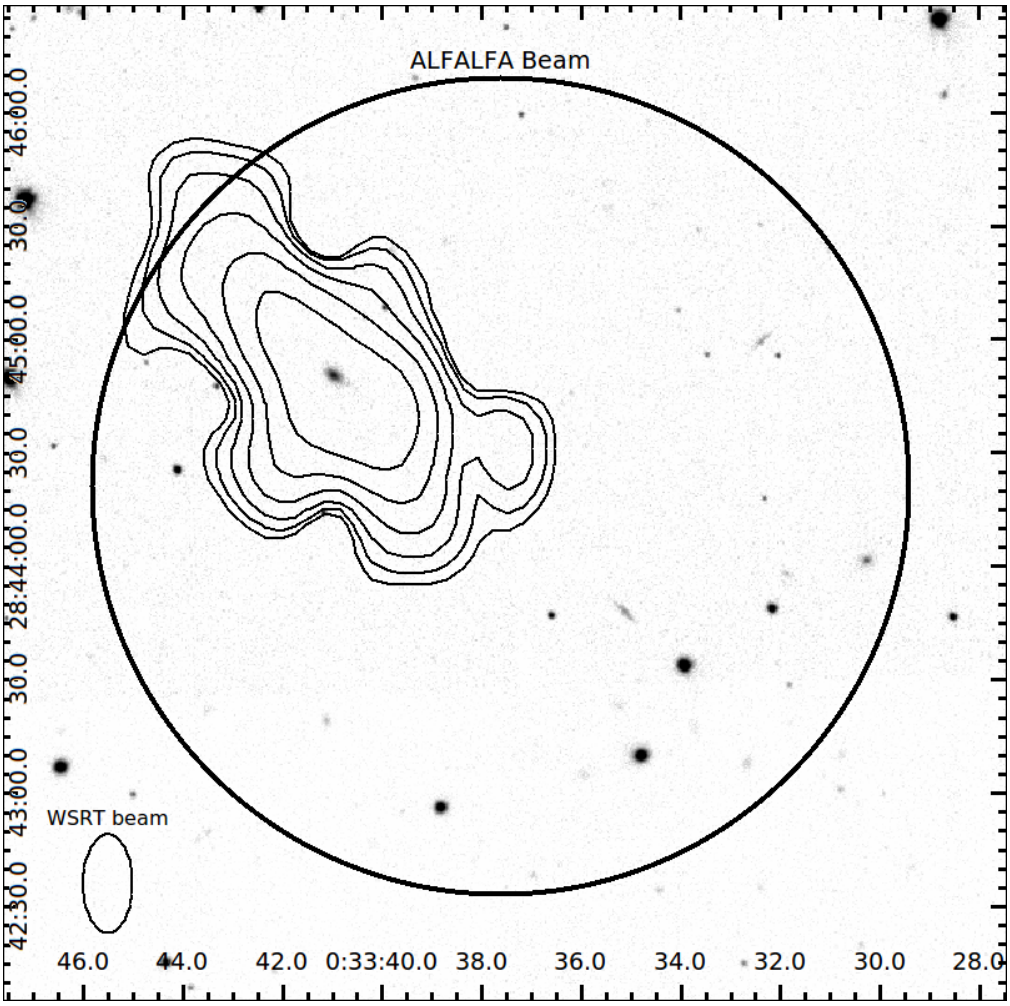

Figure 2.3: AGC 102983, an example "dark" galaxies identified with an OC located offset from the ALFALFA centroid. The image shows WSRT contours overlaid on an SDSS g-band image, compared with the ALFALFA beam. The source identified by the WSRT contours as the optical counterpart was originally considered to be an unlikely match, due to its offset from the H I centroid, and unusually compact and red morphology.

2.4.3 HI centroid Offsets

The distribution of offsets between the measured H I position in ALFALFA and the position of the stellar counterpart is determined by three things: 1) the pointing accuracy of Arecibo, 2) statistical localization due to noise in the data, and 3) physical offsets between the H I and the stars.

As was the case with the reliability/ reality of the sources, in a survey of

30,000 sources, a few sources will lie far from the beam center. Some of these are still identified as the likely counterpart, due to their size, or properties (blue, star forming, lower surface brightness). However, others, especially sources that do not look like standard nearby galaxies or those in crowded fields may instead be incorrectly identified as "dark" galaxies.

Figure 2.3 shows an example source that we have followed up with WSRT or the VLA, that turned out to be optically bright sources at significant offset. Sources like these represent ~20% of the ALFALFA dark sources with synthesis observations. These observations, coupled with a reexamination of the optical fields suggest that another 9-12 additional ALFALFA "dark" systems will similarly be associated with offset, odd stellar counterparts.

While these sources are not "dark" galaxies, they can be very interesting sources for further detailed study. For example, one of these appears to be one of the most extended H I sources known, with an H I disk that extends more than 30 optical scale lengths, similar to NGC 3741 (e.g., Begum et al., 2005).

2.5 On the Lack of Isolated Dark Sources

Figure 2.4 shows the projected separation in kpc to the nearest neighbor with a measured redshift within 500 km s^{-1} for confirmed or high S/N ALFALFA "dark" sources contrasted with the distribution for the full ALFALFA sample. The figure shows a marked difference between the two samples. While the median nearest neighbor separation for an ALFALFA source is >400 kpc, most ALFALFA dark sources are at a nearest neighbor separation <100 kpc, and almost all "dark" sources have separations <300 kpc.

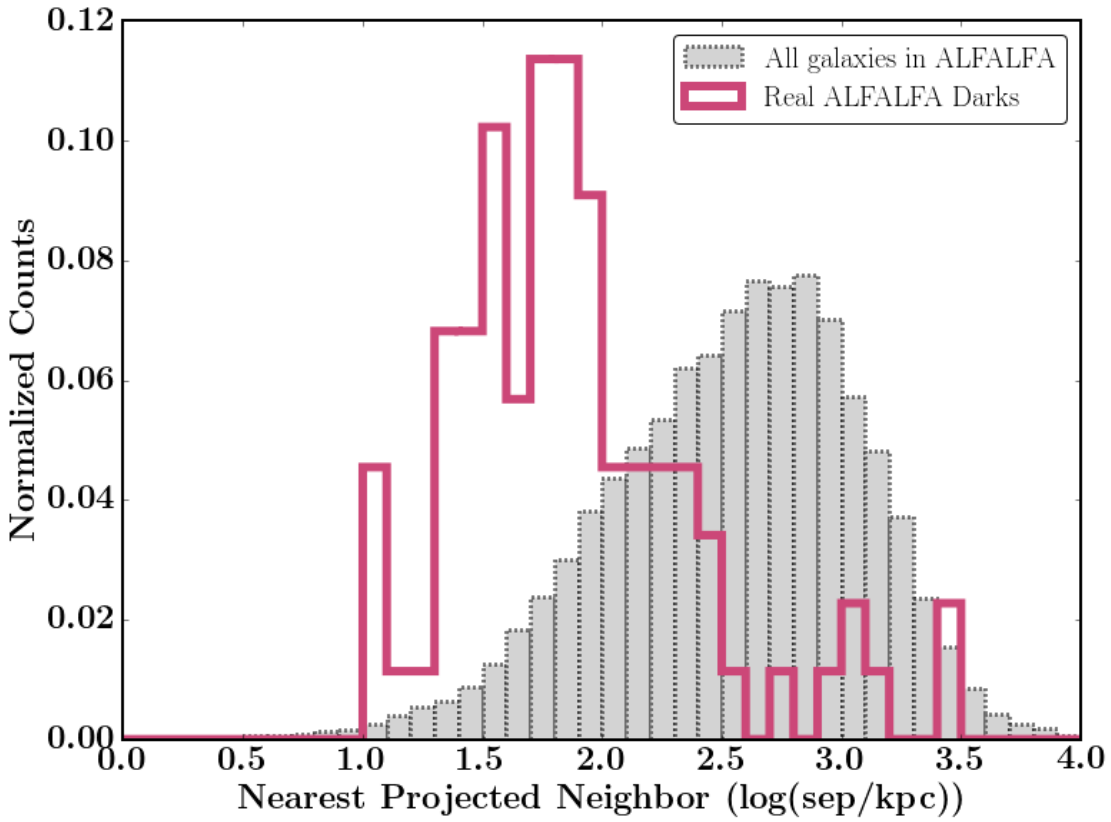

Figure 2.4: Projected separation to the nearest neighbor with a recessional velocity within 500km s^{-1} of confirmed ALFALFA sources without apparent optical counterparts (open pink bars) compared with the full ALFALFA 70% catalog (shaded grey bars). The ALFALFA "dark" sources are at significantly smaller spacial separation than the overall sample.

The large concentration of dark sources at small nearest neighbor separations implies that the most common mechanism for creating "dark" H I sources is an environment dependent process; it depends on proximity to other sources. This result is, perhaps, expected. H I clouds pulled from their host galaxy in tidal interactions are well known to be a common occurrence (e.g., Hibbard et al., 2001b). Further, galactic interactions have been shown to create occasional tidal dwarf galaxies, though the details and ubiquity of this process is a matter of debate. We discuss these sources at small separations in section 2.6.

Perhaps more surprising, however, is the dearth of sources at average or

large nearest neighbor separations. Of real sources without optical issues (like a bright star), there are only 23 sources with nearest neighbor separations of >275 kpc. Twelve of these have been assigned OCs after interferometric follow up (see section 2.4.3) or through more detailed examination (note: three of these ended up being classified as "ultra-diffuse" galaxies and are discussed in detail in chapter 5). Three more high separation sources are confirmed or very likely OHMs, and five others may have a potential strange looking OC or may be OHMs.

This leaves only three candidate isolated "dark" sources, AGC 124412, AGC 229360, and AGC 229361. AGC 124412 is in the fall sky, outside the coverage of the SDSS spectroscopic survey, and thus may have nearby gas-poor companions without measured redshifts. It also may have an unconfirmed offset OC. AGC 229360 and AGC 229361 are a gas rich, apparently optically dark pair, and are discussed in chapter 7.2. While locally isolated, they are projected to the north of the Virgo cluster, and may be at significantly smaller distances than estimated from their radial velocities, and thus significantly less isolated (for a detailed discussion of the effect of the Virgo cluster on distance uncertainties, see chapter 4). Yet these sources, together with the HI1232+20 system (with a projected separation of ~274 kpc to its nearest neighbor within 500 km s^{-1}, see chapter 4) represent the best candidate isolated "dark" sources in ALFALFA. However, each of these sources has a more likely explanation, i.e., is likely to not be a truly isolated "dark" galaxy.

While theoretical models have long toyed with the model of isolated H I disks that are stable against collapse (without another source to perturb the gas and start initial collapse, the disk could exist in a long lived, stable configura-

tion, e.g., Verde et al., 2002), the ALFALFA data strongly suggest that this is not the case. It appears that there are not massive isolated dark disks of atomic hydrogen at the sensitivity limits of ALFALFA.

2.6 Dark Sources with Nearby Companions

As described above, almost all potential "dark" candidates appear to have a nearby companion. In many cases the companion is another source detected in ALFALFA at a similar redshift, and may even appear to be connected in the ALFALFA data cubes. Given the low resolution and complicated beam response of the ALFA receiver, this does not necessarily mean that the sources are physically connected by a stream of H I, but synthesis observations have shown that this is the most likely scenario. In other cases the "dark" source appears offset from a source without detected gas, but optical redshift or morphological information suggest a connection. While it is sometimes not clear if the the offset is real or is an outlier in the Arecibo pointing distribution, pointed LBW observations have confirmed the offset in almost all cases.

Thus, the presence of a nearby companion significantly complicates the interpretation of the ALFALFA data, and necessitates synthesis follow up observations to confirm the nature of each source. In addition to confirming the association of the sources, it is important to distinguish between a large number of possible formation scenarios. Most of the sources are likely to be H I clouds that are debris from tidal forces during galaxy galaxy interactions, but they may also be H I clouds removed by ram pressure stripping in denser environments, or actual gravitationally bound galaxies, whether Tidal Dwarf Galaxies formed from

galaxy interactions, or H I disks in central halos that happen to have a nearby companion.

Below we present example sources from three main "apparent category of "dark" source with a nearby companion: an H I plume from an interaction with a gas rich companion, a H I cloud connected to a gas poor companion, and apparent gravitationally supported galaxies. These examples showcase their heterogeneous nature, and demonstrate the likely science to be obtained from future observations.

2.6.1 Tidal Tails and Appendages

The vast majority of ALFALFA dark sources appear to be appendages to large, H I rich galaxies, and presumably formed through the action of tidal forces during the close passage of two galaxies (e.g., Toomre & Toomre, 1972). As a perturbing galaxy passes by a gas rich galaxy, it pulls more strongly on gas near the edge of the galaxy, gravitationally removing that gas from its host and forming a potentially very long H I tail. This phenomenon has been observed in many systems (e.g., Hibbard et al., 2001a), and many of the "dark" tidal H I plumes detected in ALFALFA are well studied (see, e.g., Haynes, 1979, 1981; Stierwalt et al., 2009; Lee-Waddell et al., 2012).

While the magnitude of this effect depends on the separation between the interacting galaxies and the timescale of the interaction (i.e., the galaxies' relative velocities and rotation directions), the process of removing gas from a galaxy via tidal forces during galaxy-galaxy interactions can be surprisingly ubiquitous. Duc & Bournaud (2008) show that tidal tails can be created even in very

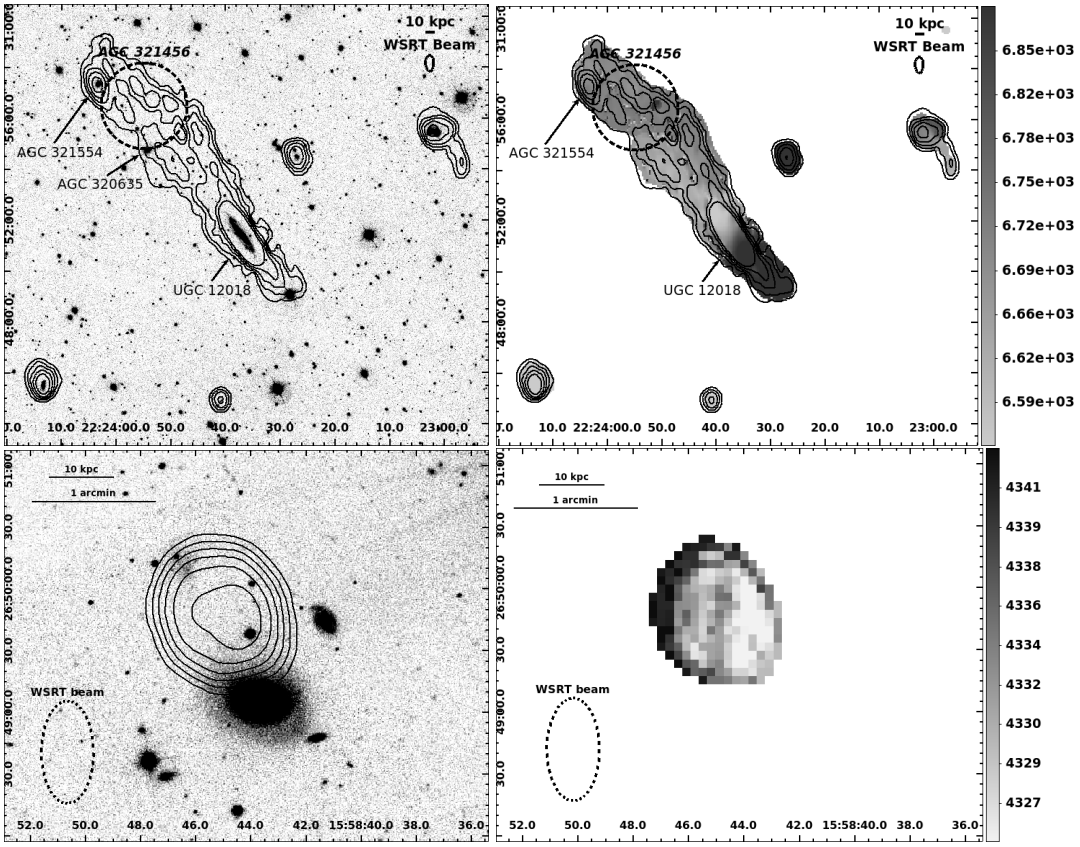

Figure 2.5: Examples of two large H I appendages that appear to have resulted from the interaction of group galaxies. The left hand panels show the H I moment 0 column density contours from WSRT overlaid on SDSS g-band images, and the right hand panels show H I velocity fields derived from WSRT imaging for AGC 321456 (top) and AGC 251402 (bottom), where the colorbar represents recessional velocities in km s^{-1}. The dashed circles show the size and location of the ALFALFA beam for the original source detection for AGC 321456. These sources demonstrate some of the diversity of starless H I clouds formed from galaxy-galaxy interactions.

high speed interactions, and that these tidal interactions are the best explanation for a claimed "dark" galaxy in the Virgo cluster, data supported by ALFALFA observations (e.g., Haynes et al., 2007; Kent et al., 2007).

Indeed, of the "dark" sources observed as part of the exploratory H I observations with WSRT and the VLA, at least six appear to be H I clouds formed from tides in interacting systems, even though the observations were selected to avoid likely tidal systems.

Four of these turned out to be part of large H I plumes clearly connected to gas rich galaxies. Three are in the NGC 3226/7 system, which is discussed in detail in chapter 3. Another source, AGC 321456 is shown in Figure 2.5. AGC 321456 appears to be a ~200 kpc H I bridge connecting two H I rich galaxies. The nature of the connection between AGC 321456 and its companions, the early type galaxy AGC 320635, the irregular galaxy AGC 321554, and the spiral UGC 12018 was not clear in the ALFALFA data. WSRT observations show complex, extended structure that contains more than 1/4 of the total gas mass of UGC 12018. WSRT observations also show an additional H I tail in the NE part of this gas rich galaxy group, and the ALFALFA flux measurements suggest that there is more intergalactic gas at low column density. These results serve to reinforce the importance of wide field mapping for understanding the evolution of groups, a concept discussed in great detail in chapter 3.

Other morphologically messy, extended H I plumes appear to be associated with early type galaxies (ETGs) without detected H I. While the gas is less clearly connected to the ETGs, it is likely to have a similar physical origin. One example, AGC 208602, is discussed in detail in Cannon et al. (2015). Another, AGC 251402 is shown in the bottom panel of Figure 2.5. Like the other tidal plumes observed with exploratory H I interferometry, the connection between AGC 251402 and its companion sources was unclear from the ALFALFA data. WSRT data reveals that the H I emission appears to be directly between a very low surface brightness stellar stream, and a gas poor, apparently early type galaxy. Interestingly, the ETG shows strong evidence of nuclear star formation in SDSS spectroscopy, but is not detected in H I emission. Figure 2.5 also shows that the H I velocity field shows some velocity gradient consistent with the measured redshifts of the optical sources, and will be an interesting source

to further model forms of gas removal from galaxies. AGC 251402 shows the diversity in potential interacting systems that can result in starless H I clouds.

While these examples all appear to have tidal origins, it is important to note that not all disturbed intergalactic gas plumes necessarily result from tides. In environments where the intergalactic medium is sufficiently dense, gas can be stripped from galaxies as they move through the medium. Indeed, multiple "dark" H I sources detected in ALFALFA are most likely the result of this ram pressure stripping (Kent et al., 2009), and others are less clear (Koopmann et al., 2008).

2.6.2 Candidate Tidal (Dwarf) Galaxies

While most ALFALFA "dark" detections with nearby companions are part of large H I plumes connected to neighboring galaxies, a handful of these detections appear to have ordered, disk-like H I morphologies in deep synthesis observations, and are clearly associated with very low surface brightness optical counterparts in deep WIYN imaging. Further, most of these sources have ordered velocity fields, with some evidence of rotation. The origins of these ordered sources are unclear, however, the presence of a reasonably nearby companion suggest that their evolution may be linked to their environment.

One possibility is that these sources are formed from the gaseous material removed from interacting galaxies. Dubbed tidal dwarf galaxies (TDGs)[i] these "second generation" galaxies are characterized by their lack of dark matter and their higher metalicities in comparison to first generation classical dwarfs (see, e.g., Duc, 2012). Moreover, Duc et al. (2014) find that evolved TDGs have low

central surface brightnesses and extended radii relative to typical dwarfs, and TDGs in the early stages of formation may also have small stellar populations relative to their H I masses. Thus, the high gas fraction ALFALFA "almost dark" sources may be candidate TDGs.

However, the frequency with which TDGs occur, and their contribution to the overall dwarf galaxy population is highly contested (e.g.,Bournaud & Duc, 2006; Dabringhausen & Kroupa, 2013). Indeed, there are only $\lesssim$20 TDGs that are widely considered to be authentic, since it requires numerous corroborating observations to constrain, e.g., the the gas kinematics, metallicity, and star formation properties and thus demonstrate the likelihood of a tidal origin (Lee-Waddell et al., 2016).

Lee-Waddell et al. (2012), Lee-Waddell et al. (2014), and Lee-Waddell et al. (2016) use deep imaging with the Canada–France–Hawaii Telescope (CFHT) and the Giant Metrewave Radio Telescope (GMRT) to explore ALFALFA dark tails in three nearby groups. They find that most low mass group objects are either classical dwarf irregular galaxies or short-lived tidal knots, but also find four likely TDGs between the three groups.

The WSRT synthesis observations find four additional "almost dark" sources that may be TDGs, including AGC 123216 (Figure 2.1). While the relatively narrow velocity widths, low surface brightnesses, and colors of these sources seem consistent with the TDG hypothesis, deep spectroscopic observations and further detailed modeling will be necessary to determine if the origin of these sources and their extreme properties is indeed a result of the interaction of larger

[i]We note that the definition of "dwarf" varies significantly throughout the literature; though the ALFALFA detections contain large quantities of H I ($>10^9 M_\odot$ in some cases), we expect galaxies formed through tidal interactions to be dark matter poor, and thus still to reside in "dwarf" dark matter halos.

"Dark" Sources with Deep Follow Up Imaging: A Heterogeneous Collection

Category/Type	$N_{sources}$
Sources that are not galaxies (OHMs, strange tidal clouds)	8
Sources at large offsets from ALFALFA centroid	5
Isolated H I-bearing ultra-diffuse galaxies (chapter 5)	3
Non-isolated UDGs/ potential Tidal Dwarf Galaxies	3
(Almost) dark galaxies in the direction of Virgo	3
Other (almost) dark galaxies	2

Table 2.1: Categories of "dark" and "almost dark" sources with deep H I and optical imaging, and the number of observed sources in each category.

galaxies.

2.7 Other Synthesis Observations: A Heterogeneous Population

As discussed above, most sources with confirming synthesis observations are not galaxies, or are candidate TDGs. Table 2.1 lists the wide ranging categories fit by the candidate (almost) dark sources, including sources with unusual optical counterparts that were previously unnoticed due to their large offsets from the ALFALFA H I centroid (section 2.4.3), and the candidate TDGs (section 2.6.2).

Three sources have identified very low surface brightness counterparts, barely visible in SDSS data after close examination. Including ALFALFA sources that are just barely detected in SDSS data significantly increases the size of the "almost darks" sample; there are many sources with peak surface brightnesses near 24-25 mag arcsec^{-2}. These sources appear to optically match properties of recently reported "ultra-diffuse" galaxies, and are discussed further in chapter 5 and Leisman et al. (2017).

Several other poorly understood dark sources appear in the rough direction of the Virgo cluster. Dark clouds in the Virgo cluster have been the subject of intense discussion. Kent et al. (2007) give an initial catalog of ALFALFA dark sources near the central region of the Virgo cluster, and present follow up analysis in Kent et al. (2009) and Kent (2010). These sources appear to have a wide range of origins, but much about the clouds in this direction is still unknown. Part of the difficulty is that recessional velocities in the direction of Virgo do not give reliable measures of distance, since peculiar velocities in this region can exceed 1000 km s^{-1}. Still, in addition to published enigmas in this region like HI1225+01 (discussed in chapter 1), the synthesis observations for this work contribute several other sources to this discussion, including AGC 226178 (Cannon et al., 2015), the HI1232+20 system (chapter 4), and the AGC 229360/229361 system that is the subject of much ongoing and future work.

An additional source that appears to be a pair of 40 kpc disks, only one of which is detected with a peak g-band surface brightness around 27 mag $arcsec^{-2}$.

Thus, the ALFALFA "almost darks" observations have uncovered a heterogeneous population, united by their large H I content.

2.8 Lessons and Conclusions from the Search for Dark Galaxies

The ALFALFA Survey represents a large step forward in sensitivity, resolution, and volume of blind H I surveys. These improvements in sensitivity and resolution allow for an improved understanding of the low surface brightness universe, especially the most extreme sources that contain an optically undetectable

number of stars. Characterization of these extreme sources is ongoing, but the main conclusions from this efforts are:

- Finding sources without optical counterparts is difficult. Sources that are not readily identified with OCs are significantly less reliable than sources with likely OCs (by $\sim 3\sigma$), and local blind H I line surveys can be contaminated by OH megamasers at z~0.2. Further, the size and pointing uncertainty of the Arecibo beam allow for unusual sources at large offsets from the fitted H I centroid to escape initial identification.
- There does not appear to be a substantial population of isolated dark sources. Of the handful of confirmed candidate "dark" sources, almost all have a more likely explanation. For a handful of sources, especially at the higher ALFALFA redshifts, more detailed observations will be necessary to conclusively rule out the "dark" galaxy hypothesis, but our observations thus far suggest that they are more likely than not to have an alternative explanation.
- Almost all "dark" sources have a nearby companion, and some are apparently tidally connected to parent galaxies over ~300 kpc away (see chapter 3).
- There does appear to be a handful of sources that are extreme "almost dark" galaxies. Perhaps the best example is AGC 229385, which is discussed in great detail in chapter 4.
- While ALFALFA only measures a handful of sources below optical detection limits, it detects many sources with surface brightnesses near the detection limit of SDSS. These "ultra-diffuse" sources are discussed in detail in chapter 5. Observationally, these sources link the darkest ALFALFA

sources and higher surface brightness populations, but whether there is a physical connection remains to be seen.

CHAPTER 3

ALFALFA AND WSRT IMAGING OF EXTENDED H I FEATURES IN THE LEO CLOUD OF GALAXIES

3.1 Introduction

Most galaxies at z~0 can be found in group environments (e.g. Tago et al., 2008), where evidence of tidal interactions and gas stripping are particularly prevalent (e.g. Hibbard et al., 2001a; Hibbard et al., 2001b). These observations of ongoing tidal interactions suggest that galaxies can undergo significant morphological evolution in the group environment, possibly playing a major role in the morphology-density relation (e.g. Postman & Geller, 1984; Bekki & Couch, 2011; Hess & Wilcots, 2013).

H I observations can give direct evidence of the fundamental role of group processing in galaxy evolution, tracing the recent interaction history of group galaxies (e.g. Yun et al., 1994). However, while the inner interactions of merging galaxies have been observed in detail, (e.g. Rand, 1994), H I studies covering the full extent of interactions in groups are difficult to execute due to the need for high sensitivity over wide fields; wide field H I surveys have been limited in resolution and sensitivity, and interferometric studies have been limited to the field of their primary beam.

Still, H I mapping on the group scale is important for understanding the ubiquity of these interactions, the fraction of gas involved, and the interaction time scales (e.g., Serra et al., 2015), which in turn constrain the impact of tidal

This chapter is an adapted version of the published article Leisman et al. (2016).

processing in groups on galactic evolution, relative to other processes, like the decrease in cold gas accretion (Sancisi et al., 2008).

The Arecibo Legacy Fast ALFA (Arecibo L-band Feed Array) survey (ALFALFA; Giovanelli et al., 2005) provides high sensitivity, unbiased, wide field maps of H I in the local volume, and has traced the atomic gas distribution in a variety of local groups (Stierwalt et al., 2009; Lee-Waddell et al., 2012; Lee-Waddell et al., 2014).

Here we present the ALFALFA data on a well studied loose group in the Leo Cloud, known to show significant evidence of interaction. The ALFALFA data are not limited to an arbitrary region on the sky, allowing us to search for additional structures and constrain the cold gas fraction outside stellar disks over the full ~9 Mpc^2 physical region. These data reveal substantial intragroup cold gas, demonstrating the power of sensitive, wide field H I mapping.

We summarize prior work on this group in section 3.2 and present our observations in section 3.3. We present our results in section 3.4, discuss the group context in section 3.5 and conclude in section 3.6. For all calculations, the assumed cosmology is $H_0 = 70\ \mathrm{kms^{-1}Mpc^{-1}}$, $\Omega_m = 0.3$, and $\Omega_\Lambda = 0.7$.

3.2 Placement in the Cosmic Web

3.2.1 The NBG 21-6 Region

Figure 3.1[i] shows the distribution of galaxies in the constellation Leo, between heliocentric recessional velocities of v_h=700 km s^{-1} and 1700 km s^{-1}. The pri-

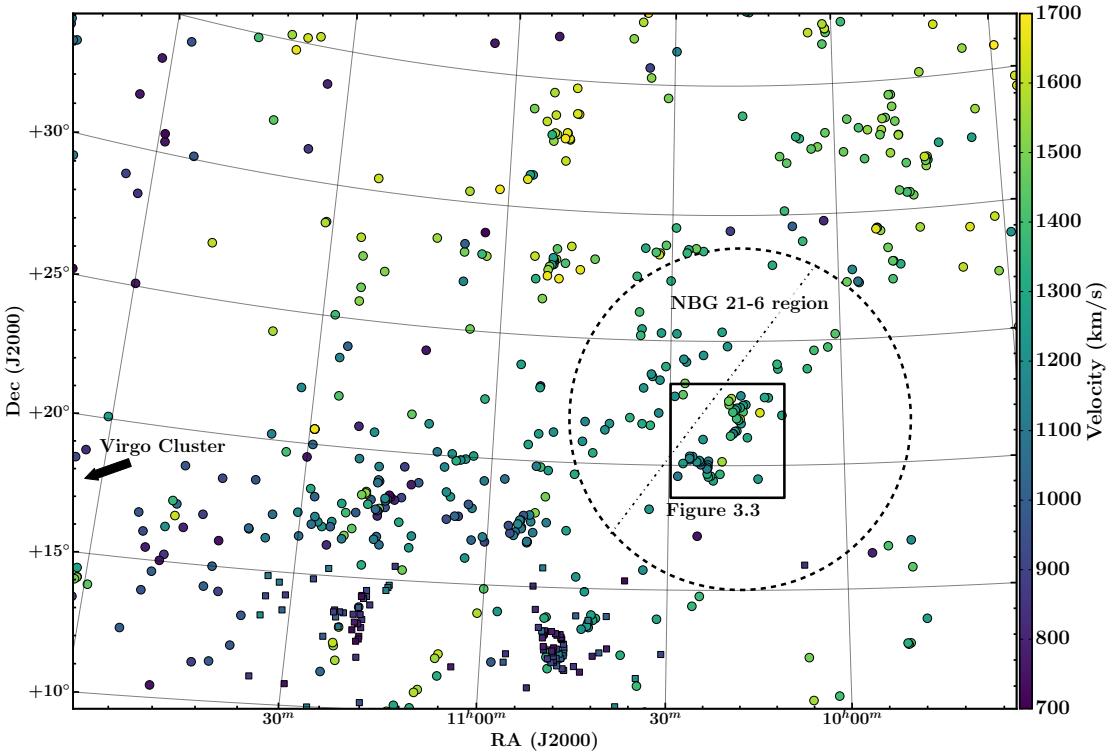

Figure 3.1: The distribution of galaxies in the NBG 21-6 region within the context of the Leo Cloud, a sparsely populated filament at D~20-30 Mpc stretching from the lower left of the image (near the Virgo Cluster) to the upper right. Sources are colour coded by heliocentric recessional velocity, and show some gradient from high to low velocities as the filament approaches the Virgo Cluster. The dashed circle has a radius of 3 Mpc at a distance of 25 Mpc, and shows the location of the NBG 21-6 region that is the primary focus of this study. Some group catalogs divide the sources in the NBG 21-6 region into two subgroups, as indicated by the dashed-dotted line. The central/SW region (below the dashed-dotted line) itself has two main concentrations, the NGC 3227 and NGC 3190 groups (Figure 3.3), which contain the large H I structures discussed in section 3.4. Members of the foreground Leo Spur (D~10 Mpc), as identified by Stierwalt et al. (2009), are indicated by squares rather than circles.

mary structure in this velocity range is the Leo Cloud,[ii] a loose collection of groups stretching ~50° across the plane of the sky at a distance of ~20-30 Mpc, from the edge of the Virgo Cluster around 12^h+15° (the lower left corner of Figure 3.1), to around 9^h30^m+35° (the upper right corner). A region of particular interest for H I studies (see section 3.2.3) is a loose association of galaxies spanning ~6 Mpc in the NW part of the Leo Cloud (indicated with a dashed circle in Figure 3.1). Figure 3.2 shows the velocity distribution of H I sources in this re-

gion, which is approximately Gaussian, with an average heliocentric recessional velocity of 1304 km s^{-1}, and a dispersion of σ ~115 km s^{-1}, in contrast with the more uniform distribution of the Leo Cloud at large.

Yet, the group relationships of galaxies in this region is unclear. Several studies assign the galaxies in this region to a single group (e.g., Huchra & Geller, 1982; Garcia, 1993), which we will refer to as NBG 21-6 following the nomenclature of the Nearby Galaxies Catalog (Tully, 1987). However, depending on the length scale chosen to link the galaxies, other authors have divided this region into two subgroups (e.g., Turner & Gott, 1976; Geller & Huchra, 1983), as indicated by the dash-dotted line in Figure 3.1, and still others further divide the SW subgroup (pictured in Figure 3.3) into the NGC 3227 group, and the NGC 3190 group (e.g., Makarov & Karachentsev, 2011).

Figure 3.2 also shows the velocity distributions of the component NGC 3190 and NGC 3227 groups, which have mean recessional velocities (dispersions) of 1220 (99) and 1353 (150) km s^{-1} respectively, in contrast with the distribution for the full NBG 21-6 region. Groups were assigned by selecting all sources within the boxed regions in Figure 3 (described in Section 3.4) within the stated velocity range. Tables 3.1 and 3.2 list the basic properties of the galaxies assigned to each group by this simplistic method (sources assigned to different groups by a more sophisticated algorithm (Makarov & Karachentsev, 2011) are noted with a star). Both the shape and narrowness of the velocity distribution suggest a

[i] Data are taken from the Arecibo General Catalog (AGC), a private database maintained over the years by MPH and RG; it contains all bright galaxies and ones of known redshift as available in NED with cz < 18000 km s^{-1} in the ALFALFA volume, additional unpublished H I results as they are acquired, and bright galaxies in other regions of the sky.

[ii] Analysis of the Leo Cloud is complicated by the superposition of the foreground Leo Spur at ~10 Mpc, which is poorly discriminated in velocity space due to infall toward the Virgo Cluster (e.g., Tully, 1987; Karachentsev et al., 2015b). ALFALFA results for the southern part of the Leo Cloud were presented in Stierwalt et al. (2009), but the coverage there only extended to $\delta < 16°$.

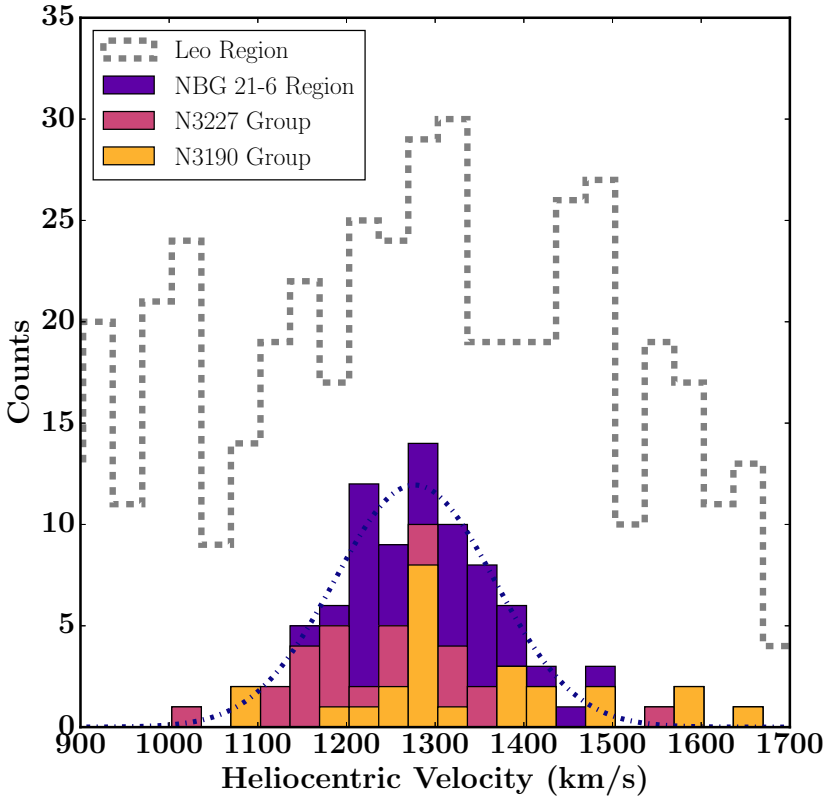

Figure 3.2: Histogram of heliocentric recessional velocities in the Leo Region. The filled purple bars indicate the counts for the NBG 21-6 region (dashed circle in Figure 3.1), which shows a roughly Gaussian distribution (the best fitting Gaussian with σ ~115 km s^{-1} is overplotted as a dash-dotted line), in contrast with the source distribution for all sources in Figure 3.1, indicated here by the dashed grey line. Sources in the NGC 3190 (yellow) and NGC 3227 (pink) groups are subsets of the NBG 21-6 distribution.

relationship between the sources in the NBG 21-6, even while the precise nature of that relationship is uncertain.

3.2.2 Distances in the NBG 21-6 Region

Distance determinations to member galaxies compound the problem of group membership. Standard Hubble flow would give distances between 15 and 22 Mpc, but the entire region is falling into Virgo at ~200 km s^{-1} (Karachent-

sev et al., 2015a), and individual galaxies are falling into the local filament and groups (see section 3.5.3). More, redshift-independent distance measurements for this group are both complicated and confusing. There are three sources with measured primary distances: NGC 3226 (23.6 Mpc) and NGC 3193 (34 Mpc) via surface brightness fluctuations (Tonry et al., 2001) and NGC 3190, which contains two type Ia supernovae that give distance estimates ranging from 18 (Amanullah et al., 2010) to 31 Mpc (Szabó et al., 2003) depending on calibration. However, given the strong interactions in this region, the primary distances to each of these objects may be strongly effected by systematic errors (see Serra et al., 2013 for a brief discussion). Other redshift-independent distances are little help, as estimates based on scaling relations are complicated by interactions; for example, estimates of distances to the merging pair NGC 3226/ NGC 3227 range from 14.5 Mpc (Yoshii et al., 2014) to 43.5 Mpc (Blakeslee et al., 2001).

Thus, observations that bridge the gap between individual galaxies and the group structure are important for disentangling the complex relationships in this region. In section 3.5 we argue that the sources in this region are gravitationally interacting, and likely to be at a similar distance. Using the corrections given in the NASA Extragalactic Database, based on the local velocity field model from Mould et al. (2000), we estimate a distance of 24.3 Mpc from the average velocity of the NBG 21-6 group. We thus choose to follow Serra et al. (2013) and assume a distance of 25 Mpc for all galaxies in the region for the remainder of this paper. We further defend this choice in section 3.5.3.

3.2.3 Interactions in the NBG 21-6 Region

Previous studies have found significant evidence of interactions between group members in the NBG 21-6 region. The NGC 3190 group centers around Hickson Compact Group 44 (HCG 44), a compact group of four galaxies of similar optical brightness. Several studies have found that the galaxies in HCG 44 appear to be H I deficient (see section 3.5.1), and NGC 3187 and NGC 3190 show strong morphological evidence of tidal interactions. Moreover, Serra et al. (2013) report the discovery of a large ~300 kpc H I tail extending to the north and west of the group.

Similarly, Mundell et al. (1995) found two tails stretching 7′ north and 16′ south (51 and 116 kpc at D=25 Mpc) of the interacting pair NGC 3226 and NGC 3227 (also called Arp 94) in deep C and D array VLA imaging. Optical imaging shows a complex set of faint stellar filaments, arcs, and loops, and Appleton et al. (2014) suggest a complex interaction history based on a plethora of multi-wavelength data.

While previous observations have been sufficient to reveal the complex nature of both the NGC 3227 and NGC 3190 groups, they have been limited by the field of view of their observations. Here we present the the first high sensitivity, complete H I maps of the entire region, corroborating and extending these results (see sections 3.4.1 and 3.4.2 for the NGC 3227 and NGC 3190 subgroups respectively), and painting a global picture of H I in the region.

3.3 Observations and Data

3.3.1 H I Data from the ALFALFA Survey

The ALFALFA observations and data processing are described in detail in previous papers (Giovanelli et al., 2005; Saintonge, 2007; Martin et al., 2009; Haynes et al., 2011). In brief, ALFALFA employs a two-pass, fixed azimuth drift scan strategy, with a bandwidth of 100 MHz and a spectral resolution of 24.4kHz (5.3 km s^{-1} at z=0) before Hanning smoothing. The data are bandpass subtracted, calibrated, and then flagged interactively for radio frequency interference (RFI). Once this "level 1" processing is complete, the data are gridded into cubes 2.4° on a side and spanning the full spectral bandwidth from -2000 to 18,000 km s^{-1} (though the cubes are split into four subcubes of 1024 spectral channels each for easy processing). Each cube was flatfielded and rebaselined, and corrected for residual telescope pointing errors. Sources are extracted using the methods of Saintonge (2007), and then each grid is examined by eye to improve on the automatic detection algorithm at lower signal-to-noise ratios (SNRs) and to identify optical counterparts in Sloan Digital Sky Survey (SDSS) and Digitized Sky Survey 2 (DSS2) images; final source parameters are measured and cataloged interactively. The public 70% ALFALFA catalog has >25,000 high SNR extragalactic detections (Jones et al., 2016).

Due to their large angular extent, the structures discussed in this paper were originally split across multiple cubes. Thus, to better study the region on physically relevant scales, the ALFALFA data were regridded into a single 50 square degree cube centered at 10^h20^m +21°. The moment 0 map of the central portion of this region is shown in Figure 3.3. This map was created by first smoothing to

2x the beam size and then masking pixels below 2.5σ. Actual telescope scheduling, gain differences between the ALFA beams, and significant flagging due to RFI resulted in uneven integration times and rms values across the cube. To correct for this we used a weights map of effective integration time after flagging to create an rms cube which allowed us to determine the appropriate threshold for masking. One strip in particular, δ ~21^d38^m, was strongly affected by low level RFI and required additional masking. The mask was then applied to the unsmoothed cube, which was then summed over velocity channels from 911 to 1722 km s^{-1}, encompassing the full velocity range of the sources in the group.

Total H I fluxes for all sources in the region were extracted manually using the standard ALFALFA software (see Haynes et al., 2011). However, the ALFALFA algorithm is optimized for point sources rather than highly extended and asymmetric sources like the features discussed below. Thus, all sources were remeasured by a modified version of the software which spatially integrates the spectrum over any arbitrary shaped area, and then divides by the summed value of the normalized beam over the same set of image pixels (e.g., Shostak & Allen, 1980). This method gives consistent measurements with the standard software on point sources, and recovers up to ~20% more flux for the extended sources in this field.

3.3.2 H I Synthesis Imaging with WSRT

Three sources in the vicinity of NGC 3226/7 were included in an exploratory sample of synthesis observations studying extreme H I sources without optical counterparts in ALFALFA (see Cannon et al., 2015 and Janowiecki et al., 2015 for

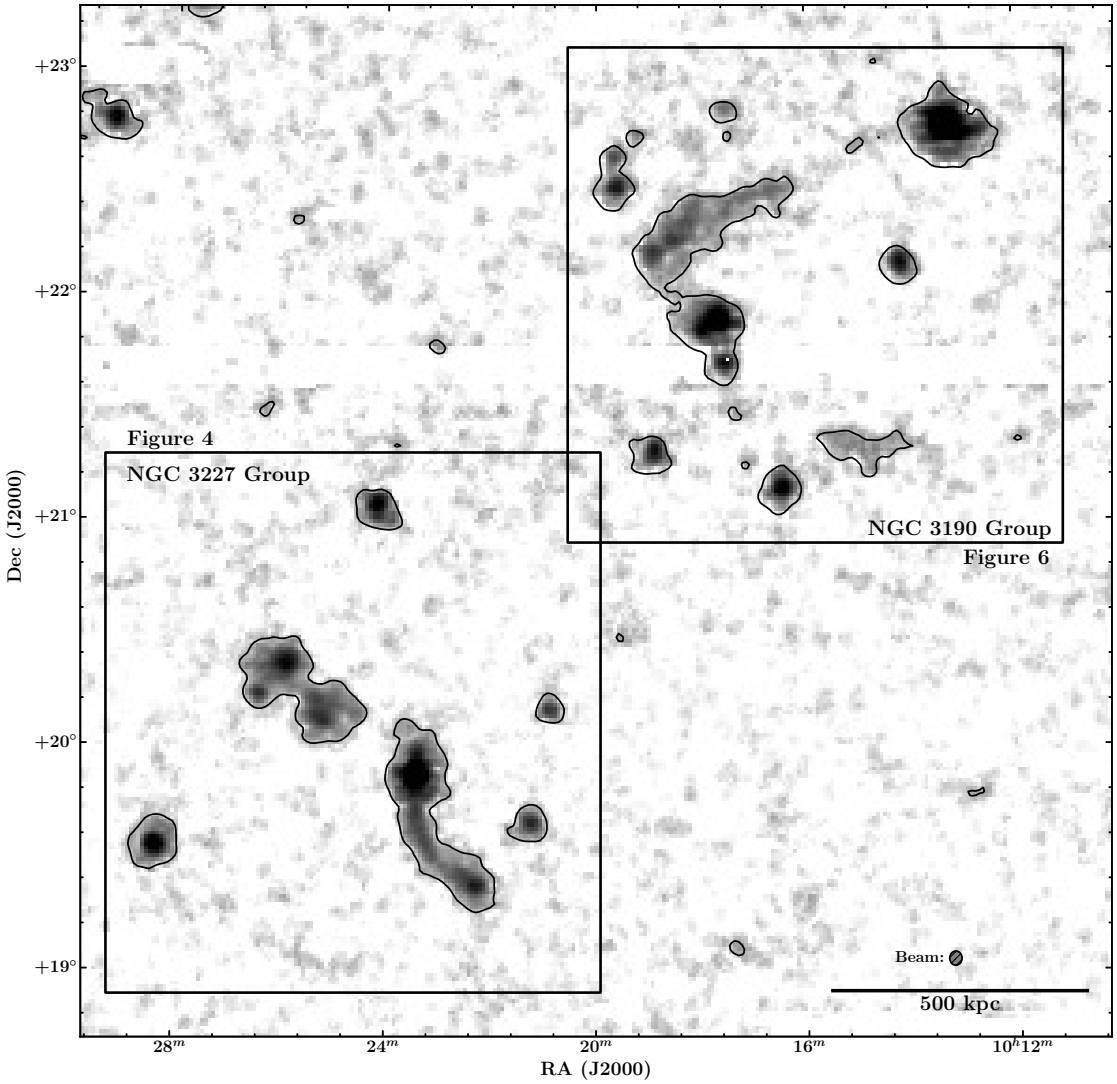

Figure 3.3: ~2x2 Mpc ALFALFA H I moment 0 map of the region containing the NGC 3190 and NGC 3227 groups, from 911 to 1722km s^{-1}, with boxes indicating the approximate locations of the two groups, and black contours denoting emission 4σ above the average rms noise of the image. This map reveals that the H I features in the groups approach the scale of the group. The extent of the features was previously undetected in WSRT and VLA synthesis observations because of their lower sensitivity, and restriction to a ~0.5 degree primary beam. A few strips with no emission (especially around δ ~21^d+38^m) have been heavily masked due to significant RFI.

more details). The connection to NGC 3226/7 was noted, but the nature of the dark H I knots, given their large separations from the merging pair, was unclear.

We observed these three sources with 4x12h pointings with WSRT, 2 centered at $10^h25^m21.0^s$ +20°10′05″, one centered at $10^h22^m26.2^s$ +19°23′17″ and one at $10^h25^m55.0^s$ +20°20′33″. The primary beams of the three pointing centers are 35′ wide. We centered observations on the H I line in one band of 10 MHz bandwidth and 1024 channels in two polarizations. This resulted in a broad range of line free channels for continuum subtraction and a velocity resolution of 4.1 km s^{-1} (FWHM) after Hanning smoothing.

We reduced the data using the same automated pipeline as applied in Wang et al. (2013), originally used by Serra et al. (2012), as described in Janowiecki et al. (2015). The pipeline uses the data reduction software Miriad (Sault et al., 1995) wrapped into a Python script. In brief, the pipeline automatically flags the data for RFI using a clipping method after filtering the data in both the frequency and time domain. After primary bandpass calibration, it iteratively deconvolves the data with the CLEAN algorithm in order to apply a self-calibration, using CLEAN masks determined on the cube with decreasing clip levels. We then subtract the continuum in the visibility domain and apply the calibration solution to the visibilities to then invert the data after Hanning smoothing. We then iteratively clean the data cubes down to the rms noise in the cubes, using CLEAN masks determined by filtering the data cubes with Gaussian kernels and applying a clip level. We used a Robust weighting of r=0.4, and binned the data to a velocity resolution of 12.3 km s^{-1}(FWHM; 6.0km s^{-1} channels) after Hanning smoothing.

For each cube we then created H I total flux maps by smoothing the images

to 2x the beam size, masking any pixel below 3σ, applying the mask to the unsmoothed cubes, and then summing along the velocity axis. We calculate H I column densities assuming optically thin H I gas that fills the WSRT beam, and also produce H I moment 1 velocity maps from cubes masked at 3σ. We measure the H I flux by applying a mask based on the smoothed moment 0 map to cubes corrected for primary beam attenuation, and then extracting and fitting 1D spatially integrated H I profiles. These fluxes are reported in Table 3.1.

3.4 Results

Figure 3.3 shows the ALFALFA moment 0 map of the central ~20 deg^2 of the regridded cube. At 25 Mpc, this image covers ~2x2 Mpc on the sky. The NGC 3227 and NGC 3190 groups are visible to the southeast and northwest of the center of the image, and are shown in greater detail in Figures 3.4 and 3.6 respectively. The H I plumes associated with NGC 3227 and the large feature in the NGC 3190 group extend to similar scales as the groups themselves. Indeed, Makarov & Karachentsev (2011) estimate the harmonic radii of the NGC 3227 and NGC 3190 groups to be 125 kpc and 276 kpc respectively (at D=25 Mpc), significantly less than the projected length of the structures discussed below. The large extent of these H I features is the main result of this paper. Here we describe the properties and extent of the features in the NGC 3227 and NGC 3190 groups in sections 3.4.1 and 3.4.2, and then discuss the mass of cold intragroup gas in section 3.4.3.

[i]NGC 3190 is referred to as NGC 3189 in some papers. According to Serra et al. (2013), NGC3189 is the southeast component of NGC 3190.

Table 3.1: Galaxies in the NGC 3227 Group: Full caption on the following page.

AGC	Name	Coordinates J2000	cz km s^{-1}	W_{50} km s^{-1}	$F_{\mathrm{H\,I,ALFA}}$ Jy-km s^{-1}	$F_{\mathrm{H\,I,SYN}}$ Jy-km s^{-1}	Source	log $M_{\mathrm{H\,I}}$ $M_\odot$	$f_{\mathrm{H\,I}}$ %
(1)	(2)	(3)	(4)	(5)	(6)	(7)	(8)	(9)	(10)
5590*	NGC 3213	10:21:17.4+19:39:04	1347±1	134±2	1.62±0.06			8.38	3.2
5620	NGC 3227	10:23:30.5+19:51:53	1126±2	412±3	17.52±0.10	14.5	M95	9.41	35.0
5629*		10:24:12.9+21:03:01	1238±1	113±2	3.58±0.06			8.72	7.2
5653	I610	10:26:28.3+20:13:42	1168±2	296±4	1.64±0.06			8.38	3.3
5675	M+327047	10:28:30.0+19:33:46	1106±1	83±2	4.55±0.06			8.83	9.1
202045†	D568-04	10:20:56.1+20:09:21	1557±2	73±4	1.31±0.04			8.29	2.6
$\mathrm{HI_{NE}}$		10:25:37.4+20:20:34	1210±2	57±4	10.18±0.21	9.61±0.39	L16	9.18	20.3
$\mathrm{HI_{North}}$		10:23:25.7+20:00:01	1305±33	134±16	2.88±0.16	3.3	M95	8.63	5.8
$\mathrm{HI_{South}}$		10:22:50.5+19:27:48	1292±5	49±5	6.77±0.21	5.12±0.2	L16	9.00	13.5
NGC 3227 group total:								9.87	1.0
5617	NGC 3226	10:23:27.0+19:53:54	1275	...	...			...	...
718673		10:23:15.4+20:10:40	1151	...	...			...	...
718681		10:23:21.6+20:01:38	1166	...	...			...	...
718719		10:24:34.7+20:01:57	1028	...	...			...	...
718778		10:26:31.0+20:16:60	1163	...	...			...	...
739353		10:23:22.4+19:54:51	1338	...	...			...	...
739467		10:27:37.5+20:04:43	1268	...	...			...	...

Table 3.1: Galaxies in the NGC 3227 Group. Column 1: ID Number from the Arecibo General Catalog; column 2: alternate name; column 3: RA and Dec correspond to the optical center of each galaxy, except for H I only features, where the coordinates give the position of the peak flux; column 4: heliocentric optical recessional velocity. For all sources detected in H I, the value is from the ALFALFA catalog, else the value is from the Arecibo General Catalog; column 5: H I line width from ALFALFA, measured at the 50% flux level; note that AGC 5620 and HI_{North} are blended, so the fluxes contain addition systematic uncertainty; column 6: $\int S dV$ as measured in the ALFALFA data; column 7: $\int S dV$ as measured in synthesis data, corrected for primary beam attenuation; column 8: Source of the synthesis measurement. Sources labeled L16 are from WSRT measurements presented in this paper, and those labeled M95 are VLA measurements from Mundell et al. (1995); column 9: H I Masses assume a distance of 25 Mpc for all sources; column 10: Fraction of group H I, $F_{\mathrm{H\,I,galaxy}}/F_{\mathrm{H\,I,group}}$, in percent. *Classified as a member of the NGC 3190 group by Makarov & Karachentsev (2011) †Classified as a background source by Makarov & Karachentsev (2011) Note: Sources below the horizontal line are not detected at the ALFALFA sensitivity limit, which is a function of W_{50} and the rms at the position of the source (see eq. 2 in Haynes et al. (2011)). For a 50 km s^{-1} wide source, the average 4σ ALFALFA flux upper limit is 0.3 Jy-km/s, which translates into a fractional limit of <0.6% of the total group mass for each undetected source.

3.4.1 Extended Tails in the NGC 3227 Group

Figure 3.4 shows the ALFALFA data for the NGC 3227 Group, overlaid on an SDSS r-band image created with Montage. The bottom and side panels show RA-velocity and Dec-velocity views of the group, with black vertical and horizontal bars indicate the ALFALFA velocity width at the 50% flux level for detected galaxies. A dashed thick black circle indicates the region imaged by Mundell et al. (1995), who report the detection of two H I plumes (labeled HI_{North} and HI_{South} in Figure 3.4) extending 51 and 116 kpc to the north and south of NGC 3227 in the center of the NGC 3227 group. However, the primary beam of the VLA at 1420 MHz (the effective field of view of the interferometer) is only ~35′. Thus, while, the ALFALFA data confirm the plumes detected in the high resolution VLA maps, they find that the plumes extend far beyond the VLA primary beam to ~10 and ~40 arcminutes (73 and 291 kpc at 25 Mpc). They also

Table 3.2: Galaxies in the NGC 3190 Group: Full caption on the following page.

AGC	Name	Coordinates J2000	cz km s^{-1}	W_{50} km s^{-1}	$F_{\mathrm{H\,I,ALFA}}$ Jy-km s^{-1}	$F_{\mathrm{H\,I,SYN}}$ Jy-km s^{-1}	Source	log $M_{\mathrm{H\,I}}$ $M_\odot$	$f_{\mathrm{H\,I}}$ %
(1)	(2)	(3)	(4)	(5)	(6)	(7)	(8)	(9)	(10)
5510	NGC 3162	10:13:31.6+22:44:13	1302±1	177±2	30.48±0.08			9.65	40.0
5524	123-027	10:14:21.8+22:07:28	1636±1	180±2	2.73±0.07			8.60	3.6
5544	NGC 3177	10:16:34.0+21:07:23	1310±2	181±4	3.76±0.07	2.11	S13	8.74	4.9
5554	NGC 3185	10:17:38.6+21:41:16	1230±1	253±2	3.58±0.08			8.72	4.7
5556	NGC 3187	10:17:47.9+21:52:23	1586±2	219±4	11.19±0.09	8.22	S13	9.22	14.7
5559	N3189/90[i]	10:18:05.5+21:49:51	1310±4	463±7	4.53±0.12	4.0	S13	8.82	5.9
5574	M+425001	10:19:43.0+22:27:06	1462±5	130±10	2.30±0.08			8.53	3.0
5575		10:19:46.9+22:35:39	1471±3	123±5	1.28±0.07	0.84	S13	8.28	1.7
200162	123-024	10:12:52.5+22:43:21	1285±11	128±23	1.48±0.07			8.34	1.9
200255*	124-001	10:19:01.5+21:17:01	1083±3	50±6	2.65±0.06			8.59	3.5
201052†		10:17:23.3+21:47:58	1943±1	42±3	2.38±0.06	1.03	S13	8.55	3.1
201174	F500-4	10:19:19.2+22:42:05	1573±3	51±6	0.57±0.06			7.92	0.7
201337	123-035	10:17:39.5+22:48:35	1178±3	183±7	1.20±0.08			8.25	1.6
202134	Wa5	10:10:32.8+22:00:40	1280±12	79±25	0.37±0.06			7.74	0.5
$\mathrm{HI_{Main}}$	$\mathrm{T_N}$	10:18:05.4+22:31:27	1302±5	115±3	7.66±0.43	2.79	S13	9.05	10.1
NGC 3190 group total:								10.05	1.0
5562	NGC 3193	10:18:24.9+21:53:36	1378	...	...			...	...
208748	124-001b	10:19:00.8+21:16:55	1085	...	...			...	...
208761		10:19:28.6+21:11:24	1381	...	...			...	...
718513		10:17:17.6+22:09:39	1423	...	...			...	...
718530		10:18:22.8+21:23:31	1408	...	...			...	...
718531		10:18:40.9+21:22:49	1289	...	...			...	...

Table 3.2: Galaxies in the NGC 3190 Group. Column Definitions are the same as Table 3.1. Note that, as in Table 1, distance dependent parameters are calculated using a distance of 25 Mpc for all sources. Measurements labeled S13 are WSRT measurements from Serra et al. (2013). Note that AGC 5556 and 5559 are blended in the ALFALFA data. For a 50 km s^{-1}wide source, the average 4σ ALFALFA flux upper limit of 0.3 Jy-km/s, translates into a fractional limit of <0.4% of the total group mass for each undetected source. *Classified as a member of the NGC 3227 group by Makarov & Karachentsev (2011) †Classified as a background source by Makarov & Karachentsev (2011).

reveal the presence of a previously unreported feature stretching 0.9 degrees to the NE (labeled HI_{NE} in Figure 3.4), distinct from the other plumes.

All three H I appendages appear to have no detectable stellar counterparts at the surface brightness limit of SDSS (~25 mags $asec^{-2}$); optically detected galaxies of known redshift (i.e. of m_g <17.7) are indicated with open diamonds, color coded by their velocity to match the scale in Figure 3.1. While there are several reasonably bright optical sources in this region, none of them are clearly associated with the H I features.

The Southern H I Plume (HI_{South})

The H I plume extending to the south of NGC 3227 shows excellent agreement with the Mundell et al. (1995) maps within the region imaged by the VLA. Both data sets show that the plume (which we will refer to as HI_{South}) rises steeply in velocity from ~1200 km s^{-1} to ~1300 km s^{-1} moving south away from NGC 3227. However, the feature extends ~28′ beyond the region covered by the VLA, continuing to rise in velocity, and decrease in projected column density. ~17′ from NGC3226/7, it bends west and begins to decrease in velocity from ~1320 to ~1270 km s^{-1}. As shown in the PV panels in Figure 3.4, the end of the plume shows a marked increase in projected column density, and the velocity disper-

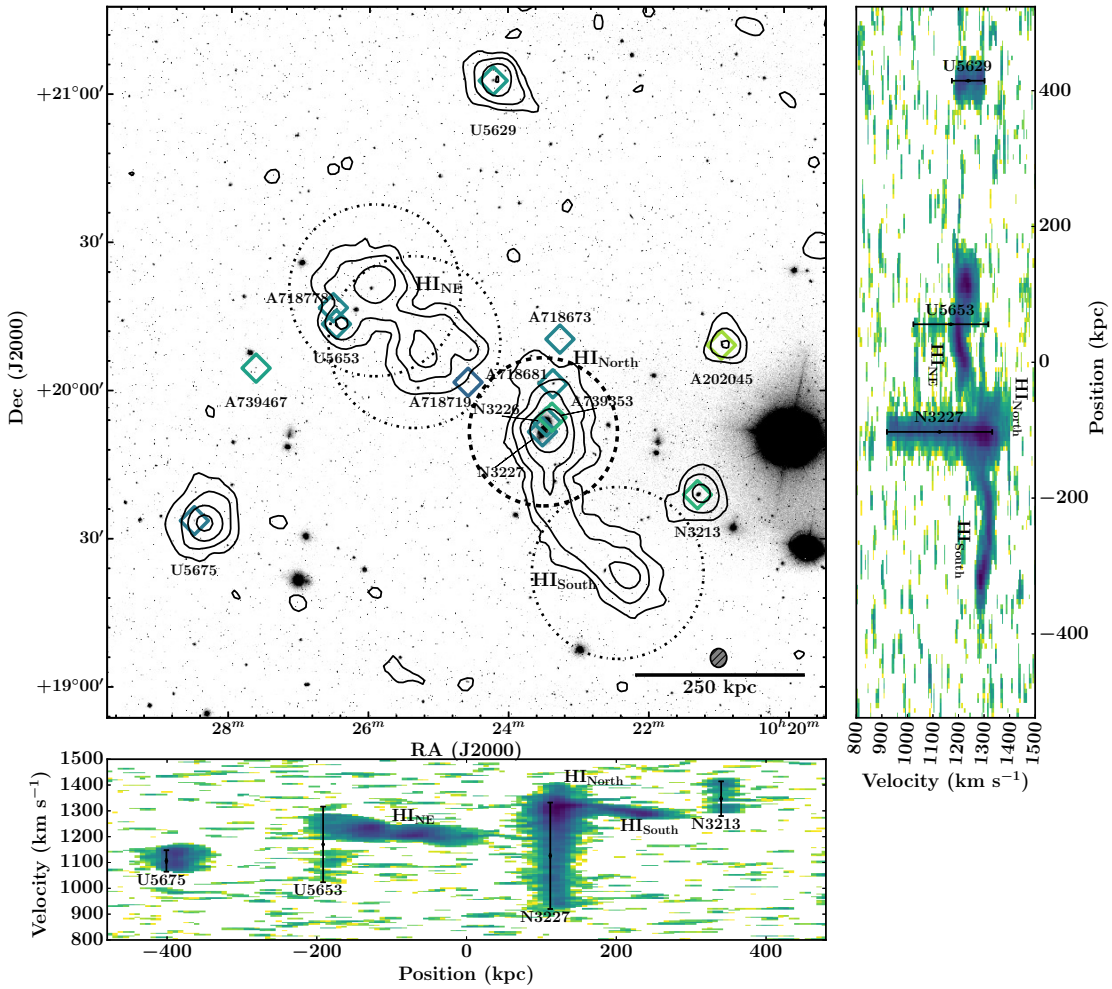

Figure 3.4: ALFALFA moment 0 contours (summed over 900 to 1500 km s^{-1}) overlaid on a SDSS r-band optical image of the NGC 3227 group, demonstrating the large extent of the H I features relative to the optical emission from the merging pair NGC 3226/7 (near the center of the image). Contour levels are spaced logarithmically at 1.2, 2.4, 4.8, 9.6, and 19.2×10^{18} atoms cm^{-2} (assuming the H I uniformly fills the ALFA beam of 3.3′x3.8′). The lowest contour level is 4σ above the rms noise. The thick dashed circle indicates the region mapped in higher resolution VLA imaging by Mundell et al. (1995), showing the need for wide field mapping for a full understanding of this system. The thinner dash dotted circles show the field of view of the WSRT observations shown in Figure 3.5. Optical galaxies with known redshifts between 700 and 1700 km s^{-1} are marked with open diamonds, colored by their recessional velocity to match the color scale from Figure 3.1. Catalog designations AGC, UGC, and NGC are abbreviated by their first initial. The ALFA beam is represented by a hashed circle in the lower right. Right and Bottom: ALFALFA position-velocity diagram summing the H I emission across the image from 10:27:30 to 10:21:45 in RA and from 19:00:00 to 20:40:00 in Dec respectively (the ranges are selected to minimize confusion and highlight the H I plumes in the diagrams). Black vertical and horizontal bars indicate the ALFALFA velocity width at the 50% flux level for detected galaxies in the region. The diagrams show the coherence of the plumes in velocity space, and the separation in velocity of HI$_{\rm NE}$ at ~1200 km s^{-1} and HI$_{\rm North}$ at ~1400 km s^{-1}.

sion of the tail appears to decrease significantly moving south from NGC 3227. However, the significantly higher resolution WSRT observations of the end of the plume, shown in panels c and d of Figure 3.5, show a messy, extended distribution, inconsistent with any suggestion of a "dark" or tidal dwarf galaxy (TDG). Indeed, the higher column density emission traces the ALFALFA data well, and has clear elongated, tail like morphology. The column density peaks at $2.3{\times}10^{20}$ atoms cm^{-2} (for a beam of $14''{\times}\,47''$), but there is no associated stellar emission at the detection limits of SDSS. There is a low surface brightness galaxy at $10^h22^m53.2^s$ +19°34′36″ without a measured redshift, but there is no associated H I in the higher resolution WSRT images. The bright elliptical galaxy at $10^h22^m37.7^s$ +19°23′49″ has a measured redshift of 11,792 km s^{-1}.

We note that NGC 3213 is ~22′ (~160 kpc) from the end of HI_{South}, has a similar recessional velocity (see the RA-velocity plot in Figure 3.4), and appears to show some extended H I emission at low SNR; however, our data do not have the sensitivity to determine if it is related to this southern plume. Thus, the H I distribution mapped here is consistent with the properties of a tidal tail associated with the merging pair NGC 3226/7, but we cannot completely rule out the rather unlikely possibility that HI_{South} is instead an H I bridge.

The Northern H I Plume (HI_{North})

The northern plume reported in Mundell et al. (1995) also is consistent with the ALFALFA data, but is blended with the emission from the TDG identified in Mundell et al. (2004) and NGC 3227, in Figure 3.4. While it appears to spatially connect with the northeastern feature (HI_{NE}, discussed below), the two tails are well separated in velocity space, as demonstrated in the PV diagrams in Figure

3.4. The northern structure increases in velocity from 1300 to 1400 km s^{-1}, as one moves away from NGC 3226/7 to a projected linear separation of 15′ (compared with HI_{NE} (section 3.4.1), which approaches NGC 3226/7 at a recessional velocity of 1240 km s^{-1}).

Appleton et al. (2014) use Spitzer IRAC observations together with the VLA H I data to connect this northern structure to the elliptical galaxy NGC 3226, suggesting that the gas is infalling onto NGC 3226. We note that it shows a significantly wider velocity dispersion (~50 km s^{-1}), and steeper velocity gradient than HI_{South}, and that there are suggestions of significant substructure at lower SNR. There are two blue, fuzzy galaxies of moderate magnitude (AGC 718681 with M_r = -17.3 and AGC 718673 with M_r = -16.1 at 25 Mpc) that fall within this plume's H I contours, but both objects have recessional velocities that fall below that of the detected H I (1151 km s^{-1} and 1166 km s^{-1} respectively). The compact dwarf AGC 739353 near NGC 3226 has a recessional velocity of 1338 km s^{-1}, somewhat higher than HI_{North}. Further modeling will be necessary to confirm the origins of this feature (and if, in fact it is a tidal tail, a tidal bridge, or something else).

The Northeastern Feature (HI_{NE})

Figure 3.4 also shows a bright H I feature extending 0.9 degrees to the northeast of NGC 3226/7. The feature is somewhat more massive than HI_{South}, but has a clumpier gas distribution, higher velocity dispersion, and more complicated velocity field. The nature of the feature's connection to NGC 3226/7 was not immediately clear, since it is not connected at the column density sensitivity of our data. However, emission detected at 2.5σ in at least 3 neighboring beams

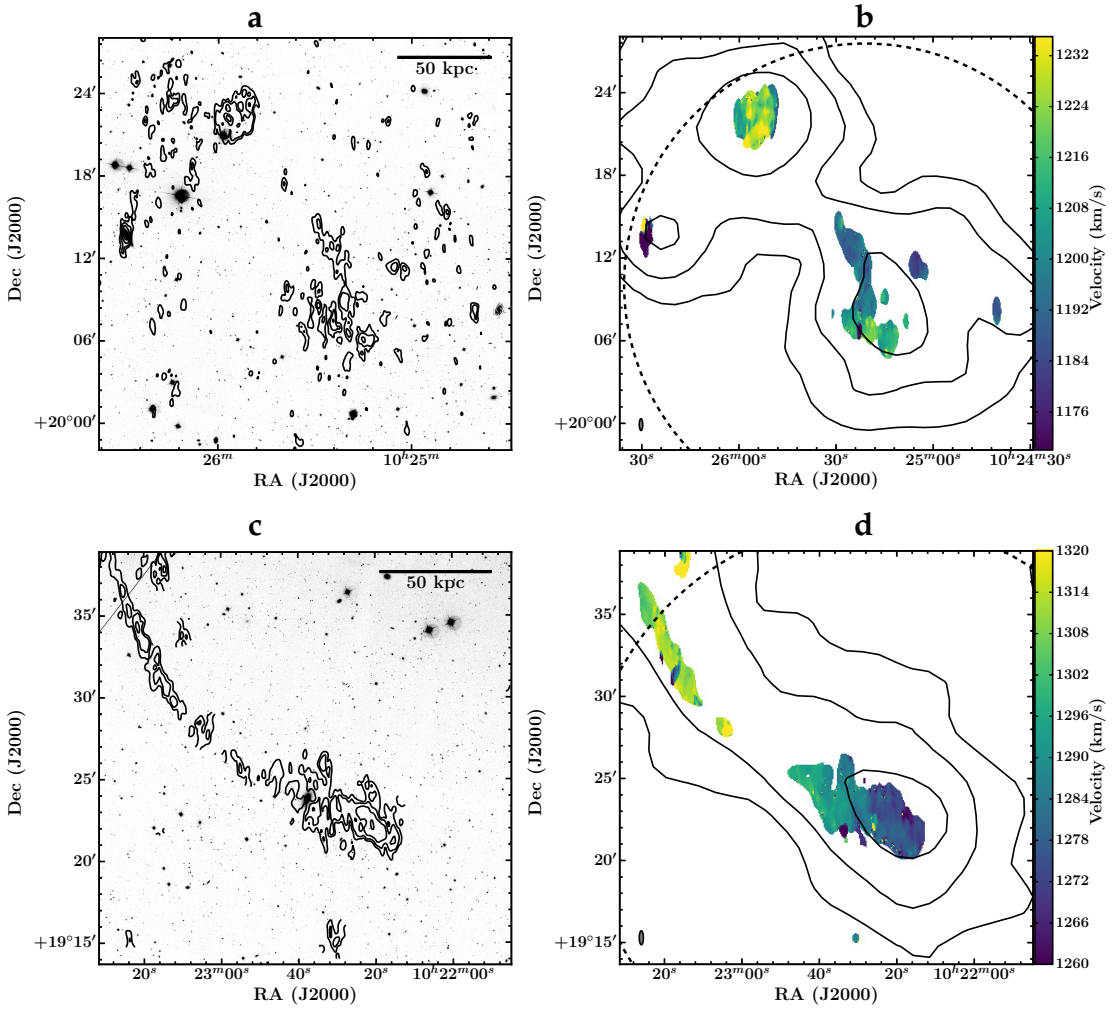

Figure 3.5: Left: High resolution WSRT synthesis imaging of the ends of the North-eastern (HI_{NE}) and Southern (HI_{South}) H I features associated with NGC 3227, showing messy, apparently tidal morphology in the higher column density gas. Panels a and c show WSRT H I column density contours at 3.5, 7, 14, 28, and 56 $\times 10^{19}$ atoms cm^{-2} (assuming the H I uniformly fills the beam of 14″$\times$ 47″) of HI_{NE} and HI_{South} respectively, overlaid on g-band images from SDSS created with Montage. Panels b and d show WSRT moment 1 maps of HI_{NE} and HI_{South} respectively, with ALFALFA flux density contours from Figure 3.4 overlaid in black. The WSRT observations match well with the lower resolution ALFALFA observations, and both features show coherent velocity structure. The FWHM of the WSRT primary beam is indicated by black dashed circles; significant primary beam corrections are necessary to estimate the flux of the entire features. The WSRT beam is indicated by a small grey circle in the lower left corner of panels b and d.

leads away from NGC 3226/7 at around 1230 km s^{-1} (most easily seen in the PV diagrams), forming a smooth arc with the rest of the NE tail. This feature shows two primary projected density peaks in the ALFALFA data, one roughly associated with the velocity minimum, and the other near the end of the tail. The WSRT observations, shown in Figure 3.5, resolve these peaks into several clumps, revealing complicated structure in the high column density emission. The SW clump appears messy with two or more density peaks, and the velocity field suggests it may contain significant substructure. Some of the emission extends in the NE-SW direction, while the emission at higher velocity is elongated in the EW direction. The NE structure appears as a single clump with a peak column density of 3.9×10^{20} cm^{-2} in the WSRT data (assuming the flux fills the 13″×41″ beam integrated over the width of the source), but does not appear to show coherent velocity structure.

The disordered morphology at high column density, and the smooth, correlated nature of the structures in the ALFALFA data point to a tidal connection between NGC3226/7 and this NE structure. However, detailed modeling will be required to understand the full history of this feature, which may be the product of several interactions within the group.

The entire structure shows no stellar emission in SDSS imaging. There are 3 optical galaxies with measured redshifts in the nearby vicinity. AGC 718719 is fairly small and blue, and appears in projection near NGC 3226/7. However, with a recessional velocity of 1028 km s^{-1} it appears to be unrelated to the details of the tail. AGC 718778 (v_{helio}=1163 km s^{-1}) is a low surface brightness dwarf located near the northeastern end of the tail, and at a more similar velocity to the tail, but is still at a lower recessional velocity than the detected gas. UGC 5653 is

an edge on spiral with a clear dust lane located in the vicinity, but to the south of HI_{NE}. While some of the emission from UGC 5653 is blended with HI_{NE}, its central recessional velocity is lower than bulk of the nearby emission from HI_{NE} (1170 km s^{-1} when separated from the other emission). It is possible that HI_{NE} is, in fact, a bridge between UGC 5653 and NGC 3227, however the WSRT observations do not indicate a clear connection between the H I in UGC 5653 and HI_{NE}, and the geometry seems rather unfavorable. Further, without measured primary distances, velocity crowding from infall requires that these sources be interpreted with caution since there is a small chance that they are simply projected to a similar region of phase space. However, we do note that the 6 objects detected without any H I in this subgroup (besides NGC 3226; listed in the bottom of Table 3.1) are all in close proximity to HI_{NE} or HI_{North} discussed above, and have somewhat similar optical colors and morphologies. All other objects brighter than m_g=17.7 have detected H I in ALFALFA.

The moment 0 map also reveals suggestive tidal features at low SNR extending to the southwest of the NE plume toward the low surface brightness dwarf galaxy UGC 5675. However, deeper observations would be necessary to put this low SNR suggestion on firmer footing. Understanding the origins of the three main features detected here will require detailed dynamical modeling.

3.4.2 Extended Tails in the NGC 3190 Group

Located approximately 1 Mpc to the NW of the NGC 3227 group, the NGC 3190 group is the other primary overdensity in the NBG 21-6 region. Like the NGC 3227 group, the NGC 3190 group is know to exhibit extended H I with-

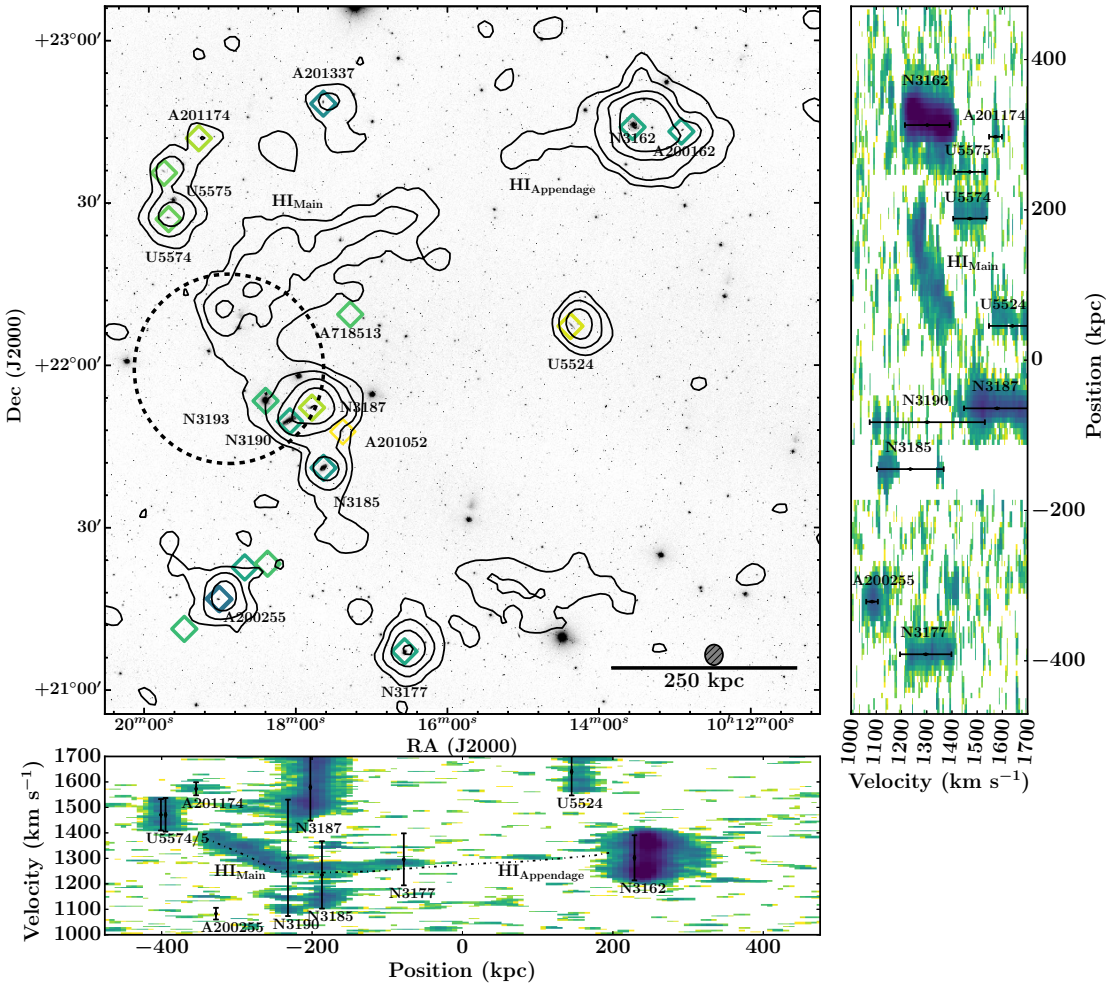

Figure 3.6: ALFALFA imaging of the central region of the NGC 3190 subgroup overlaid on an SDSS r-band optical image, showing the extended dark feature to the north of HCG 44, and the likely connection to NGC 3162. Optical galaxies with measured redshifts are indicated by open diamonds as in Figure 3.4. The ALFALFA moment 0 contour levels are spaced logarithmically at 2, 6, 18, and 54×10^{18} atoms cm^{-2} (assuming the H I uniformly fills the ALFA beam of 3.3′×3.8′). The lowest contour level is 4σ above the rms noise. The black dashed circle indicates the FWHM of the WSRT primary beam from Serra et al. (2013). Note that the entire northern tail appears optically dark at the detection limits of SDSS. Right and Bottom: ALFALFA PV diagrams summing the H I emission across the image from 10^h12^m to 10^h20^m in RA and from 21°30′ to 23° in Dec respectively (the ranges are selected to minimize confusion in the diagrams). Note that NGC 3185 is missing significant emission between v~1200-1300 km s^{-1} due to RFI masking, so the entirety of the main H I tail is visible in the bottom PV diagram. The emission from HI_{Main} and $HI_{Appendage}$ are underscored by a dashed dotted line, showing that they align well in both position and velocity.

out apparent associated stellar emission. Specifically, using a deep 6x12h pointing with WSRT, Serra et al. (2013) reported the detection of a large H I feature (which they refer to as the northern tail, T_N) near the center of the group, extending ~20′ (220 kpc) to the northwest of HCG 44, and optically dark down to μ_g = 28.5 mags asec^{-2} (in deep CFHT imaging). They further note the detection of HIPASS emission beyond the edge of the WSRT primary beam, which might extend the tail to ~300 kpc, and the detection of a small cloud (C_S) to the east of HCG 44 and the south of the main H I feature. They suggest that the large H I feature originated due to tidal stripping, and suggest that it may have originated from an interaction between NGC 3190 and NGC 3187, or from an interaction between NGC 3162 and the members of the compact group during a close flyby.

Like in the NGC 3227 group, ALFALFA finds that this previously detected H I feature extends to the group scale, well beyond the region previously studied, and finds evidence of additional extended H I structures. Figure 3.6 shows ALFALFA H I column density contours overlaid on a Montage SDSS g-band mosaic of the NGC 3190 group. The primary beam from Serra et al. (2013) is shown as a black dashed circle. The ALFALFA observations, which have an effective integration time of 40 seconds per beam, are sensitive to low column density structure across the entire group, and show that full extent of the primary H I structure. This feature, which we will refer to as HI_{Main} hereafter, contains all of T_N and the suggestive HIPASS emission, and more, covering ~45′ (330 kpc) across the sky. The feature shows significant substructure, which is confirmed in a recent, deep pointing with KAT-7, and discussed in detail in Hess et al. (2017).

The ALFALFA data further show a low column density extension stretching

SE from NGC 3162 in the direction of HI_{Main}. This appendage ($HI_{Appendage}$) is relatively low signal-to-noise, but is detected at >2.5σ in 6 contiguous beams, and has a narrow (W_{50}=31 km s^{-1}), but coherent structure in velocity space. Moreover, it is not simply a sidelobe of NGC 3162, since it extends ~30′ from the center of NGC 3162 (the peak of the first ALFA sidelobe is at ~5′). The emission from the NGC 3162 extension does not connect directly to HI_{Main} at the sensitivity of the ALFALFA data, however, Figure 3.6 demonstrates that they are well aligned both spatially and in velocity space, strongly suggesting that HI_{Main} is, in fact connected to NGC 3162. The apparent connection of the H I features means that the entire structure is nearly 1.4 degrees (610 kpc) long.

Several other weaker pieces of evidence fit with the interpretation that HI_{Main} is associated with NGC 3162. The mass budget, presented below in section 3.4.3, argues for the reality of the connection to NGC 3162, since the tail contains 20% of the H I mass of NGC 3162, but at least 40% of the H I mass of any of the sources in HCG 44. Additionally, NGC 3162 shows some sign of the presence of a forward tail encompassing the smaller spiral AGC 200162, and the gas in the full H I structure appears to spread out spatially as it moves away from NGC 3162, possibly consistent with gas spreading as a function of time after leaving NGC 3162. However, we note that the velocity dispersion smoothly increases from ~20 km s^{-1} to ~60 km s^{-1} moving away from NGC 3162, which seems to suggest energy input from HCG 44.

Indeed, since HI_{Main} lies within the disk velocities of both NGC 3162 and NGC 3190, it is reasonable to assume that the feature is related to both sources. However, The connection between the giant H I feature and the galaxies of HCG 44 is less clear. The moment 0 contours in Figure 3.6 show a low column

density bridge between the brightest parts of the tail and HCG 44. However, when examined in velocity space, the ALFALFA data hint that the extended H I may be composed of at least two superimposed kinematic features. Figure 3.7 presents the region surrounding HI_{Main}, masked to contain just the emission clearly associated with the extended H I structures. The blue-green contours show the H I emission associated with HI_{Main} and $HI_{Appendage}$ demonstrating that together they extend nearly continuously from NGC 3162 toward a point ~20′ north of HCG 44, bending through velocity space from ~1300 km s^{-1} near NGC 3162 down to ~1250 km s^{-1}, and then receding to ~1400 km s^{-1}. Near the SE end of HI_{Main} the H I appears to reach south from the main feature toward NGC 3190, potentially suggesting a connection between HI_{Main} and the compact group. However, combination of the ALFALFA data with the WSRT data from Serra et al. (2013) and with recently obtained KAT-7 data (Hess et al., 2017) shows no strong evidence that HI_{Main} is connected to HCG 44 in the deeper cube.

The red contours in Figure 3.7 show H I emission summed over velocities above 1400 km s^{-1}. These reveal a potential second, low column density, low signal-to-noise structure, hereafter $HI_{Secondary}$, visible at higher velocities (~1500 km s^{-1}). The structure extends east from NGC 3187 to encompass the cloud dubbed C_S in Serra et al. (2013), and then north toward UGC 5574, UGC 5575, and AGC 201174, at matching recessional velocities. This suggestion, however, is tentative, since the structure is detected at low significance (the significance of this structure in Figure 3.7 is potentially exaggerated by the superposition of signal from multiple low significance features). The combined ALFALFA, WSRT, and KAT-7 data (Hess et al., 2017) also shows a compact H I cloud at the location of the northern peak in the red contours in Figure 3.7, but do not show clear emission connecting it to C_S or NGC 3187. Thus, much of the

extent of this structure is likely a result of beam smearing and artifacts in the ALFALFA data.

Figure 3.6 also shows the apparent detection of an extended feature around 10^h15^m +21°20′. Analysis of the ALFALFA spectrum at this position shows significant baseline fluctuations, consistent with low level RFI not masked by our other algorithms. Similarly, Figure 3.6 also shows the suggestion of a southern extension off NGC 3185, however, this extension is in the region of the cube with low weights due to significant RFI. Thus, further observations of these regions will be necessary to know if there is any real H I emission to the south and southeast of HCG 44.

3.4.3 The H I Mass Budget in the NGC 3190 and NGC 3227 Intragroup Medium

The extended features in both the NGC 3190 and NGC 3227 groups contain a significant fraction of the total H I in the group. Tables 3.1 and 3.2 list the fluxes and H I masses for all sources detected by ALFALFA in the NGC 3227 and NGC 3190 groups respectively, assuming a common distance of 25 Mpc (note that under this assumption, the NGC 3190 group contains 1.5× the H I mass of NGC 3227 group). Column 10 gives the full breakdown of H I in each group, listing the percentage of H I in each feature relative to the sum of each subgroup. The dark plumes in the NGC 3227 group (HI_{North}, HI_{South}, and HI_{NE}) have a combined log H I mass of 9.47, 40% of the total H I in the group, and 53% of the gas associated with NGC 3226/7. Only slightly less massive, HI_{Main} in the NGC 3190 group has a log H I mass of 9.05, making up 10% of the total group

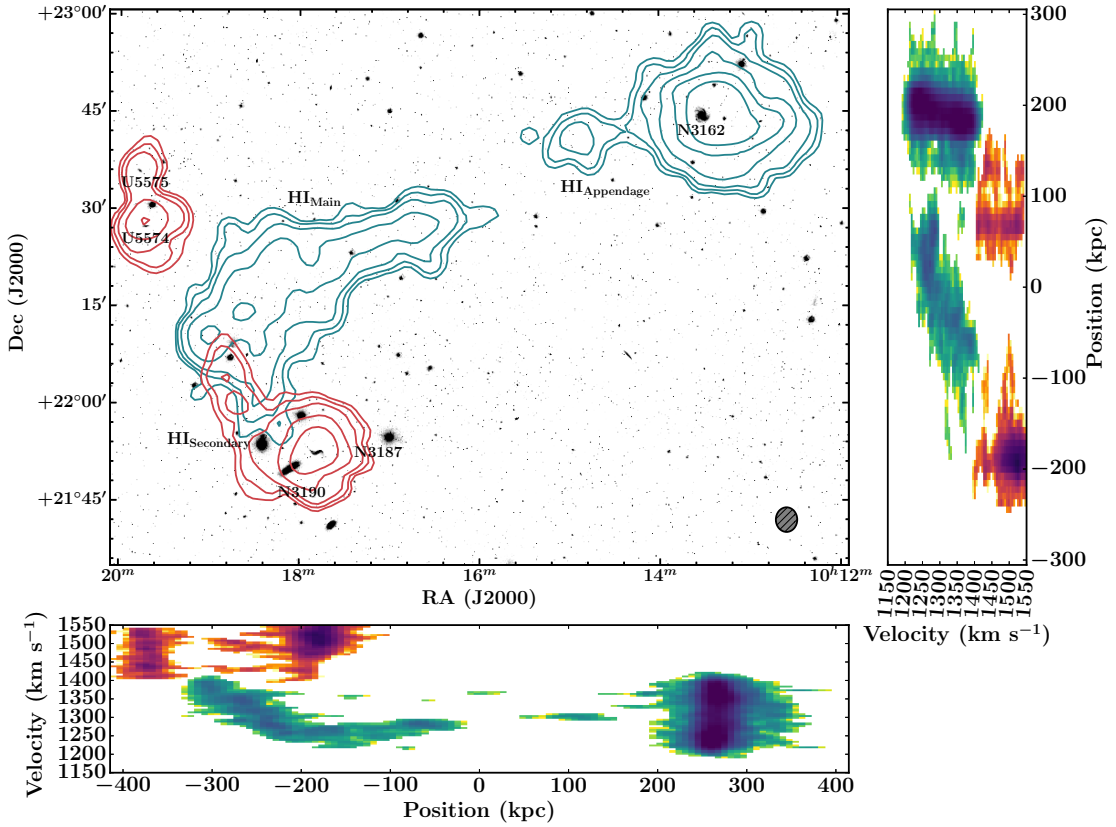

Figure 3.7: ALFALFA moment 0 H I contours, masked to highlight the primary H I features in the NGC 3190 group, overlaid on SDSS g-band optical images, with PV diagrams as in Figure 3.6. The blue-green contours and blue to green colored emission in the PV diagrams outline the entire main feature (HI_{Main}), which is visible at velocities below 1400 km s^{-1}, and appears to be associated with NGC 3162. The red contours and red to magenta colored emission at velocities above 1400 km s^{-1} show the suggestion of a secondary feature ($HI_{Secondary}$) at higher velocity, which may suggesting a connection between NGC 3187 and UGC 5574, but this feature is only partially confirmed in deeper data (Hess et al., 2017). Contour levels are spaced logarithmically at 6, 12, 24, 48 96, and 192×10^{17} atoms cm^{-2} (assuming the H I uniformly fills the ALFA beam).

H I mass. However, 40% of the H I mass of the NGC 3190 group is contained in NGC 3162; HI_{Main} is nearly 30% of the combined H I mass of the galaxies in HCG 44. For comparison, the Leo Ring makes up 24% of the $M_{H\,I}$ in the M96 group, and tidal plumes in the Leo Triplet constitute 14% of the H I mass in the M66 group (Stierwalt et al., 2009).

Comparisons to synthesis imaging can give a sense of the amount of low sur-

face density gas in these intragroup features, but direct comparison is difficult due to significant differences in the data and the subsequent analysis. Tables 3.1 and 3.2 give synthesis measurements where available. WSRT observations recover 94% of the flux in HI_{NE}, and 74% of the flux in HI_{South} in the NGC 3227 group. However, the large extent of the dark H I features necessitates large primary beam corrections for the portions of the sources near the edge of the beam, which means these results should not be over interpreted. For example, WSRT measures the flux of HI_{South} to be 5.1±0.2 Jy km s^{-1}. However, if one only measures the flux outside the Mundell et al. (1995) observation, and combines it with the Mundell et al. (1995) VLA flux of 2.42 Jy km s^{-1}, the summed synthesis observations give a flux of 6.0 Jy km s^{-1}. It is also worth noting that Mundell et al. (1995) measured a larger flux for HI_{North} than ALFALFA. However, the flux for HI_{North} is significantly blended with that of NGC 3227 in the ALFALFA data, so the artificially low flux of HI_{North} is likely due to conservative deblending. A reasonable deduction from these data is that a significant portion of the flux in the NGC 3227 subgroup is coming from the higher column density gas detected in synthesis observations.

ALFALFA detects fluxes significantly higher than those reported from WSRT in Serra et al. (2013), with the WSRT observations recovering between 43% and 88% of the ALFALFA flux for galaxies in HCG 44. However, it is worth noting that the ALFALFA fluxes for NGC 3187 and NGC 3190 individually contain significant uncertainty, since their emission is blended in the ALFALFA cubes. It is also important to note that the flux of NGC 3185 is likely significantly affected by RFI, in spite of care during source parameter extraction to mitigate this effect. The range in recovered fluxes may suggest that HCG 44 is surrounded by significant lower column density gas.

Notably, ALFALFA detects the entirety of the H I tail reported in Serra et al. (2013), and is unaffected by beam attenuation. Serra et al. (2013) report a total tail log H I mass of 8.71 after including HIPASS emission detected in re-reduced cubes. ALFALFA measures a total log H I tail mass of 9.05±0.03, 2.2× higher than the WSRT+HIPASS measurement, significantly more than their stated typical flux uncertainties of 10-20%.

3.5 Discussion

The ALFALFA maps of the NBG 21-6 region underscore the need for sensitive, wide field surveys to obtain a complete understanding of ongoing galaxy evolution in groups. Specifically, the detection of H I tails and bridges on scales larger than the group virial radius suggests strong ties between the evolution of galaxies in this region, and their group environment. Here we discuss the regional context of the sources presented above as evidence of ongoing hierarchical galaxy assembly.

3.5.1 HCG 44 in the Context of the NGC 3190 Group

Previous studies of the H I in the NGC 3190 group have focused on understanding the evolutionary state of HCG 44 in the context of of other compact groups. Verdes-Montenegro et al. (2001) propose an evolutionary sequence where a compact group's H I deficiency (Haynes et al., 1984) increases with time due to multiple tidal interactions, and find the the H I deficiency of the members of HCG 44 to be high relative to other compact groups.[i] Similarly,

Borthakur et al. (2010) and Borthakur et al. (2015) use the Green Bank Telescope to find evidence of diffuse H I in compact groups, but find that most of the gas in a 180×180 kpc (25′×25′) region surrounding the central galaxies of HCG 44 originates in high column density, disk-like structures. However, the apparent connection between NGC 3162 and HCG 44 in the ALFALFA data suggests that HCG 44 is best understood in the context of the entire NGC 3190 group.

Using H I synthesis maps, Serra et al. (2013) propose that the large H I feature originated due to tidal stripping, and suggest two specific origins: 1) within the compact group due to an interaction between NGC 3190 and NGC 3187, or 2) from an interaction between NGC 3162 and the members of the compact group during a close flyby. In the context of the entire group, the ALFALFA data strongly favor the second hypothesis.

Serra et al. (2013) suggest that if the H I feature originated in HCG 44, it could at least partially explain the observed H I deficiency. However, NGC 3162 dominates the H I mass budget of the NGC 3190 group, with more than 150% of the H I mass contained in NGC 3185, NGC 3187, and NGC 3190 combined. While a highly disruptive event could remove ~50% of the gas from e.g., NGC 3187, tidal forces should more easily remove ~20% of the gas from the outskirts of an H I-rich source like NGC 3162. Moreover, even after including the entire mass of HI_{Main}, HCG 44 is still H I deficient by more than a factor of six. This, suggests the members of HCG 44 were likely gas poor prior to an interaction with NGC 3162, which would make it even more difficult to remove the remaining, more tightly bound gas. Indeed, the potential detection of separate H I features

[i]Verdes-Montenegro et al. (2001) measure the H I deficiency of NGC 3185 and 3190 to be +1.0 (10% of the expected gas), and the H I deficiency of NGC 3187 to be +0.4 (40% of the expected gas). Serra et al. (2013) get values a factor of 2 more deficient using the relations of Toribio et al. (2011), but we note that this difference can be explained by a typo swapping radius and diameter in the Toribio et al. (2011) relations.

like $HI_{Secondary}$ is consistent with the idea that the group has experienced other tidal interactions. Thus, the group context suggests a scenario where the interaction with NGC 3162 is only one of the interactions responsible for the removal of gas from the members of HCG 44, and that NGC 3162 is the primary source of the gas in the H I feature, potentially delivered on a first infall to the group.

Further, the scale of the interactions surrounding HCG 44 suggests interesting questions for studies of other compact groups. Since not all tidal interactions favor the creation of massive tidal tails, the existence of a ~600 kpc tail suggests that groups with less fortuitously aligned interactions on similar scales should exist. Studies like Walker et al. (2016) have found only weak correlations between the total H I in compact groups (as observed with GBT) and the properties of individual galaxies. However, the GBT has a 9′ beam per pointing, and thus may miss significant group flux. In the case of HCG 44 ($\log M_{\mathrm{H\,I,total}} = 9.45$), the entire compact group fits within just a couple of GBT beam pointings, but neither the large H I tail ($\log M_{\mathrm{H\,I}} = 9.05$) nor NGC 3162 ($\log M_{\mathrm{H\,I}} = 9.65$) would be detected.

Thus, future wide-field surveys will be important for understanding the regions surrounding compact groups. While HCG 44 may be an extreme example, it presents a cautionary note that a full understanding of compact group scaling relations will likely require careful consideration of the surrounding ~1 Mpc via deep, wide field H I surveys.

3.5.2 Interactions in their Group Context

As discussed in section 3.4.1, the H I features in the NGC 3227 group suggest potential associations between NGC 3227 and other group members, including NGC 3213, UGC 5653, and the dwarf galaxies in close spatial proximity to the plumes. Similarly, the apparent connection between NGC 3162 and NGC 3190 makes it highly probable that they are at the same distance. In regions of the local universe with limited distance information, upcoming H I surveys will be an important tool for connecting sources with large distance uncertainties to those with primary distances. For example, a common way of determining group distances is to examine the Tully-Fisher relationship for the sources in the region (e.g. Figure 3.9 and the corresponding discussion in Section 3.5.3). However, stringent selection of galaxies for accurate distance determination (e.g. mostly edge on, similar Hubble types, etc.) often leaves too few sources for reliable distance determination, especially in compact groups where interactions may contribute to increased scatter in the relation. In these groups H I mapping coupled with stellar distance estimates from JWST will be an important source of reliable distances.

The potential tidal connection between sources separated by $\sim$ 300 kpc has potential consequences for searches for tidal dwarf galaxies. Mundell et al. (2004) report a potential TDG candidate in close proximity to NGC 3226/7. While the plumes in the NGC 3227 group do not show clear evidence of TDGs further out at our current resolution, they do indicate that searches for tidal dwarf galaxies may require imaging at significant separations from their parent galaxies. For example, Lelli et al. (2015) analyze VLA observations of 6 merging systems containing TDGs at cz<5000 km s^{-1}. The edges of the extended H I

emission in the NGC 3227 group would still extend just beyond the VLA primary beam if it were at D=70 Mpc (5000 km s^{-1}). More, numerical simulations predict differing numbers of potential tidal substrates per system (e.g. Bournaud & Duc, 2006; Yang et al., 2014), so understanding the full scale of each interaction will be important in validating these predictions.

3.5.3 Hierarchical Structure Formation in the NBG 21-6 Region

The assembly of structures via mergers at all scales is a key prediction of hierarchical structure formation models. Thus, the discovery of two large tidal systems in relatively close proximity (~1 Mpc) motivates an examination of the surrounding region as a potential example of galaxy evolution on multiple scales.

As discussed in section 3.2, the grouping of galaxies in the NBG 21-6 region depends on the scale used in the grouping algorithm. However, the histogram in Figure 3.2 suggests a potential connection between galaxies in the broader region. Figure 3.8 plots the recessional velocities from Figure 3.2 as a function of angular separation from the center of HCG 44 (HCG 44 was selected as the dynamical center since it has the largest velocity dispersion of the region). The narrow velocity structure (σ ~115 km s^{-1}) over large angular scales suggests the region may be experiencing significant infall onto a larger, filamentary dark matter structure, though there are currently too few distance measurements to confirm this suggestion.

As a rough diagnostic tool, Figure 3.8 also shows simple caustic curves calculated using $v = \sqrt{(GM/2r)}$ and assuming all sources are at a distance of 25 Mpc. The distribution of sources in the region approximately match the velocity dis-

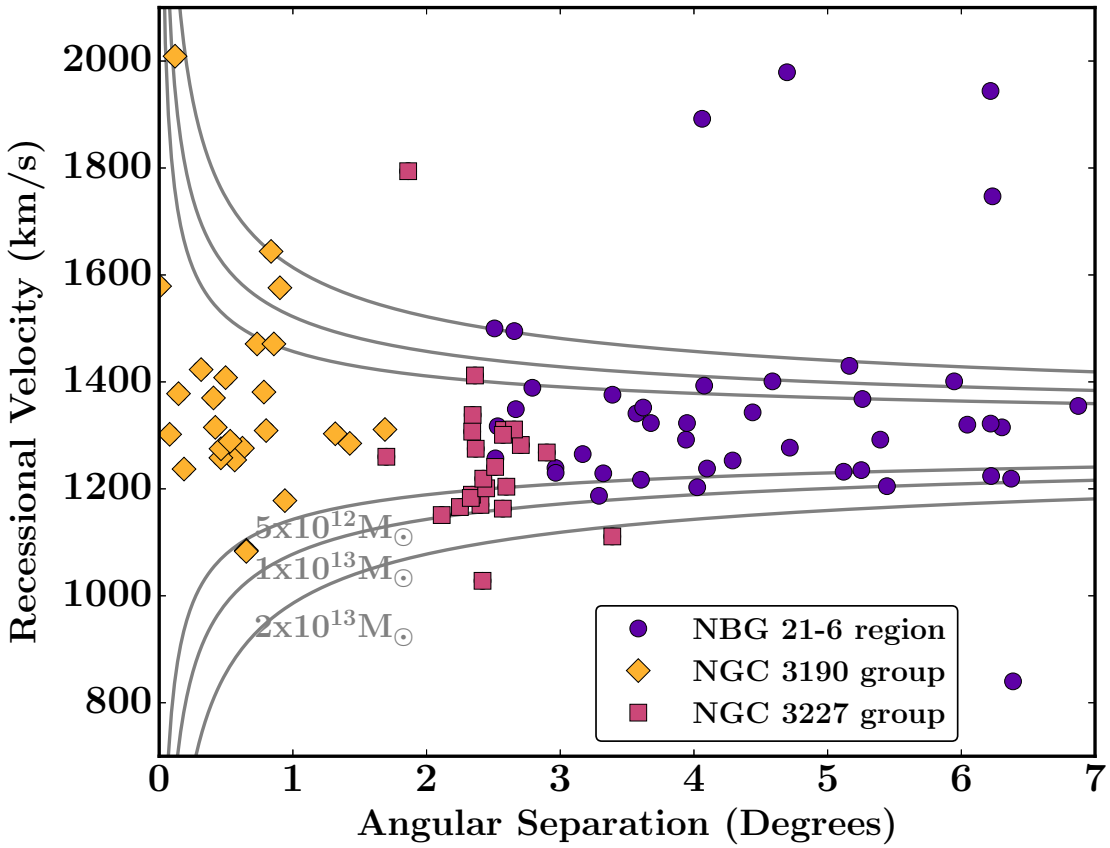

Figure 3.8: Angular separation on the sky versus recessional velocity for galaxies in the NBG 21-6 region, showing the dynamics of the larger region. Separations are measured from the center of HCG 44, which we take to be 154.5+22. Green squares are the galaxies associated with the NGC 3227 group, and red diamonds are those associated with the NGC 3190 group. Blue circles are the other galaxies within 7 degrees of the center of HCG 44. At a distance of 25 Mpc, 7 degrees corresponds to ~3 Mpc. Grey lines show simple caustic curves calculated using $v = \sqrt{(GM/2r)}$ (see Section 3.5.3).

tribution expected for a sources moving in a potential of M = $2{\times}10^{13} M_{\odot}$. Given the assumption of uniform distance and that this system is likely far out of equilibrium, these curves are at best suggestive. However, simple calculations of the dynamical mass of the NGC 3190 and and NGC 3227 groups using the median mass calculation defined in Heisler et al. (1985) estimate masses of 8.5 and $3.3{\times}10^{12} M_{\odot}$ respectively. We speculate that these estimates are consistent with a picture of the NGC 3190 and NGC 3227 groups as part of larger structure, falling toward the center of a larger common potential. Indeed, under the as-

sumption that the two groups are moving toward each other, each with a velocity $v = \sqrt{(G \times 2 \times 10^{13} M_{\odot}/(2 \times 1 \text{ Mpc}))} \approx 200$ km s^{-1}, the two systems will merge in ~3-4 Gyr.

If all the galaxies in the region are actually part of the same structure and at a similar distance, we would expect them to follow the Tully-Fisher relation between their apparent magnitude and their H I velocity widths. Figure 3.9 shows the Tully-Fisher relation for sources contained within by the $2{\times}10^{13} M_{\odot}$ caustics in this 6 Mpc diameter region. Optical magnitudes were taken from the NASA-Sloan Atlas[i] where available, since the NSA compensates for significant shredding issues in the SDSS pipeline magnitudes.[ii] They were converted to I-band magnitudes using the Lupton (2005) relations from the SDSS website, and corrected for internal and galactic extinction following Giovanelli et al. (1997c). NSA inclinations were checked by eyeball measurements, and any sources with $(b/a)_{NSA}$-$(b/a)_{eye} > 0.2$ were removed. H I velocity widths from ALFALFA were converted to total widths following Giovanelli et al. (1997c), and all sources with i<40 were removed from the sample. Assuming all sources are the same distance and follow the Tully-Fisher relation from Giovanelli et al. (1997c), we estimate the best fit distance to be 24.7±1.1 Mpc using a single parameter orthogonal distance regression fit to the data.

The black line shows the I-band Tully-Fisher relation and error budget from Giovanelli et al. (1997c) and Giovanelli et al. (1997b), for a distance of 25 Mpc. The scatter around the relation is consistent with all sources at the same distance for the small number of sources available. However, while this result is consistent with the interpretation of (almost) all of the sources in the region be-

[i] http://www.nsatlas.org/

[ii] The SDSS pipeline often de-blends nearby galaxies into several sources, thus underestimating the overall brightness. This issue is referred to as "shredding."

ing at the same distance, the lack of sources makes it impossible to strongly differentiate between that and significant distance scatter, since a source with W = 160 km s^{-1} in the background by 5 Mpc, would only lie ~1σ off the relation. Thus, this calculation demonstrates the difficulty of using secondary relations to determine group distance. Significant source statistics to perform this kind of analysis will have to await next generation deep H I and optical surveys, and improved understanding of the faint end of the baryonic Tully Fisher relation.

The collective optical properties of galaxies in the NBG 21-6 region are consistent with expectations for galaxies experiencing significant large scale infall in a hierarchical formation model. Most of the sources in the NBG 21-6 region are dwarfs with a r-band absolute magnitude of M_r>-18. Most sources in the region are H I rich (ALFALFA detects 73% of the galaxies with measured redshifts in NBG 21-6), and significantly bluer than the average SDSS population. Moreover, sources within the NGC 3190 and NGC 3227 groups may be slightly more processed than the other galaxies in the region. ALFALFA detects 81% of the 43 galaxies outside the two group, compared with 63% of the 36 galaxies inside the groups, while examination of the color distribution hints of that galaxies in the two groups appear to be somewhat redder than the other sources in the region (though this result is only marginally significant: a KS test on the two color distributions gives p = 0.08). The largest galaxies near the centers of the NGC 3190 and NGC 3227 groups appear to be the reddest sources in the region, and indeed, Appleton et al. (2014) discuss the importance of the green valley color of NGC 3226, demonstrating that the color cannot be explained by a recent resurgence of star formation, but rather must result from quenching of fairly recent star formation.

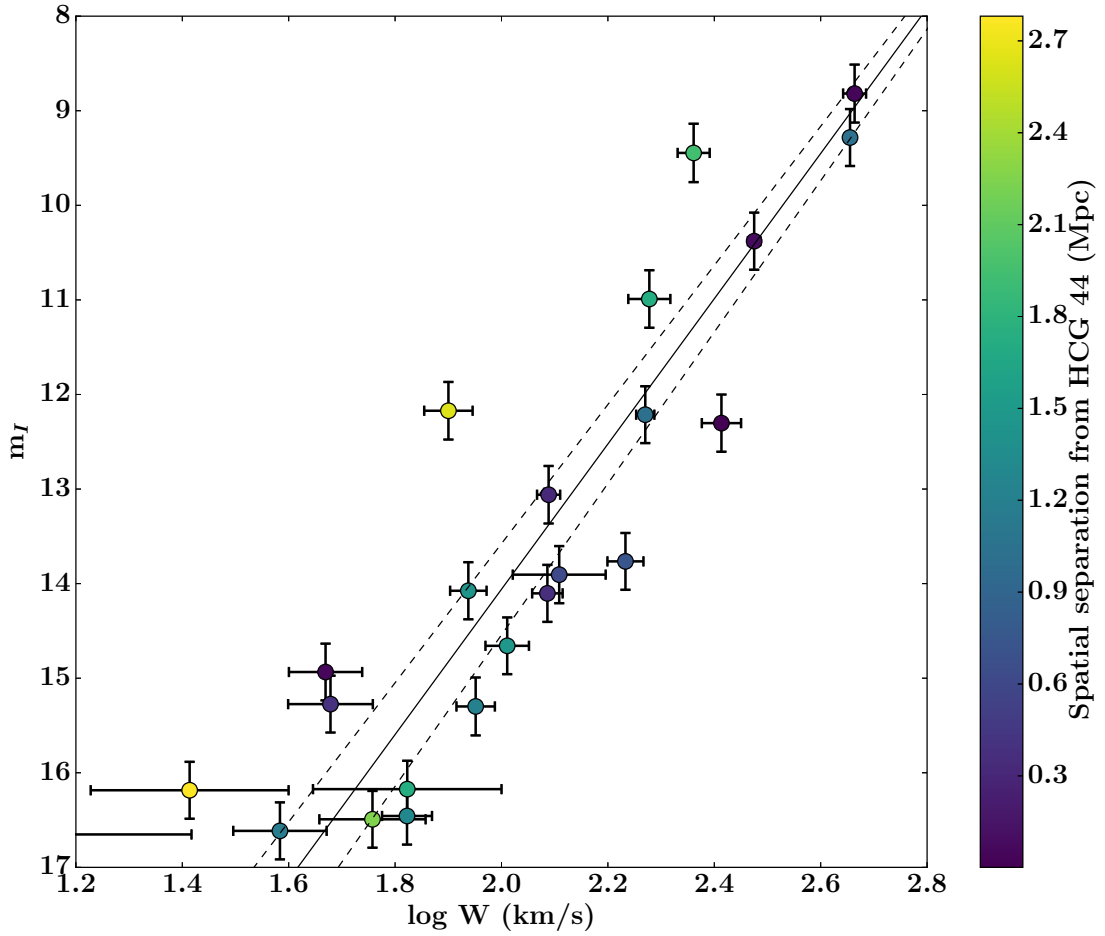

Figure 3.9: Tully Fisher relation for the galaxies within the $2 \times 10^{13} M_{\odot}$ caustic curves within R=3 Mpc of HCG 44, demonstrating the difficulty of TF methods for determining group distance. The observed sources are consistent with all being at the same distance, but due to the lack of qualifying sources with current survey data, this result is simply suggestive. Optical data were taken from the NASA-Sloan Atlas, and combined with the H I data from ALFALFA. The sample was corrected and culled following the procedure outlined in Giovanelli et al. (1997c), and discussed in section 3.5.3. The black line is the I-band relation from Giovanelli et al. (1997a) for a distance of 25 Mpc, with the dashed lines representing the 1σTF error budget discussed in Giovanelli et al. (1997b). The color axis represent the distance of the source from the center of HCG 44.

These observations together paint an observational picture that mirrors recent simulations of group and cluster formation in a hierarchical context. HCG 44, which shows the largest velocity spread in the region (NGC 3185 and NGC 3187 are separated by ~360 km s^{-1}), sits at the bottom of a larger potential well, with the other members of NGC 3190 delivering gas as they fall in. The merging pair NGC 3226/3227 rests near the bottom of a smaller potential that is falling toward the NGC 3190 well. Currently out of equilibrium, the region will continue to group and virialize as it makes its journey toward the Virgo cluster.

The lack of primary distance information and the poorly populated nature of these groups cautions against over-interpretation of the current data, since without accurate distance measurements, the possibility remains that velocity crowding gives the appearance of connection between unrelated sources. Further, in a hierarchical model, it is possible that interactions play a significant role in increasing the velocity dispersion of the NGC 3190 and NGC 3227 groups, effecting mass estimates. However, this caution suggests important synergies between upcoming optical surveys (which can deliver more and better understood primary distance measurements), and upcoming sensitive, wide field H I surveys in understanding this fortuitously aligned group, and others like it.

3.6 Conclusions

In this paper we presented sensitive, wide-field H I imaging of the NBG 21-6 region of the Leo Cloud of galaxies, observed as part of the ALFALFA H I survey, and follow up imaging of several regions using WSRT. We detect intra-group plumes that each extend over ~2 degrees (~600 kpc), far beyond the primary

beams of current synthesis telescopes. These features reveal interactions on larger scales than initially anticipated, providing an important tool for future modeling the recent history of these systems.

Specifically, the main conclusions of this paper are:

1. The detection of multiple >300 kpc H I appendages in a 2x2 Mpc area of the sky mapped by ALFALFA. We find that the large gas tail to the north of HCG 44 detected in Serra et al. (2013) is likely associated with NGC 3162, as speculated by those authors, and find a tentative detection of a second, superimposed tail associated with NGC 3187 and UGC 5574. We additionally find the H I plumes in the NGC 3227 group presented in Mundell et al. (1995) extend far beyond the observed primary beam, and report the detection of a third, clumpier feature to the NE of the system, which displays a prominent kink in WSRT observations, suggestive of additional interactions.

2. H I features without associated stellar counterparts make up a significant component of the group gas content in the groups considered here. The intra-group gas makes up 10% of the NGC 3190 group and 40% of the NGC 3227 group.

3. The NGC 3190 group (containing HCG 44) and the NGC 3227 group may be part of a larger, dynamically young region experiencing active infall, and may merge in ~3-4 Gyr. Examination of the broader group dynamics and optical colors suggests that its relatively local proximity and projection on the sky make the NBG 21-6 region an important laboratory for studying the role of ongoing galaxy interactions in the progression of group galaxies from the blue cloud to the red sequence.

Our observations emphasize the importance of wide-field, high sensitivity H I mapping. These massive, extended H I features were found in a region that had been extensively studied in H I; without the powerful combination of sensitivity, resolution, and field of view of ALFALFA we would not have been able to trace galaxy interactions in these large scales. Wide field, deep mapping with next generation H I detectors like the Square Kilometer Array Pathfinders (see Giovanelli & Haynes, 2016) will be necessary for a full understanding of galactic evolution in the group environment.

CHAPTER 4

(ALMOST) DARK HI SOURCES IN THE ALFALFA SURVEY: THE INTRIGUING CASE OF HI1232+20

4.1 Introduction

Low surface brightness (LSB) galaxies are difficult to detect optically, and thus may be underrepresented in most optically-selected samples used in studies of galaxy formation and evolution and their hierarchical assembly history (e.g., Williams et al. 1996, Madau et al. 1998, McGaugh et al. 2000, Brinchmann et al. 2004, Hopkins & Beacom 2006). Some of the LSB galaxies might be those in which star formation has been a slow and gradual process (McGaugh & de Blok 1997, Schombert & McGaugh 2014) and some may provide a source of fresh gas infall to larger galaxies through merger and interactions (Sancisi et al., 1990). By missing the LSB galaxies in most surveys, we may be missing an entire population of galaxies and/or a phase of galaxy evolution.

At the extreme end of the LSB galaxy spectrum, Disney (1976) predicted the existence of entirely "dark galaxies" with no observable optical stellar counterparts because their surface brightness is too low. A category of "crouching giants," exemplified by the highly luminous and massive LSB spiral Malin I (e.g., Lelli et al., 2010), has been identified, but they are quite rare. Overall, no large population of unseen LSB objects has been detected at any wavelength.

This chapter is an adapted version of the published article Janowiecki et al. (2015). This paper was a fully collaborative effort, with both Dr. Janowiecki and I contributing equally to this effort. Dr. Janowiecki is the optical expert, and contributed the optical analysis to the paper, and I was the H I expert, and contributed the H I analysis.

LSB galaxies typically possess substantial reservoirs of atomic hydrogen, so blind 21-cm surveys represent the best opportunity to find large populations of the most extreme LSBs. Two major blind H I surveys, HIPASS (H I Parkes All Sky Survey, Doyle et al. 2005) and ALFALFA (Arecibo Legacy Fast ALFA, Haynes et al. 2011), have reached the conclusion that there is not a significant population of gas-bearing but optically dark systems. At the same time, there are a number of intriguing, unexplained objects detected clearly in HI, showing signs of ordered motion and coincident with no discernible stellar counterpart The best example of such a "dark galaxy" remains the southwestern component of the HI1225+01 system (Chengalur et al., 1995; Matsuoka et al., 2012), although it is important to note its presence in a common envelope with a visible star forming dwarf companion.

While some simulations can produce dark galaxies in the form of stable gas disks that never produce stars (Verde et al., 2002), others find that star-less galaxies cannot exist for very long before becoming unstable to star formation (Taylor & Webster, 2005). The presence of H I in some LSB galaxies provides a key dynamical tracer of the mass in these extreme systems (Geha et al. 2006, Huang et al. 2012b). Detailed kinematic studies are being undertaken to study the effects of outflows and feedback in lower mass galaxies, (van Eymeren et al., 2009), in order to understand star formation modes in these shallow potential wells and low density galaxies. Groups have worked to develop models that can simultaneously explain galaxy scaling relations in the full cosmological context (e.g., Dutton et al. 2007).

Recently, the ALFALFA survey has made significant improvements in the sensitivity and depth of available wide-field blind H I surveys. ALFALFA has

measured 25,000+ HI sources over 7000 square degrees in a cosmologically significant volume (Giovanelli et al. 2005, Haynes et al. 2011, Jones et al. in prep.). ALFALFA has characterized the population of normal galaxies (Huang et al., 2012a), low mass galaxies (Huang et al., 2012b), as well as probing the H I mass function to lower H I masses than ever before (Martin et al., 2010).

As discussed in Cannon et al. (2015), the ALFALFA (Almost) Dark Galaxy Project has been studying the very small fraction (~0.4%) of HI sources which lack obvious optical counterparts and are isolated from other sources. Followup observations are ongoing and include deep optical imaging and H I synthesis maps. Many objects turn out to be tidal in origin, but some have very low surface brightness stellar populations at or below the detection limits of current wide field imaging surveys.

In this work we study the newly discovered HI1232+20 system of three (almost) dark extragalactic H I sources which were not detected in optical surveys, and are at least an order of magnitude less luminous than previously studied LSB galaxy populations (e.g., Schombert et al. 2011). This paper is organized as follows. In Section 4.2 we describe the discovery and observations of this system, and in Section 4.3 we show the results of those observations. Throughout this work we use a flow model distance (Masters, 2005) of D=25 Mpc to the HI1232+20 system, and we discuss the effects of distance uncertainty on our conclusions in Section 4.3.4. In Section 4.4 we discuss the implications of these objects and what they might mean in the context of (almost) dark galaxies, and in terms of extending scaling relationships from normal galaxies. Section 4.5 contains a brief summary of our main results. Throughout this work we assume a ΛCDM cosmology, with $\Omega_{\rm m}$=0.3, Ω_{Λ}=0.7, and H_0=70 km s^{-1} Mpc^{-1}.

4.2 Observations

4.2.1 ALFALFA Discovery of the HI1232+20 System

The ALFALFA survey employs a two-pass, fixed azimuth drift scan strategy, the details of which are described in previous papers (Giovanelli et al. 2005, Saintonge 2007, Martin et al. 2009, Haynes et al. 2011). All data are flagged for radio frequency interference (RFI) interactively, and each grid is examined by hand to confirm and improve on sources detected via the automated methods of Saintonge (2007); final source parameters are measured and cataloged interactively.

Among the ALFALFA (almost) dark extragalactic sources, the HI1232+20 system (comprised of sources AGC 229383, AGC 229384, and AGC 229385) was found to be of particular interest. These three objects are near each other on the sky and also have similar recession velocities, so are likely associated with each other. From the ALFALFA observations it was clear that these three sources have significant amounts of gas present, even though they do not have readily identifiable optical (stellar) counterparts in existing optical databases (SDSS, DSS). While they appear on the sky near AGC 222741 (CGCG 129-006), there is a significant separation in velocity between the sources. AGC 222741 has an H I recession velocity of 1884 km/s while the three sources in this sample have recession velocities of ~1300 km/s.

An overlapping archival ultraviolet (UV) image from GALEX GR7 (Galaxy Evolution Explorer, Martin et al. 2005, Morrissey et al. 2007, Data Release 7, Bianchi et al. 2014) shows a faint diffuse UV source at the coordinates of AGC 229385 (see Section 4.2.4 for more details). There is also a hint of a faint

object at the same position in the DSS2-B image (Digitized Sky Survey[i]) but no source visible at that position in images from SDSS DR9 (Sloan Digital Sky Survey, Data Release 9, Ahn et al. 2012). Tables 4.1 and 4.2 contain information about the HI1232+20 system. No optical sources were evident at the locations of the other two H I detections.

Given the curious nature of this system, we have carried out further observations to study it in more detail. We have obtained deep optical images to look for possible faint stellar populations in the sources, and sensitive H I synthesis observations to resolve the gas distribution and kinematics in more detail.

[i]The Digitized Sky Surveys were produced at the Space Telescope Science Institute under U.S. Government grant NAG W-2166. The images of these surveys are based on photographic data obtained using the Oschin Schmidt Telescope on Palomar Mountain and the UK Schmidt Telescope. The plates were processed into the present compressed digital form with the permission of these institutions.

Table 4.1. Observed H I parameters of the HI1232+20 system

AGC	Position J2000	$F_{HI,ALFALFA}$ [Jy km s^{-1}]	F_{HI} [Jy km s^{-1}]	V_{50} [km s^{-1}]	W_{50} [km s^{-1}]	R_{HI} [′]	$R_{5\times10^{19}}$ [′]
(1)	(2)	(3)	(4)	(5)	(6)	(7)	(8)
229385	12:32:10.3 +20:25:24	4.87 ± 0.04	4.84 ± 0.04	1348 ± 1	34 ± 1	1.60 × 0.72	1.87 × 1.10
229384	12:31:36.4 +20:20:06	1.36 ± 0.03	1.25 ± 0.04	1309 ± 1	27 ± 1	0.73 × 0.55	1.00 × 0.70
229383	12:30:55.3 +20:34:04	0.81 ± 0.06	0.42 ± 0.05	1282 ± 4	59 ± 8	···	0.80 × 0.28

Note. — Observed properties of objects in HI1232+20. (1) Catalog ID in the Arecibo General Catalog (an internal database maintained by M.P.H. and R.G.) (2) H I centroid position from WSRT (3) Total integrated H I line flux density measured from ALFALFA data (4) Total integrated H I line flux density measured from WSRT data (5) Heliocentric velocity, measured at the 50% flux level (6) H I velocity width, measured at the 50% flux level (7) H I radius at a H I surface density of 1 $M_\odot$ pc^{-2} (corresponding to an H I column density of 1.25×10^{20} cm^{-2}), in arcminutes, measured from the moment 0 maps assuming a beam of 13″×39″. Uncertainties on all radius measurements are ±0.06′. At a distance of 25 Mpc, 1′ subtends a distance of 7 kpc. Note that AGC 229384 is separated into two peaks at the 1$M_\odot$ pc^{-2} level, and that AGC 229383 never reaches a surface density of 1$M_\odot$ pc^{-2}. Also note that the measurement for AGC 229383 only reflects the radius of the NW clump; the SE clump reaches a column density of 5×10^{19} over an area of 14″×7″. (8) H I semimajor and semiminor axis at a column density of 5×10^{19} cm^{-2}, in arcminutes, assuming a beam of 13″×39″.

4.2.2 Deep Optical Imaging with WIYN pODI

The HI1232+20 system was observed with the WIYN[ii] 3.5-m telescope at Kitt Peak National Observatory[iii] using the partially populated One Degree Imager (pODI). Currently, pODI is made up of 13 Orthogonal Transfer Arrays (OTAs), each of which is made of sixty-four 480x496 pixel cells. The OTAs are arranged on the focal plane such that the central 3x3 OTAs cover an area of $24' \times 24'$ with pixels that are 0.11'' on a side. The numerous gaps between cells and OTAs require a series of offset dithered exposures to produce a well-sampled image. Four of the standard Sloan Digital Sky Survey (SDSS, Gunn et al. (1998), Doi et al. (2010)) g',r',i', and z' filters are available, and stars from the SDSS catalog photometry are used for standard photometric calibrations.

We imaged an area which includes both AGC 229384 and AGC 229385 on the night of 6 February 2013 with nine dithered 300 second exposures in each of the $g'r'i'$ filters. We observed AGC 229383 on 2 May 2014 with nine dithered 300 second exposures in both the g' and r' filters. By combining data from these two nights of observations, we have contiguous deep multi-wavelength imaging coverage over an area $\sim 40' \times 40'$. We also imaged this field with an 80 narrow-band Hα filter during photometric conditions on the night of 6 February 2013. Our dithered sequence of nine 300s images, while not calibrated, do not show any Hα detections at the locations of the three H I sources in the HI1232+20 system, but do show a background spiral galaxy (AGC 222741) quite clearly.

We reduced our observations using the QuickReduce (QR, Kotulla 2014)

[ii]The WIYN Observatory is a joint facility of the University of Wisconsin-Madison, Indiana University, the University of Missouri, and the National Optical Astronomy Observatory.

[iii]Kitt Peak National Observatory, National Optical Astronomy Observatory, which is operated by the Association of Universities for Research in Astronomy (AURA) under cooperative agreement with the National Science Foundation.

Table 4.2: Derived properties and limits from observations

Quantity [units]	AGC 229383	AGC 229384	AGC 229385
$m_{g'}$ [mag]	> 20.7	> 20.7	19.20 (0.03)
$m_{r'}$ [mag]	> 20.2	> 20.5	19.27 (0.03)
$m_{i'}$ [mag]	$\cdots$	> 19.7	19.36 (0.04)
$\mu_{g',\mathrm{peak}}$ [mag/arcsec^2]	> 27.8	> 27.9	26.4 (0.1)
$\mu_{r',\mathrm{peak}}$ [mag/arcsec^2]	> 27.3	> 27.7	26.5 (0.1)
$\mu_{i',\mathrm{peak}}$ [mag/arcsec^2]	$\cdots$	> 26.8	26.1 (0.1)
Optical A x B (at $\mu_{g'}$=27) [kpc]	$\cdots$	$\cdots$	7×3
HI A x B (at $5{\times}10^{19}$cm^2) [kpc]	12×4	14×10	28×16
$M_{g'}$ [mag]	> -11.3	> -11.3	-12.89
$M_{r'}$ [mag]	> -11.8	> -11.5	-12.79
$M_{i'}$ [mag]	$\cdots$	> -12.3	-12.69
$g' - r'$ [mag]	$\cdots$	$\cdots$	-0.09
$B - V$ [mag]	$\cdots$	$\cdots$	0.13
M_B [mag]	> -11.2	> -11.1	-12.72
L_{FUV} [$L_\odot$]	$\cdots$	$\cdots$	2.41×10^7
L_{NUV} [$L_\odot$]	$\cdots$	$\cdots$	2.66×10^7
SFR_{NUV} [M$_\odot$/year]	$\cdots$	$\cdots$	4.1×10^{-3}
SFR_{FUV} [M$_\odot$/year]	$\cdots$	$\cdots$	6.9×10^{-3}
$\log M_{HI}$ [$\log M_\odot$]	8.08	8.30	8.86
$M_\star$ [M$_\odot$]	$<3.7 \times 10^5$	$<3.4 \times 10^5$	1.5×10^6
$M_{HI}/M_\star$	> 320	> 580	290
$M_{HI}/L_{g'}$ [$M_\odot/L_\odot$]	> 31	> 57	45.8
M_{HI}/L_B [$M_\odot/L_\odot$]	> 26	> 48	38.2

Apparent magnitudes ($m_{g'}$, $m_{r'}$, $m_{i'}$) are not corrected for Galactic extinction. Absolute magnitudes ($M_{g'}$, $M_{r'}$, $M_{i'}$, M_B) luminosities (L_{FUV}, L_{NUV}), and colors ($g' - r'$, $B - V$) are corrected for Galactic extinction from Schlafly & Finkbeiner (2011). All absolute quantities assume a distance of 25 Mpc. M_B and $B - V$ are determined from conversions in Jester et al. (2005). Upper limits are determined where sources are not detected in pODI observations and are at 3σ confidence levels. Uncertainties on measured quantities are indicated in parentheses.

data reduction pipeline, and supplemented this processing with an additional illumination correction. QR was run interactively in the One Degree Imager Pipeline, Portal, and Archive (ODI-PPA)[iv] science gateway (Gopu et al. 2014, Young et al. 2013). The PPA interface allows the user to select which observations will be reduced, and runs all of the reductions on computing resources at the Pervasive Technology Institute (PTI) at Indiana University.

The QR pipeline includes: masking of saturated pixels, crosstalk, and persistence; overscan subtraction; bias level subtraction; dark current subtraction; non-linearity corrections to each cell; flat field correction from dome flat fields; cosmic-ray removal; fringe removal (in *i'*); pupil ghost correction. However, the final pipeline-processed data still have uncorrected instrumental artifacts in them, especially at very faint intensity levels. In order to produce images that are suitable for low surface brightness analysis, we need to correct for the small gradients, sky level offsets, and other artifacts in particular cells. Once these effects are corrected, the dithered images can be combined into a final deep image.

In order to remove these image artifacts, we apply an illumination correction using dark sky flats generated from the observations themselves. For a particular filter, we mask all objects in the images, then use a median algorithm to combine all of the exposures into a dark sky flat field, which is then smoothed with a 3×3-pixel smoothing element. Each exposure is then divided by this illumination correction image.

Before combining all exposures in a dither pattern, we re-project them to

[iv]The ODI Pipeline, Portal, and Archive (ODI-PPA) is a joint development project of the WIYN Consortium, Inc., in partnership with Indiana University's Pervasive Technology Institute (PTI) and with the National Optical Astronomy Observatory Science Data Management (NOAO SDM) Program.

a common pixel scale and also scale the images to a common flux level using measurements of stars in the field and SDSS DR9 catalog magnitudes (Ahn et al., 2012). This compensates for varying sky transparency during the dither sequence, and typically yields final photometric zeropoints with standard deviations of 0.02 – 0.03 magnitudes. The g' filter calibrations required a g'-i' color term of amplitude 0.079 ± 0.013, but r' and i' calibrations required no color term. The point sources in our final combined images have an average FWHM of $0.7'' - 0.9''$.

We also create a deep "detection-only" image by combining all images from both pointings in all filters to reach the faintest light possible. This detection image is then binned to 1.2″ resolution to bring out very faint emission, and is shown in Figure 4.1 with relevant H I sources labeled and H I synthesis contours overlaid. The contrast levels in this image have been stretched to show the exquisite sensitivity to faint light. In this view, the optical counterpart to AGC 229385 is strikingly visible, as will later be discussed. Also visible in the upper left corner of the image is diffuse filamentary emission from Galactic cirrus. This foreground emission comes from reflections of star light off cold dust clouds in our Galaxy (Sandage 1976, Witt et al. 2008). Multiple infrared surveys (IRAS, Schlegel et al. 1998, WISE, Wright et al. 2010) also observe this dust via its thermal emission, and show features that are coincident with the faint optical emission we see in our image. It even shows up weakly in the overlapping deep archival GALEX UV image. Galactic cirrus is very faint and diffuse at optical wavelengths and typically only visible in deep, wide-field images that are very accurately flat-fielded (e.g., Rudick et al. 2010).

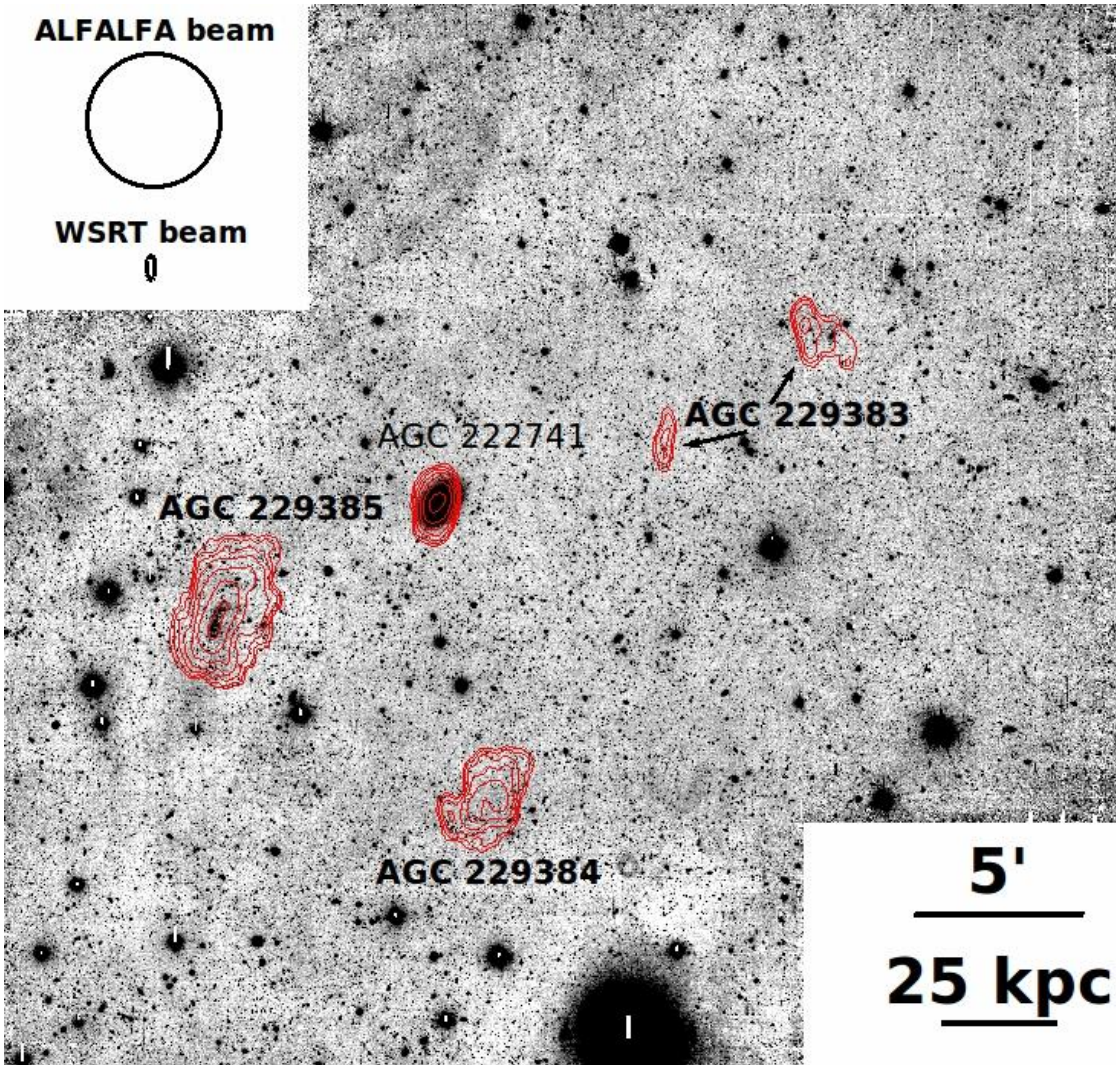

Figure 4.1: Detection image made from all pODI observations with ALFALFA H I sources in the HI1232+20 system labeled and WSRT contours overlaid in red. The size of the ALFALFA and WSRT beams are indicated by the shapes at the top left corner. The WSRT pointings cover nearly the entire area region shown in this image. The optical image is binned 12×12 pixels so that the resulting pixels are 1.3″ on a side, and is aligned north up east left. The WSRT contours show column densities spaced logarithmically between 1 and $64{\times}10^{19}$ cm^{-2}. The tight packing of the lowest contours is likely a result of sigma-clipping, and not a sharp edge in the HI distribution. See Section 4.2.3 for more details and about sensitivity differences across the image. The spiral galaxy AGC 222741 has a recession velocity of cz=1884 km/s, so is significantly more distant than the objects in the HI1232+20 system, which have recession velocities around cz~1300 km/s (see Section 4.3.4 for details). The WSRT contours of AGC 229383 show that it is separated into two components at this sensitivity level, as is discussed further in Section 4.3.3. Also visible at the top left of the image is diffuse filamentary emission from Galactic cirrus, which coincides with features seen in far-infrared and ultraviolet images of the same area.

4.2.3 HI Synthesis Imaging with WSRT

We observed the HI1232+20 system with four 12h pointings at the Westerbork Synthesis Radio Telescope (WSRT), three of which were centered on (12:31:52.6 +20:22:59) to encompass the centroids of AGC 229385 and AGC229384, and one of which was centered on (12:31:08.5 +20:31:41.9), to encompass AGC 229383. The primary beams of the two pointing centers are 35′ wide and cover nearly all of the area displayed in Figure 4.1. We observed the H I line in one band with 10 MHz bandwidth, two polarization products, and 1024 channels, ensuring a broad range of line free channels for continuum subtraction and a velocity resolution of 4.12 km s^{-1} after Hanning smoothing.

The data were reduced using the same automated data reduction pipeline as applied in Wang et al. (2013), originally used by Serra et al. (2012), using the data reduction software Miriad (Sault et al., 1995) wrapped into a Python script. The data were automatically flagged for radio interference using a clipping method after filtering the data in both the frequency- and time-domain. After the primary bandpass calibration, the data were iteratively deconvolved with the CLEAN algorithm, using clean masks determined on the cube with decreasing clip levels, to then apply a self-calibration. The calibration solution was applied to the visibilities and the continuum was subtracted in the visibility domain to then invert the data after Hanning smoothing, using a set of combinations of Robust weighting and tapering with a Gaussian kernel, as well as a binning in the frequency domain. Finally the data cubes were iteratively cleaned using clean masks determined by filtering the data cubes with Gaussian kernels and applying a clip level. The clean cutoff level was set to the rms noise in the data cubes. Because we hence cleaned the data comparably deeply,

no correction of the intensity levels of the residuals was made.

Our pipeline produces cubes at each centroid with three different robustness weightings, $r = 0.0$, $r = 0.4$, and $r = 6.0$, binned to a velocity resolution of 6.2 km s^{-1} after Hanning smoothing (12.4 km s^{-1} for the $r = 6.0$ cube). The noise level in the cubes for the three respective robustness weightings are 0.40, 0.36, and 0.24 mJy/beam/channel, with beam sizes of 39″×13″, 45″×15″, and 54″×20″.

For each cube we then created H I total flux maps by summing masked cubes along the velocity axis. We created the masks by smoothing the images to twice the beam size, and then keeping any pixel 3σ above the noise level. From these we calculate H I column density maps assuming optically thin H I gas such that $N_{HI}=1.823 \times 10^{18} \int T_b dv$ cm^{-2}. Since the final contour map results from the combination of multiple WSRT observations (3 at the SE pointing, and 1 at the NW pointing), the signal-to-noise ratio varies across the image and is less sensitive near AGC 229383. The lowest H I contour shown on the images, 1×10^{19} cm^{-2}, corresponds to a less significant detection in the region around AGC 229383 than it does in the region around AGC 229385 and AGC 229384. As a result, there were locations outside of the main signal from AGC 229383 where the H I column density exceeded 1×10^{19} cm^{-2}, but since the significance of the detection was $<3\sigma$, those contours are not shown.

We additionally create a one dimensional integrated H I line profile for each object, as displayed in Section 4.3. We fitted the line with both the two horned function applied in the ALFALFA data processing, and using a standard Gaussian fit and note that the fluxes from the fits match well within random errors. We recover 99% of the ALFALFA flux in the WSRT spectrum of

AGC 229385, and 92% in AGC 229384, but only 52% in AGC 229383. The spectra for AGC 229385 and AGC 229384 are both well fitted by a Gaussian profile, and though both may show slight deviation from Gaussian, using two Gaussians does not return a better result. The spectrum for AGC 229383 is not well fitted by either a Gaussian or a two-horned fit.

Finally, we produce H I velocity maps using two different methods. We created standard moment 1 maps from cubes masked at 3σ, and additionally fitted Gaussian functions to each individual profile in the datacube using the GIPSY task XGAUFIT. The resulting maps from the two methods are virtually identical, and we show the maps in Section 4.3.

To further analyze the velocity field we create Position-Velocity (PV) diagrams for each source. We produced the PV diagrams by taking an 18″ (1 minor axis beam width) wide slice along the H I major axis centered on the H I surface density centroid. We measured the position angle and centroid from the surface density profile since the variations in the velocity field leave the major velocity axis and center uncertain. We note that none of the PV diagrams change significantly for small variations in position angle or slice width.

4.2.4 Archival GALEX Observations

AGC 229385 (the strongest H I detection of the HI1232+20 system) had a very faint UV counterpart visible in an archival dataset from GALEX (Martin et al. 2005, Morrissey et al. 2007). GALEX obtained images in the far ultra-violet (FUV) from 1344 to 1786 with 4.3″ FWHM resolution, and in the near ultra-violet (NUV) from 1771 to 2831 with 5.3″ resolution. These UV images are es-

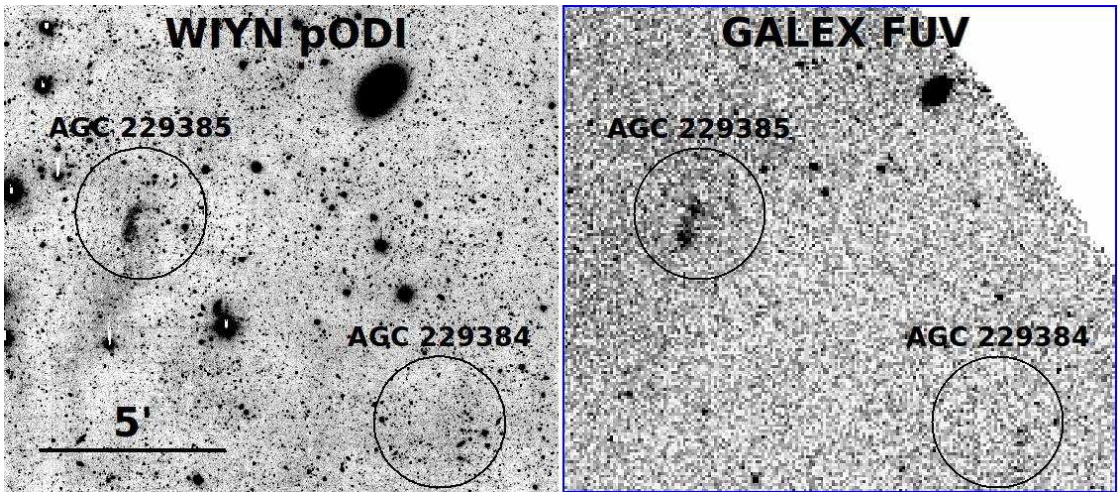

Figure 4.2: Comparison of WIYN pODI image and GALEX FUV image. The pODI detection image is binned 12 × 12 so that pixels are 1.3″ on a side. The FUV image has been binned 3 × 3 so that pixels are 13″ on a side. Two of the three H I sources in the HI1232+20 system are labeled on both panels with 3′ circles, the size of the ALFALFA beam. AGC 229385 clearly has an optical and ultraviolet counterpart while AGC 229384 lacks a counterpart at either wavelength. AGC 229383 has not been observed by GALEX.

pecially sensitive to young stellar populations, and should help to identify sites of recent star formation.

AGC 229385 was imaged by GALEX in May 2007 in the NUV and FUV bands, with exposure times of 1145s in both bands. A set of matched images is shown in Figure 4.2, with data from pODI WIYN and GALEX FUV. The locations of AGC 229385 and AGC 229384 are shown in these images, while AGC 229383 lies outside of any archival GALEX image. The brightest H I source, AGC 229385, is faintly visible in the UV image as a diffuse source. However, the GALEX pipeline (GR7, Bianchi et al. 2014) does not identify this diffuse object as a source, instead shredding it into multiple point sources. We measure the brightness of AGC 229385 in the FUV and NUV images ourselves in an aperture matched to our optical images, as discussed in Section 4.3. There is no source visible in the FUV image at the position of AGC 229384.

4.3 Results

In the following sub-sections we describe the results of our followup observations for the HI1232+20 system. The derived results are summarized in Table 4.2. We also consider the environment around this system, and uncertainties in the adopted distance.

4.3.1 AGC 229385

Figure 4.3 shows our observations of AGC 229385. Figure 4.3a is a deep 3-color image from WIYN pODI with contours from our WSRT HI synthesis map at the highest resolution (39″×13″). Figure 4.3b shows a zoomed-in region around the optical counterpart with the regions we use to measure its surface brightness indicated by black squares. The optical emission from AGC 229385 appears very blue, and coincides spatially with the peak of the H I distribution. The optical component appears ∼5× less extended than the radio emission, but both are similarly elongated in the northeast-southwest direction.

AGC 229385 has an unusual optical morphology that is not simple to describe. The optical counterpart is elongated in the N-S direction, but has a nearly constant surface brightness across its entire extent. We fitted an ellipse to the 5σ contour on the g' image and found a semi-major axis of 32″ and semi-minor axis of 10″. This 5σ ellipse has a position angle of 15° (measured clockwise from N) and an ellipticity (ϵ=1 − b/a) of ϵ=0.68.

After attempts to fit elliptical annuli to the optical images of AGC 229385 resulted in inconsistent and divergent surface brightness profiles, we decided to

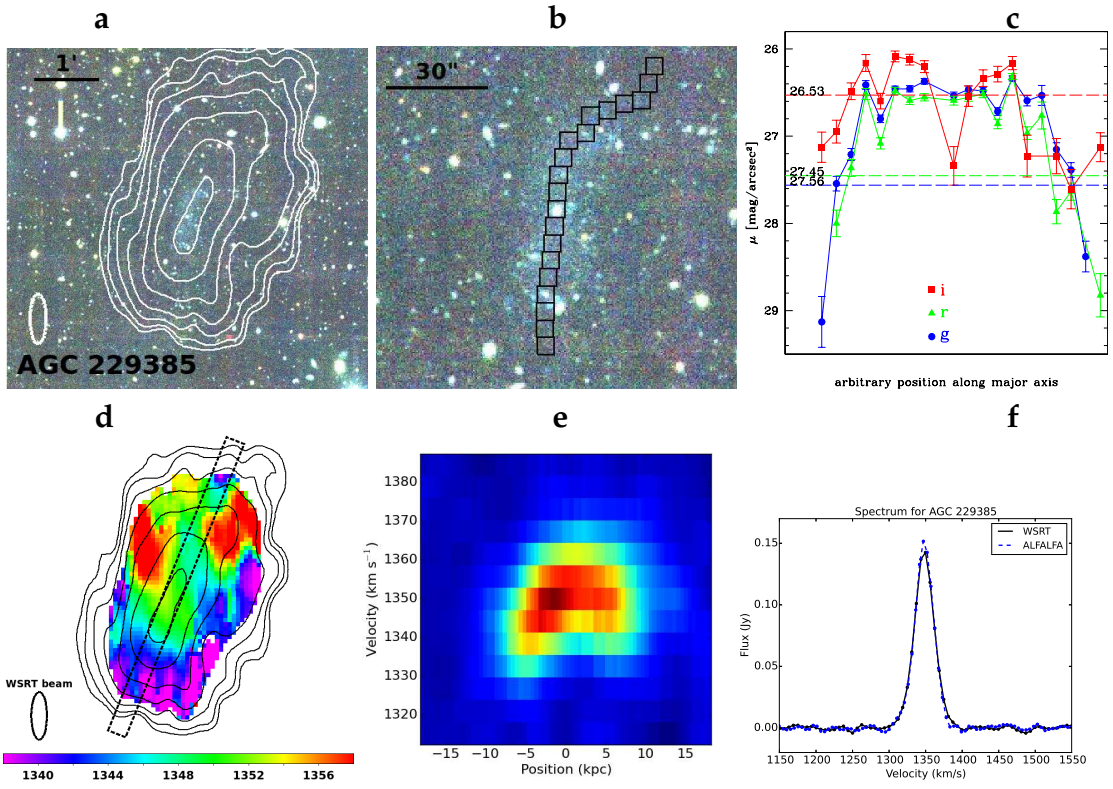

Figure 4.3: Our observations of AGC 229385. a) 3-color optical image from WIYN pODI binned 4×4 so that pixels are 0.44″ on a side. North is up, East is left, and the angular scale is indicated on the image. White contours of HI emission are from WSRT and are at are at 1, 2, 4, 8, 16, 32, and 64×10^{19} atoms cm^{-2}, and the white ellipse at the bottom left shows the size and shape of the WSRT beam. b) Zoomed-in view of the WIYN pODI observations, with black boxes indicating regions used for surface brightness measurements. c) Surface photometry for AGC 229385 from pODI images in g', r', and i' filters, measured in 5″ × 5″ boxes following the brightest part of the optical emission, after masking obvious stars and background galaxies. Dashed lines show the 3σ surface brightness detection limits in each filter. Blue points and lines indicate g' filter measurements, green indicate r' measurements, and red indicate i' measurements. d) XGAUFIT velocity field from WSRT with the same H I contours as above. The ellipse in the bottom left corner indicates the size and shape of the WSRT beam. The dashed rectangular region shows the slice along the major axis which is used to generate the P-V diagram. e) Position-Velocity diagram from WSRT. f) ALFALFA and WSRT H I spectra of AGC 229385. As discussed in the text, H I fluxes from ALFALFA and WSRT are in good agreement. Blue dashed lines represent the ALFALFA spectra, while the solid black lines show the WSRT $r = 0.4$ spectra.

measure the surface brightness in small regions instead. We measured the optical surface brightness of AGC 229385 in 5″ × 5″ regions following the curving shape of this source from south to north, after masking all obvious foreground

and background sources. These regions are shown as black boxes in Figure 4.3b. We also placed similar regions outside the periphery of the source to determine the local sky value. The surface brightness traces along AGC 229385 are plotted in the Figure 4.3c. We calculated the surface brightness level that corresponds to 3 times the standard deviation in the sky, and label it as the 3σ detection threshold. The g' surface brightness profile has the highest signal-to-noise ratio, and is well above the 3σ level. The r' profile is weaker but still well-measured. In i', this source is only weakly detected, but still is above the 3σ surface brightness level. In all three filters a similar profile shape is seen as the outlying regions show very little signal and the inner regions show a relatively flat brightness distribution across the source. To estimate a peak surface brightness value in each filter we use the measurements from the three boxes just south of the bright foreground star near the center of AGC 229385, where there are relatively few contaminating sources which had to be masked and the profiles are relatively smooth. The peak values are calculated by averaging the measurements in these three boxes, and are 26.4, 26.5, and 26.1, in g',r', and i', respectively. While the formal uncertainties on these surface brightness measurements are low ($\sim$3$-$5%, owing to our accurate photometric calibrations and the good S/N of the optical counterpart), the variations between adjacent boxes can be as high as 0.1 mag. Accordingly, we assign an uncertainty of 0.1 mag to these peak values. We also measure photometry of this source in a 32″ radius aperture after masking obvious foreground and background sources. The results of the surface and aperture photometry of all three sources are summarized in Table 4.2.

The H I synthesis observations from WSRT (shown in the bottom row of Figure 4.3) are also difficult to interpret. The moment 0 map, Figure 4.3d, shows an H I source significantly more extended than its optical counterpart. AGC 229385

has H I major and minor axes of 3.2′×1.4′ measured at an H I surface density of 1 $M_\odot/\mathrm{pc}^2$ (corresponding to a column density of $12.5 \times 10^{19}\mathrm{cm}^{-2}$), or 24 kpc ×10 kpc assuming a distance of 25 Mpc. WSRT measures significant emission at lower column densities, out to $3.7' \times 2.2'$ or 28 kpc ×16 kpc at $5 \times 10^{19}\mathrm{cm}^{-2}$ and a furthest extent of ∼5′ at $10^{19}\mathrm{cm}^{-2}$.

The exact surface density profile of AGC 229385 is subject to its 3D geometry and inclination, which are difficult to determine conclusively given our beam size and the unusual nature of AGC 229385. AGC 229385 appears to have an H I position angle of 21° which gives $\sim 6 \times 7$ resolution elements at the furthest extent along the major and minor axes. We formally measure an inclination of 63 ± 4 degrees assuming a thin H I disk and uncertainties of half the beam size along the major and minor axes.

As an instructive exercise, we assume a disk geometry and compute deprojected surface density profiles for AGC 229385 using Robertson-Lucy deconvolution (Lucy 1974, Warmels 1988, the GIPSY task RADIAL). This method, developed for use in low resolution imaging, works by collapsing the measured intensity along the minor axis, and produces a one-dimensional profile, which is then iteratively matched by a model one-dimensional profile produced by summing axisymmetric, uniform density co-planar rings along lines of sight. This method does not require knowledge of the inclination of the object, but still assumes a disk geometry. The summed one-dimensional surface density profile shows some asymmetry and two peaks with a slight depression in the center. These features are reflected by asymmetry in the resulting RADIAL model, and a strong suggestion of a hole in the center of the H I distribution, a feature that would be smeared out in 2D ellipse fitting analysis. If confirmed, this hole could

be indicative of the formation of cold atomic and molecular hydrogen in the center of the object, or of a non-disky, more complicated H I distribution, possibly caused by two recently merged components. However, higher resolution data are necessary to confirm the existence of a gap in the HI distribution.

The H I velocity field of AGC 229385 shown in Figure 4.3d is equally difficult to interpret. The narrow integrated H I line width and single peaked spectrum (shown in Figure 4.3f) is suggestive of slow rotation. If we assume a thermal velocity dispersion of 11.0 km/s, the 34 km/s integrated line width of AGC 229385 gives an observed rotation velocity of 16 km/s when subtracting thermal velocity and dividing by 2. This translates to a rough inclination-corrected rotation velocity of 18 km/s. Indeed, the moment 1 map shown in Figure 4.3d shows evidence of ordered rotation roughly along the major axis of the source, but the gradient is asymmetric; the irregular shape of the P-V diagram for AGC 229385 (Figure 4.3e) further diagnoses this asymmetry. The southern side of the source shows a clear slope of 12 – 15 km/s, but then any gradient appears to flatten out or even turn over as one approaches the north side of the galaxy. Further, the P-V diagram reveals that the velocity dispersion is of a similar order to the velocity gradient. It is possible that the major axis of rotation is offset from the surface density major axis: fitting a P-V diagram at 0° removes any turnover in the north side of the object, but does not give a significant gradient.

The FUV image of AGC 229385 from GALEX is shown in Figure 4.2. While this image is less striking than the optical images, this source is still detected in both the NUV and FUV images. The GALEX pipeline shreds this extended source into multiple point sources, so we measure its brightness in the same 32″ radius aperture and with the same masking that was used on the optical

images. The apparent magnitude and uncertainties in the NUV and FUV bands are 19.631 (0.069) mag and 19.155 (0.035) mag, respectively. After correcting for Galactic extinction, we use the assumed distance of 25 Mpc to determine star formation rates (SFRs) from the NUV and FUV luminosities following the relations of Murphy et al. (2011) and Hao et al. (2011), and report the results in Table 4.2. We do not include a correction for internal extinction.

Using the flow model distance of 25 Mpc, we derive absolute global parameters for AGC 229385, which are listed in Table 4.2. AGC 229385 has an optical luminosity comparable to typical dwarf galaxies (converted to M_B=−12.72 via Jester et al. 2005). Its $g' - r'$ color is very blue, and corresponds to a $B - V$ color of 0.13 (via similar conversion in Jester et al. 2005). Using this B magnitude instead of the SDSS g' magnitude, we find M_{HI}/L_B=38.2$M_\odot/L_\odot$. Using the self-consistent simple stellar population models discussed in McGaugh & Schombert (2014), this color implies a stellar mass-to-light ratio (in the V band) of $M_\star/L_V$=0.3$M_\odot/L_\odot$, or a total stellar mass of ∼1.5 × $10^6 M_\odot$, and a ratio f_{HI}=$M_{HI}/M_\star$=475.

4.3.2 AGC 229384

Figure 4.4a shows the deep 3-color WIYN pODI image of AGC 229384 with WSRT H I contours overlaid. No obvious optical counterpart is visible. The faint grid of horizontal and vertical stripes in the background is an artifact from the data reduction process. Figure 4.4b shows a zoomed-in view near the twin peaks of the H I contours (marked with black ×s). We used small 5″ × 5″ regions placed around this area to determine upper limits on the optical non-

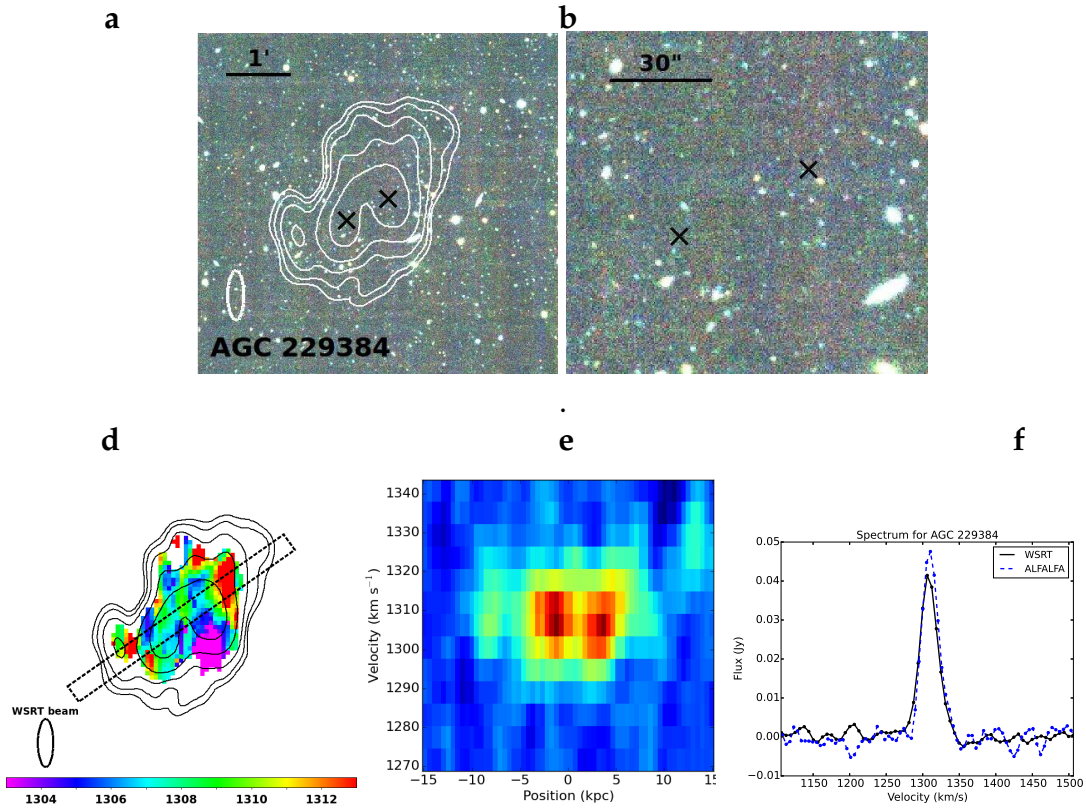

Figure 4.4: Our observations of AGC 229384, same panels as Figure 4.3. No optical counterpart is detected down to an upper limit of $\mu_{g'}$ ~27.8 mag/arcsec^2, so no surface brightness profiles are shown. The black "×"s in panels a and b mark the two peaks of the H I distribution. The H I velocity field of AGC 229384 in panel e shows no evidence of ordered rotation. As with AGC 229385, the WSRT and HI spectra in panel f are in good agreement with each other.

detection, using the same method as for AGC 229385, after masking all obvious foreground and background sources. The 3σ upper limits on this non-detection are given in Table 4.2, and are 27.9, 27.7, and 26.8 mag/arcsec^2 in g', r', and i', respectively. To estimate an upper limit on an integrated magnitude, we must assume an aperture size. Since the H I major axis of AGC 229384 is ~50% of the H I major axis of AGC 229385, the aperture is scaled by the same amount, to 15″. Using this aperture of radius 15″, we find 3σ upper limits on the integrated magnitude in g', r', and i' filters to be 20.7, 20.5, and 19.7 mag, respectively. These upper limits are used to generate upper limits on $M_{HI}/L_{g'}$, $M_\star$, and

$M_{HI}/M_\star$, all of which are shown in Table 4.2. In particular, these non-detections correspond to a stellar mass upper limit of $M_\star$<$3.4 \times 10^5 M_\odot$. When necessary, the observed colors of AGC 229385 were used to make filter conversions on the optical non-detections for AGC 229384. An archival GALEX image that covers AGC 229384 also shows no optical counterpart for this object (see Figure 4.2).

The H I contours of AGC 229384 in Figure 4.4a show an irregular distribution with two weak density peaks. The H I major axes at a surface density of $1 M_\odot$ pc^{-2} are $1.4' \times 1.2'$ or 10 kpc $\times$ 8 kpc. The H I velocity field shown in Figure 4.4d is patchy and irregular, and appears to be dominated by random motions. The position-velocity diagram in Figure 4.4e shows no evidence of ordered rotation. At its assumed distance of 25 Mpc, AGC 229384 has a total H I mass of M_{HI}=$2.0 \times 10^8 M_\odot$. Complete details are given in Tables 4.1 and 4.2.

4.3.3 AGC 229383

From the ALFALFA H I observations, AGC 229383 was extracted as a single, possibly extended weak source. Follow up observations with the single pixel L-Band Wide (LBW) receiver confirmed the existence and extended nature of the source, since the more sensitive LBW observations only recovered 64% of the original ALFALFA flux, as shown in Figure 4.5f. WSRT observations resolve the source into two low H I column density clumps, separated by 5.5 arcminutes ($\sim$ 40 kpc at D = 25 Mpc). The SE clump is only detected in a single beam at low signal-to-noise ratio, but is detected in both WSRT pointings which overlap its position. It is possible that these two clumps are independent sources. However, the two clumps together only recover 52% of the original ALFALFA

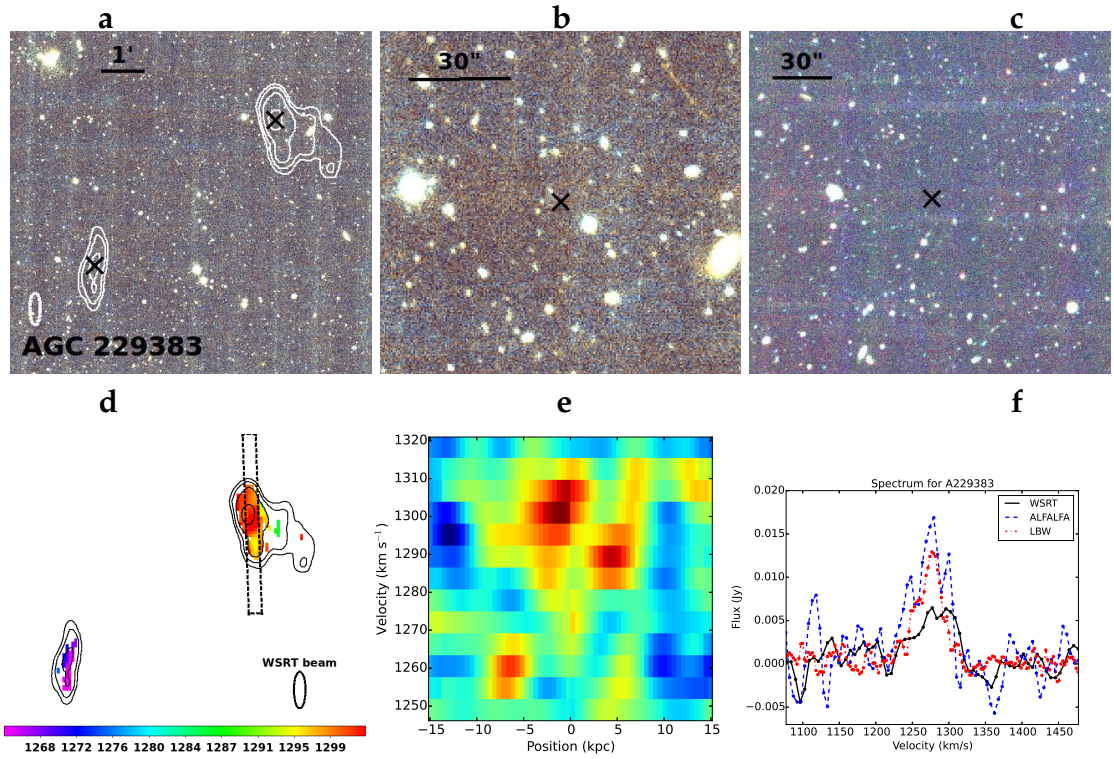

Figure 4.5: Our observations of AGC 229383, same as Figure 4.3. a) WIYN pODI optical image covering both peaks of the HI distribution, with contours from WSRT and black "×"s marking the H I peaks. b) A zoomed in view of the NW component, with a black "×" marking the peak of the H I distribution. No optical counterpart is detected. An asteroid trail is also visible in this image. c) A zoomed in view of the unresolved SE component, with its center marked. Again no optical counterpart is detected. d) The moment 1 map from WSRT with the same H I contours as above. The ellipse in the bottom right corner indicates the size and shape of the WSRT beam. The dashed rectangular region shows the slice along the major axis which is used to generate the P-V diagram to the right. e) Position-Velocity diagram from WSRT. No ordered rotation is visible in this splotchy and irregular velocity field. f) ALFALFA, WSRT, and LBW H I spectra of AGC 229383. As discussed in the text, LBW recovers 64% of the ALFALFA HI flux, and WSRT recovers only 52%. This likely means that there may be extended gas below the WSRT sensitivity which connects these sources, and we consider them to be peaks of a common source in this work.

flux, suggesting that there may be gas connecting the sources below the sensitivity of the synthesis observations. AGC 229383 may be two distinct sources, but because the missing flux and the clumpy H I distribution are ambiguous as to the true nature of the source, we choose to discuss it as a single source with two peaks in the remainder of this paper.

Figure 4.5a shows the color image made from the g' and r' observations of AGC 229383, which is located 19′ to the NW of AGC 229385. As with AGC 229384, no optical counterpart is visible. Figure 4.5b shows the zoomed-in region around the NW peak of the H I distribution. Again we masked obvious foreground and background sources and used regions around this area to measure the background statistics and determine upper limits on the optical non-detection using the same method as for AGC 229385. These 3σ upper limits are given in Table 4.2, and are 27.8 and 27.3 mag/arcsec^2, in g' and r', respectively. Similarly, we find upper limits on integrated magnitudes in a 15″ aperture of 20.7 and 20.2 mag in g' and r', respectively. We use these in the same way as AGC 229384 to generate upper limits for the derived quantities for AGC 229383, all of which are listed in Table 4.2. Figure 4.5c shows the zoomed-in region around the unresolved SE peak of AGC 229383, and reveals no optical counterpart as well.

The H I contours of AGC 229383 in Figure 4.5a show the two density peaks, of which the NW component appears resolved and the SE component unresolved. The H I never reaches a projected H I surface density of $1 M_{\odot}\mathrm{pc}^{-2}$ (corresponding to a column density of $12.5 \times 10^{19}\mathrm{cm}^{-2}$ at this distance), and has a maximum extent of only 48″ × 17″ at a column density of $5{\times}10^{19}\mathrm{cm}^{-2}$. The H I velocity field is patchy and irregular, and appears to be dominated by random motions, though our data are limited due to the fact that the two peaks are poorly resolved or unresolved. The limited data and patchy nature of the velocity field precluded meaningful fitting with XGAUFIT, so instead we show the moment 1 map in Figure 4.5d, and the messy position-velocity diagram in Figure 4.5e. At its assumed distance of 25 Mpc, AGC 229383 has a total H I mass of $1.2 \times 10^8 M_{\odot}$.

4.3.4 Isolation, Environment, and Distance Uncertainty

Isolation of the HI1232+20 system

Since many "dark" galaxy candidates turn out to be tidal features (e.g., VIRGOHI21 Duc & Bournaud (2008)) rather than isolated galaxies, we look for possible objects which may have recently tidally interacted with HI1232+20. To test this possibility, we searched all cataloged nearby sources in the Arecibo General Catalog (AGC), NED, and the SDSS spectroscopic survey and determined the timescale on which they could have interacted with this system, given their current velocities. If we generously assume that a flyby encounter may have had a relative velocity of ~500 km/s, we can calculate how long ago the nearby objects could have interacted. Naturally, the three sources in the HI1232+20 system all have short interaction time scales with each other (<300 Myr, based on these assumptions). The only source with an interaction time scale <1 Gyr is AGC 742390, which is ~30′ W of this system and has $cz = 1127$ km/s. AGC 742390 is an elongated star-forming galaxy with $M_g = -15$ mag, assuming it is at the same distance of 25 Mpc. At this distance, AGC 742390 has a projected separation from the HI1232+20 system of ~200 kpc, but its smaller recession velocity ($\Delta v \sim 200$ km/s) implies that it is likely more nearby than this system. Given the lack of obvious nearby galaxies in optical and H I surveys, and the lack of objects which could have recently tidally interacted with this system, it seems that HI1232+20 is a locally isolated system, and not a tidal feature of a larger parent object. Still, we cannot exclude the possibility that this system may have been produced as a result of tidal interactions or other gas stripping processes.

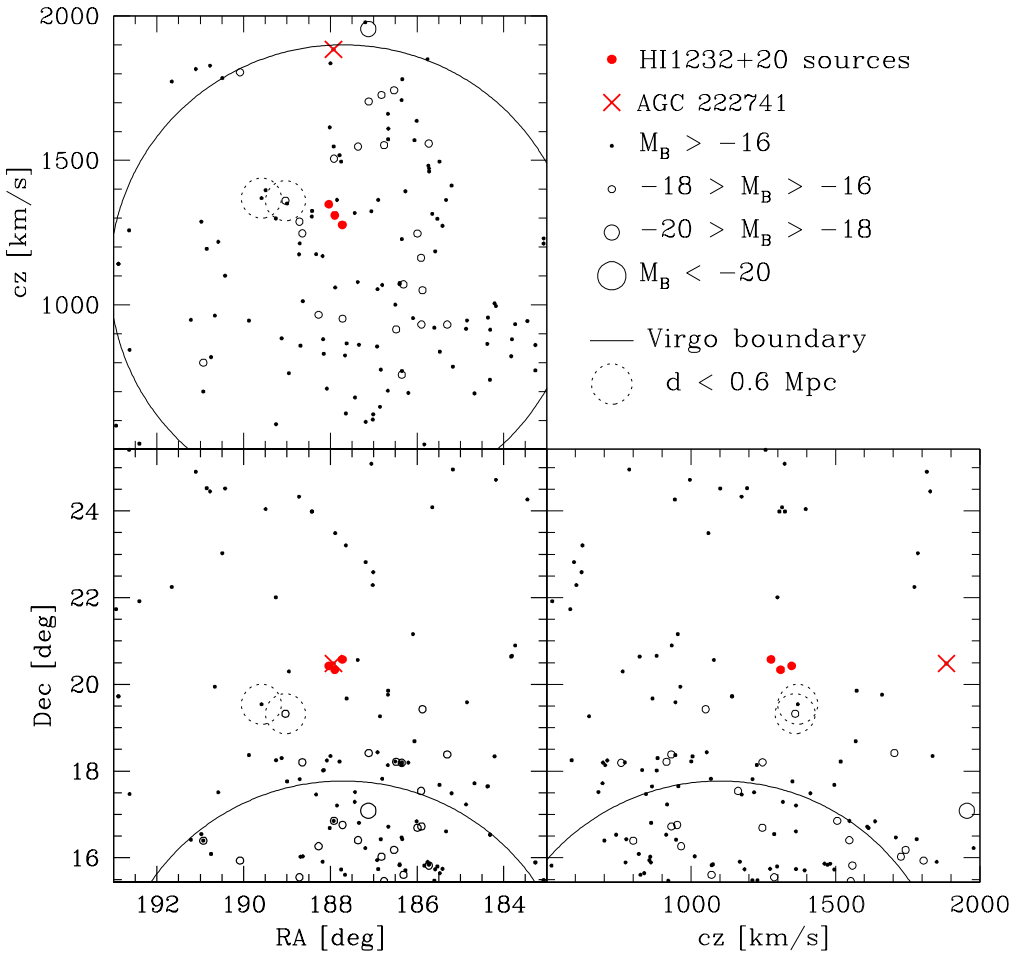

Figure 4.6: All panels show galaxies from the UZC, SDSS, and AGC. Larger circles represent more luminous galaxies, and smaller circles and dots represent less luminous galaxies. Note that we are plotting the three objects in the HI1232+20 system as red dots, as well as the background spiral galaxy (AGC 222741) at cz=1884 km/s as a red "×". The latter is nearby the objects in the HI1232+20 system in the RA-Dec plane, but is well-separated in the other two panels. The bottom left panel shows the galaxy distribution in the plane of the sky. The top left panel shows the galaxy distribution in the velocity-right ascension plane. The bottom right panel shows the galaxy distribution in the declination-velocity plane. The solid curved lines show the virial radius of the Virgo Cluster in each projection. Dotted circles enclose the galaxies nearest to this system.

Effects of distance uncertainty and the environment

Throughout this work we have adopted a flow-model distance (Masters, 2005) of D=25 Mpc to the HI1232+20 system. However, given its location on the outskirts of the Virgo Cluster, there is some uncertainty about its true distance. We

consider the possibility that the H I recession velocity may not give an accurate distance for this system, which could affect the derived absolute properties of the objects in the HI1232+20 system.

Large scale peculiar motions have been observed around the Virgo Cluster of galaxies, even beyond its virial radius, due to its significant gravitational influences. Recently, Karachentsev et al. (2014) used a large sample of 1801 galaxies (mostly from Karachentsev & Nasonova (2010) and with some new observations) in the vicinity of the Virgo Cluster which have independent distance measurements (e.g., Tully-Fisher, TRGB, Cepheid) as well as measured recession velocities. This kinematic sample of galaxies was used to map out the zero-velocity surface around the cluster, which encloses the region of space where galaxies are falling into the Virgo Cluster. Karachentsev et al. (2014) find that the zero-velocity surface radius is 7.2 ± 0.7 Mpc, which corresponds to a projected radius of 25° ± 2° at their assumed Virgo distance of D=17.0 Mpc. The HI1232+20 system is at a projected distance of only ~8° from the center of the Virgo Cluster (NGC 4486), and may be participating in the infall motion. Figure 1 in Karachentsev & Nasonova (2010) shows a graphical representation of the difficulty in determining distances from recession velocities in this region, and for this system's measured recession velocity of ~1300 km/s, there are three possible distances. If HI1232+20 were infalling from the near side, located at the center of the cluster, or infalling from the far side, it could have distances of ~12, ~17, or ~25 Mpc, respectively. Further complicating the nearby velocity field is the Coma I cloud just north of the HI1232+20 system. This complex of galaxies with peculiar velocities is centered around $(\alpha, \delta) = (12.5\text{h}, +30°)$ (Karachentsev et al., 2011). Still, we can make a crude but reliable estimate of the lower limit on the distance based on the fact that we do not resolve any individual stars

in the optical counterpart of AGC 229385. WIYN has been used to successfully resolve stellar populations in galaxies under similar observing conditions out to 2–4 Mpc (e.g., Leo P, Rhode et al. 2013; M81 group, Rhode, private communication). Furthermore, WIYN observations of SHIELD galaxies (Cannon et al., 2011) resolve upper main sequence and supergiant stars at distance of 8 Mpc.

Many of the most extreme properties of the objects in the HI1232+20 system are distance-independent quantities and would not be affected by a more nearby distance (e.g., M_{HI}/L_B, surface brightness measurements and limits, average H I surface density). However, if they were only ~12 Mpc distant instead of 25 Mpc, the absolute quantities (e.g., H I mass, stellar mass, total luminosity, physical area) would all scale down by a factor of four. For example, the H I mass of AGC 229385 would become $1.8 \times 10^8 M_\odot$, its stellar mass would be reduced to $3.8 \times 10^5\ M_\odot$, its absolute B magnitude would be reduced to M_B=−11.4 mag, and its optical diameter would be ~2 kpc.

Even with the difficulties of constraining the absolute distance to the HI1232+20 system, we are interested in the large scale environment around it, and how isolated it has been on longer time scales. The background spiral galaxy AGC 222741 (CGCG 129-006, labeled in Figure 4.1) appears on the sky between the three sources in HI1232+20, but has a recession velocity of $v_{\rm lsr}$=1884 km/s, which is substantially higher than the velocities of the three sources in the system (1277, 1309, and 1348 km/s), so is very unlikely to be related. Figure 4.6 shows the galaxies in the area around these H I sources. Galaxies shown on the plot come from the Updated Zwicky Catalog (UZC, Falco et al. 1999), from the spectroscopic sample of SDSS DR9 (Ahn et al., 2012), and from the Arecibo General Catalog (AGC). The UZC is an extragalactic redshift survey

of ~20,000 galaxies that is 96% complete to m_{Zw}<=15.5 mag and the SDSS DR9 spectroscopic survey includes spectra of ~1.5 million galaxies, and is 95% complete down to r'=17.7 mag. On Figure 4.6, a red "×" indicates the location of the background spiral galaxy (AGC 222741), which appears near our H I sources on the sky. Also shown on Figure 4.6 is the projected virial radius of the northern subcluster of the Virgo Cluster of galaxies (Binggeli et al., 1985). The curves enclose a region centered at the position of M87 with a radius of 5.4° and centered on a recession velocity of 1100 km/s and extending 800 km/s on either side (Ferrarese et al., 2012).

In order to demonstrate the complexity of the velocity field around HI1232+20, we calculate 3-space separations between this system and any nearby sources, using only their positions and observed velocities. The three sources within the HI1232+20 system are all within ~20′ and ~70 km/s of each other. While the global velocity field around these sources is complicated due to the influence of the nearby Virgo Cluster (Karachentsev & Nasonova, 2010; Karachentsev et al., 2014), we use this approach to crudely identify any possible galaxies which may be near enough to affect this system, and have similar positions and velocities. The object with the most similar velocity and position is NGC 4561 with a velocity of 1360 km/s and an angular separation of 1.4°, implying a physical separation of ~400 kpc assuming a simple Hubble flow. However, the Tully-Fisher distance to NGC 4561 is 12.3 Mpc (Tully & Fisher, 1987), so it is likely infalling to the Virgo Cluster from the near side. The object with the next-smallest 3-space distance is the starbursting galaxy IC 3605, which has a velocity of 1360 km/s and is located ~1.8° to the SE, with an implied physical separation (Hubble flow only) of ~500 kpc. No other distance measurements exist for IC 3605. The locations of NGC 4561 and IC 3605 are indicated on Fig-

ure 4.6 with large dotted circles. The close proximity of this system to the Virgo Cluster means that its distance is uncertain and that the global velocity field is rich and complex.

4.4 Discussion

The objects in the HI1232+20 system are not easily explained, and some of their properties seem contradictory and puzzling. For example, it is difficult to understand the star formation history of AGC 229385, which apparently has only produced a tiny population of stars in an otherwise massive H I cloud. The H I mass of AGC 229385 (log M_{HI} = 8.9) is larger than the nearby star-forming Large Magellanic Cloud (log M_{HI} = 8.7, Kim et al. 1998) and just smaller than the nearby spiral galaxy M33 (log M_{HI} = 9.1, Gratier et al. 2010), although its stellar populations and optical luminosity are vastly dissimilar. The H I kinematics of its H I cloud are also perplexing, as its rotation speed seems inadequate for its large mass and size. It is similarly difficult to explain why the other members of the HI1232+20 system have not formed any detectable stars, even with their substantial, although quite spread out, HI distributions. For comparison, both AGC 229383 and AGC 229384 have larger H I masses than the nearby dI galaxies IC 10 and NGC 6822 (log M_{HI} = 8.0, Nidever et al. 2013, de Blok & Walter 2000), but lack any optical counterparts in our observations.

In order to put these objects in context with other galaxies, we consider their locations in typical galaxy scaling relations. In this exercise, we are treating these objects as independent galaxies and not simply gas clouds that have been stripped or tidally disturbed. It is possible that objects like this may be part of a

large but mostly-unobserved class of galaxies (e.g., the sunken galaxies of Disney (1976)), but is more likely that the objects in this system are simply unique and uncommon galaxies. Since AGC 229385 has an optical counterpart we consider its location on optical and H I scaling relations, while for the other sources our optical upper limits can still help constrain some of the same scaling relations. After discussing these scaling relations, we will will consider some possible formation scenarios to explain this unusual system of objects.

4.4.1 M_{HI}/L Relationship

One of the most extreme properties of the objects in the HI1232+20 system is their exceptionally large H I mass-to-light ratio measurements (or lower limits). Galaxies are known to follow a typical relationship between between this H I mass-to-light ratio and the overall luminosity. The HI mass-to-light ratio is defined as M_{HI}/L, where L is the optical luminosity, often measured in a blue filter. This relationship is especially difficult to measure for faint low-mass galaxies, where a significant fraction of the optical luminosity may come from low surface brightness regions. Almost universally, whenever a galaxy with a reportedly large M_{HI}/L_B ratio is observed with deeper optical images, the ratio returns to more typical values near unity. Warren et al. (2004) used survey and catalog data to identify possible galaxies with a large M_{HI}/L_B ratio ($3<M_{HI}/L_B<27$), but their sample of 9 large M_{HI}/L_B galaxies were almost all found to have less extreme ratios ($M_{HI}/L_B<5$) after deeper observations. Similarly, (van Zee et al., 1997) used broadband optical imaging observations of six low surface brightness dwarf galaxies to show that their catalogued optical magnitudes had been severely underestimated by ~1.5 mag, so their previously reported M_{HI}/L_B ra-

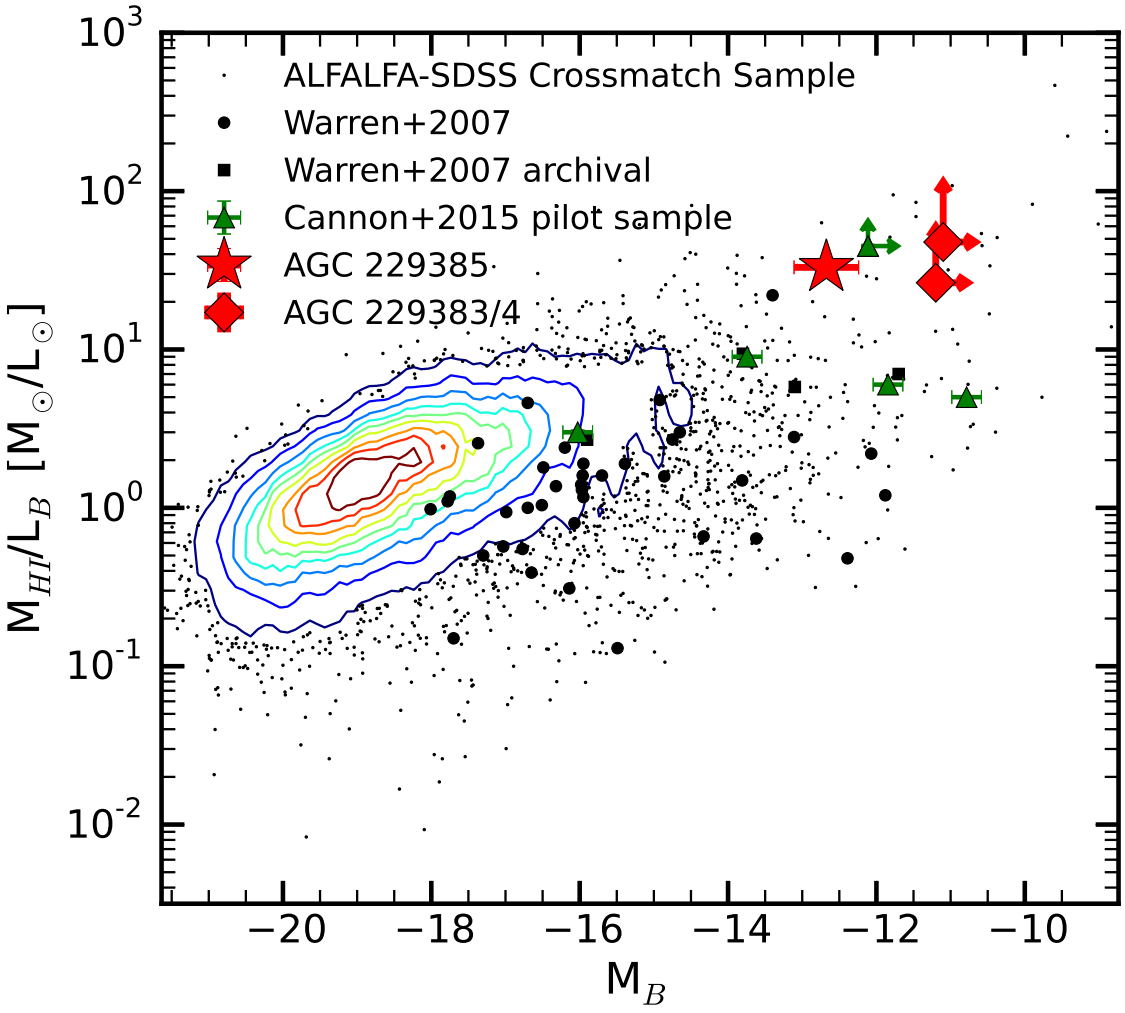

Figure 4.7: Relationship between the H I mass-to-light ratio (M_{HI}/L_B, in solar units) and absolute B magnitude. The small dots and contours indicate HI-detected galaxies from the ALFALFA α.40 catalog matched with SDSS DR7 photometry. The dark circles and squares come from the new and archival observations of Warren et al. (2007). The green points show the five (almost) dark galaxies from the pilot observations of Cannon et al. (2015). AGC 229385 is shown as a red star, and the upper limits for AGC 229383 and AGC 229384 are indicated with diamond points and arrows. The error bars on AGC 229385 also include a distance uncertainty of ±5 Mpc. The object from the Cannon et al. (2015) sample with a larger lower limit on M_{HI}/L_B than the measured value for AGC 229385 is AGC 208602 and is likely a tidal feature and not an isolated galaxy.

tios became 4 times smaller and less extreme. Among dwarf galaxies, typical measurements of M_{HI}/L_B are between 0.15 and 4.2, considering a variety of samples including Sm/Im galaxies (Roberts & Haynes 1994; Stil & Israel 2002) and field dIs (Lee et al., 2003). The relatively small dynamic range of ratios (a factor

of 30 between the lowest and highest ratio) highlights the importance of careful and accurate measurements of this ratio.

Figure 4.7 shows the relationship between the H I mass-to-light ratio (M_{HI}/L_B) and absolute B magnitude (M_B) for multiple samples of galaxies. The main dataset shown in Figure 4.7 comes from the matched ALFALFA α.40 and SDSS catalogs of Haynes et al. (2011), which is the parent sample from which the ALFALFA (Almost) Dark Galaxies are drawn. We note that the shallow SDSS photometry may underestimate the luminosity of the faint sources in this sample. The average exposure time in SDSS is only ~1 minute, and will not detect low surface brightness emission from these galaxies. Additionally, optical fluxes may be erroneously estimated due to issues with SDSS background subtraction and effects from nearby bright stars. Also shown on Figure 4.7 are galaxies from Warren et al. (2007), who observed 38 galaxies at optical and radio wavelengths, and also compiled an archival sample of previously observed galaxies. Some of these sources are observed at low Galactic latitude, which results in additional uncertainty in the necessary extinction corrections. The five (almost) dark galaxies from the pilot VLA observations of Cannon et al. (2015) are also shown on Figure 4.7 as green dots. The VLA observations allowed OCs to be identified for all but one of their sample, and the gas mass to light ratios for these sources are well-measured. We find that AGC 229385 has $M_{HI}/L_{g'}$=45.8$M_\odot/L_\odot$, or, converted to B via Jester et al. (2005), M_{HI}/L_B=38.2$M_\odot/L_\odot$, and its position is indicated on Figure 4.7. As AGC 229383 and AGC 229384 are not detected in our deep optical images, we can only determine lower limits on $M_{HI}/L_{g'}$, and find >31 and >57 $M_\odot/L_\odot$, respectively. These limits are also shown in Figure 4.7, where we have converted our upper limits in $M_{g'}$ to M_B assuming the same $g' - r'$ color as AGC 229385.

Warren et al. (2007) suggest that there is an upper envelope in Figure 4.7, which may represent the minimum amount of stars a galaxy will form, given a shallow potential well and an isolated environment. The sources in the HI1232+20 system are in an extreme region of Figure 4.7, near this upper envelope. While there are other galaxies from ALFALFA with more extreme values of M_{HI}/L_B shown on the plot, none have ratios that are as well-determined as the objects in this system. SDSS photometry for faint low surface brightness galaxies will likely underestimate their luminosity, which leads to an overestimate of the M_{HI}/L_B ratio. A recent study identified a low surface brightness galaxy near the Virgo Cluster with a very large H I mass-to-light ratio that they measure as $M_{HI}/L_V \gtrsim 20 M_\odot/L_\odot$ (Bellazzini et al., 2015). AGC 229385 has the largest accurately measured HI mass-to-light ratio in the literature, but still appears to lie along a continuation of the trend seen in more luminous galaxies. Warren et al. (2007) use a similar sample of galaxies with H I and optical data to fit the relationship between M_{HI}/L_B and M_B. They fit the upper envelope of the relationship with the following expression:

$$\log(M_{HI}/L_B)_{\max}=0.19(M_B + 20.4).$$

For AGC 229385 its M_B=−12.72 would predict a maximum M_{HI}/L_B=29. While AGC 229385 does follow the general trend of low stellar mass objects having higher gas mass-to-light ratios, we measure M_{HI}/L_B=38, which is even more extreme than the upper envelope of Warren et al. (2007).

4.4.2 Galaxy Scaling Relations with Stellar Mass

Studies of large samples of galaxies have found that stellar mass seems to be an important parameter that relates to star formation in the possible evolution of galaxies from the blue cloud to the red sequence (Brinchmann et al. 2004; Salim et al. 2007; Huang et al. 2012a). Using a sample of 9,417 ALFALFA-selected galaxies with counterparts in archival GALEX and SDSS images, Huang et al. (2012a) studied the scaling relations as a function of stellar mass and optical color (see their Figure 8). Figures 4.8a and 4.8c show the H I mass and f_{HI}=$M_{HI}/M_\star$ as a function of the stellar mass, which is determined from SED fits. A clear relationship with M_{HI} is found from $M_\star$=3.2×$10^7 M_\odot$ to 3.2×$10^{11} M_\odot$, with a change in slope at $M_\star \sim 10^9 M_\odot$. Analogously, f_{HI} follows the same general trend with a break at $\sim 10^9 M_\odot$. On both panels the location of AGC 229385 is indicated with a large star, and the upper limit measurements of AGC 229383 and AGC 229384 are indicated with arrows. These sources are deviant from the expected scaling relations at the low stellar mass end, and have too much H I for their stellar mass (detected or not).

Figures 4.8b and 4.8d show M_{HI} and f_{HI} as a function of $NUV - r$ color, which acts as an indicator of the amount of recent star formation (UV) compared to the amount of past star formation (r). Here only AGC 229385 can be plotted, since we have no optical or UV detections of the other two sources. AGC 229385 is at an extreme location in both of these parameter spaces, and lies significantly above an extrapolation of the low mass trend in the relationship between f_{HI} and $NUV - r$. The color cannot be much bluer than it already is, since after 5 Myr, a simple stellar population of half solar metallicity will have $NUV-r$=−0.2 (Bressan et al., 2012). AGC 229385 seems to be deviant in the sense

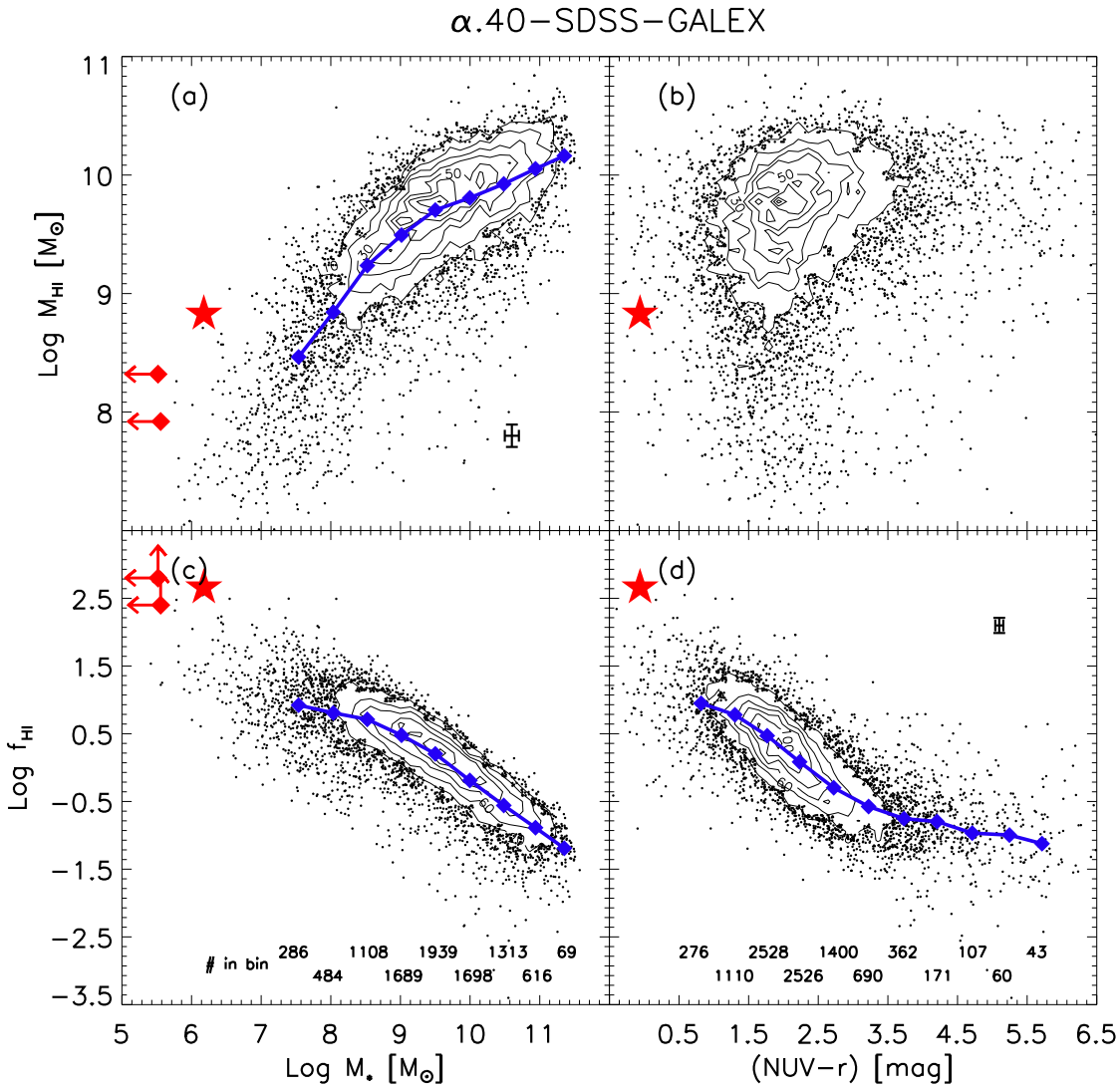

Figure 4.8: The scaling relations between H I and optical observations, using the α.40-SDSS-GALEX sample and analysis from Figure 8 of Huang et al. (2012a). In all panels, number densities of galaxies are calculated within grid cells set by the intervals of the minor ticks on the axes. Contours are drawn above densities of 20 galaxies per grid cell, and selected contours are labeled with their number densities. Blue diamonds and lines show the average y-values in each x-bin. Panel (a) shows the relationship between H I mass and stellar mass, with stellar masses from mass-to-light ratios from fits to SDSS photometry. Panel (b) shows the H I mass as a function of NUV-r color. Panel (c) shows the ratio of H I mass to stellar mass (f_{HI}=$M_{HI}/M_\star$) versus stellar mass. Panel (d) shows the relationship between f_{HI} to NUV-r color. Typical error bars of individual galaxies are shown in the corner of panels (a) and (d). The red star shows the location of AGC 229385 in each panel, while the red arrows indicate the upper limits of AGC 229384 and AGC 229383 where measured.

that it has too much H I for its $NUV - r$ color, consistent with the previously discussed panels. Finally, we note that Toribio et al. (2011) found a strong relationship between M_{HI} and the optical diameter measured at $\mu = 25$ mag/arcsec^2, such that galaxies with smaller values D_{25} typically had smaller H I masses as well. However, we cannot compare the properties of the HI1232+20 system with this relationship because the optical counterpart to AGC 229385 never reaches $\mu = 25$ mag/arcsec^2, and the other two sources have even fainter limits on their optical non-detections.

4.4.3 Galaxy Scaling Relations with H I mass

We now discuss the scaling relations which depend on the total HI mass of a galaxy. First, we consider the relationship between HI diameter (measured at a particular column density) and total H I mass. Broeils & Rhee (1997, hereafter BR97) observed this relationship in a sample of 108 spiral and irregular galaxies and found a strong correlation between $log\ M_{HI}$ and $log\ D_{HI}$ (the H I diameter at $1 M_\odot/\mathrm{pc}^2$), with a dispersion of only 0.13 dex, and a slope of 1.96 ± 0.04. Swaters et al. (2002) found the same correlation and slope when they used a sample of lower mass irregular galaxies. This relationship has been measured between H I masses of 6×10^7 and $3\times10^{10} M_\odot$ and between H I diameters of 0.8 and 160 kpc. A consistent relationship implies that there is a constant average HI surface density in all gas-rich galaxies, which BR97 estimates as $3.8 \pm 1.1\ M_\odot \mathrm{pc}^{-2}$.

While explanations for the underlying mechanisms for this correlation are complex (e.g., feedback, turbulence, etc.), it is simple to apply the relationship from BR97 to our sources. In the case of AGC 229385, our H I mass pre-

dicts an H I diameter of 16 kpc (measured at $1 M_{\odot}/\mathrm{pc}^2$). Our H I observations of AGC 229385 show an elongated source with dimensions 24×10 kpc, when measured at this H I column density. This is ~50% larger than predicted, and while projection effects could reduce this discrepancy somewhat, the H I kinematics do not suggest we are viewing a disk edge-on so any correction for projection effects will be small. AGC 229384 has an H I mass of $2.00 \times 10^8 M_{\odot}$ which predicts an H I diameter of 8.1 kpc. Our observations show an elongated H I source with dimensions 10×8 kpc, which is slightly larger than expected (although this source has two separate H I peaks at that column density). The H I distribution of AGC 229383 never reaches the column density that corresponds to $1 M_{\odot}/\mathrm{pc}^2$, and we are unable to apply this relationship to it. Both AGC 229385 and AGC 229384 have larger H I diameters than predicted by the H I diameter-H I mass scaling relation. This also implies that their average H I surface density is significantly less than the constant value found by BR97. Assuming a circular H I disk for AGC 229385 and AGC 229384, we find that their average H I surface densities are 1.6 and $2.4 M_{\odot}\mathrm{pc}^{-2}$, respectively, which are at the lower limit of the distribution found by BR97. Rosenberg & Schneider (2003) also compared M_{HI} and D_{HI} for a different sample, but their relationship gives similar results to BR97. These unusually low H I surface densities may be related to the lack of significant star formation in the objects in the HI1232+20 system.

4.4.4 Galaxy Scaling Relations with HI kinematics

We consider the H I kinematics of the sources in the HI1232+20 system, especially with regard to their apparently slow rotation. However, since the H I rotation curves of these sources are difficult to fit or interpret (see Figures 4.3e, 4.4e,

and 4.5e), we instead use the integrated width of the 21cm line itself to measure their rotation. The H I velocity widths (W_{50}, measured at 50% of the peak value) of the three sources in the HI1232+20 system are unusually small for their H I masses. We model the H I velocity width distribution for all ALFALFA galaxies as a function of their HI mass. Integrating over the model distribution at the H I mass of AGC 229385 (M_{HI}=6.7 $\times$ $10^8 M_\odot$) we find that only 2% of ALFALFA galaxies have velocity widths smaller than its measured value of W_{50}=34 km/s. Similarly for AGC 229384, we find only 3% of ALFALFA galaxies at its H I mass have similarly small values of W_{50}. We note that the much wider velocity width of AGC 229383 falls near the 50th percentile of objects of its H I mass, but that this may be due to the presence of multiple objects within the ALFALFA beam. Full details of the velocity width model will be published in a forthcoming paper (Jones et al. in prep.).

We can next use the Baryonic Tully Fisher relation (McGaugh, 2012) to compare the total baryonic masses with the rotation velocities for the members of the HI1232+20 system. Since these objects are gas-dominated, we use the relationship from McGaugh (2012) to calculate rotation velocities as v_f=W_{20}/2, where W_{20} is the H I velocity width at 20% of the maximum. While the H I rotation of these objects is difficult to measure accurately, their placement on the BTF relation is intended as a suggestive exercise to shed light on some of their unusual properties. If these objects are indeed galaxies, then their rotation seems too slow for their measured mass.

Figure 4.9 shows the locations of the objects in the HI1232+20 system compared to a large sample of galaxies (McGaugh 2012, McGaugh 2005). The baryonic mass is the sum of the stellar and total gas mass, and in gas-dominated

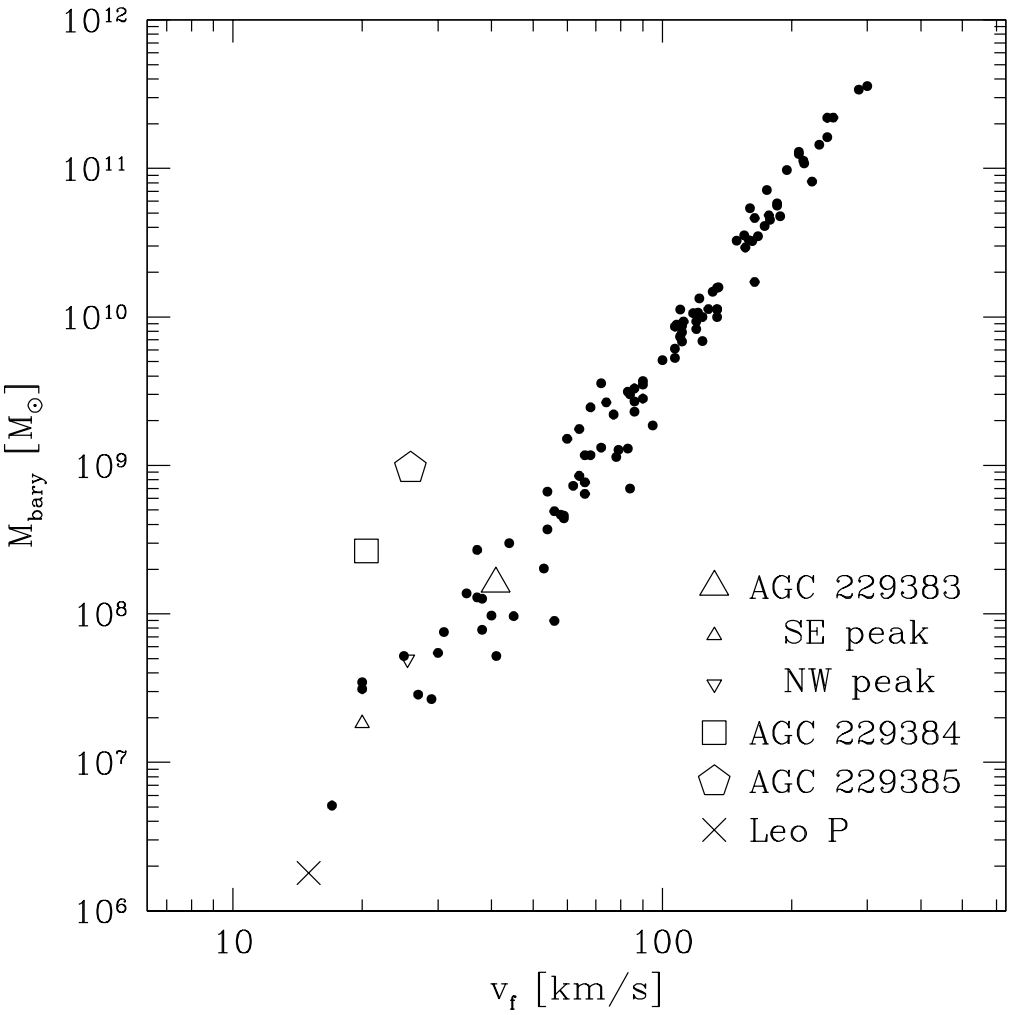

Figure 4.9: Baryonic Tully-Fisher relation. Black dots show galaxies measured by McGaugh (2012) and McGaugh (2005). Open polygons show the sources in the HI1232+20 system from this work. AGC 229385 (shown as an open pentagon) has the largest H I mass of this sample and is offset above the BTF relation. The next most massive, AGC 229384 (shown as an open square), is also offset above the relationship, while the least massive, AGC 229383 (shown as an open triangle), is consistent with the BTF relation. The two H I peaks of AGC 229383 are measured separately (shown as small triangles), and both lie along the BTF relation as well. The "×" shows the position of Leo P, a metal-poor gas-rich dwarf galaxy discovered by ALFALFA in the local volume just outside the Local Group (Giovanelli et al., 2013; Rhode et al., 2013; Bernstein-Cooper et al., 2014).

galaxies without substantial stellar populations, is determined as $M_{\rm bary}$=1.33 × M_{HI}, where the extra factor of 1.33 accounts for helium. The stellar mass of the optical counterpart of AGC 229385 contributes only a negligible ~0.2% com-

pared to its HI mass. The upper limits on the non-detections of stellar populations of the other two objects indicate that these would contribute similarly negligible amounts of baryonic mass. This estimate of baryonic mass does not include contributions from molecular or ionized gas. It is conceivable that there may be an envelope of low density ionized gas surrounding these galaxies, contributing more mass than is included in our determination of $M_{\rm bary}$.

Figure 4.9 shows that the two more massive objects in the HI1232+20 system both fall significantly above the standard BTF relationship, while the least massive (AGC 229383) is in agreement. However, since AGC 229383 has two strong H I peaks which are separated by $\sim$ 40 kpc, we also consider the kinematics of each clump separately, and plot them on Figure 4.9 as well. AGC 229383 is the lowest column density object of this system, and is, at best, difficult to interpret. Naive placement of the combined object or its peaks seems to agree reasonably well with the BTF, but the low signal-to-noise nature of the H I observations makes further analysis or interpretation difficult. We also caution that the WSRT observations do not recover the total H I flux of ALFALFA (see Section 4.3.3), so the H I masses of the two peaks do not sum to the total observed mass.

We note that inclination effects could slightly modify our determination of rotation velocities, but that the discrepancies from the BTF are larger than can be accounted for by changing the inclination angle of the objects. If the distance to the HI1232+20 system was significantly smaller, then they would be in better agreement with the BTF. In order for AGC 229385 to agree with the BTF it would need to be at a distance of ~4.4 Mpc, and AGC 229384 would need to be at a distance of ~5.4 Mpc. This smaller distance is unlikely given other constraints

(e.g., the lack of resolved stars in our optical observations, see Section 4.3.4).

We also consider the ratio of dynamical mass to H I mass ($M_{\rm dyn}/M_{\rm HI}$) as another independent constraint on the distance by assuming a typical value of $M_{\rm dyn}/M_{\rm HI}$=10. We measure an effective velocity ($v_{\rm eff}^2$=$v_{\rm rot}^2+3\sigma_v^2$) for AGC 229385 of $v_{\rm eff}$=21.2 km/s, so this relationship implies a distance of 4.3 Mpc. If we assume no dark matter (e.g., $M_{\rm dyn}/M_{\rm HI}$=1.3), we find a distance of 32.8 Mpc instead. The H I kinematics of AGC 229384 and AGC 229383 make it difficult to measure $v_{\rm rot}$, which is required to determine $v_{\rm eff}$.

4.4.5 Formation Scenarios

Given the variety of observational constraints we have for the sources in the HI1232+20 system, and the context from existing galaxy scaling relations, we now consider some of the possible evolutionary scenarios which could account for a system like this.

The blue color of the optical counterpart of AGC 229385 suggests that it may consist of a mostly young stellar population. If this object has only just begun forming stars, it may not have had enough time yet to convert a significant amount of its gas into stars, as reflected by the high gas mass-to-light ratio. However, the lack of Hα detection and the weak UV SFR (~0.004$M_\odot$/yr) seem to indicate that it is only slowly forming stars. At this rate it would take more than a Hubble time to generate enough mass in stars to return it to the normal relationship between H I and stellar mass (e.g., Figure 4.8a).

It is difficult to find a single convincing explanation for why one H I cloud

has an observable stellar population while its two nearby neighbors do not. Obviously, this creates a "fine-tuning" problem of sorts. Interactions between the members of this system may have triggered star formation in the most massive object. It is also possible that the system may have been perturbed by an external object. Our analysis in Section 4.3.4 showed that there was only one plausible perturber nearby, even given our generous assumptions about relative velocities and timescales for interactions.

Alternatively, Verde et al. (2002) has suggested that low-mass dark matter halos can contain neutral gas without ever forming stars, under certain conditions. However, the members of this system have substantial H I masses and are likely different from the low-mass dark matter halos of Verde et al. (2002). It may be that star formation has only occurred in the H I cloud which is dense enough at its center to exceed a gas density threshold (e.g., Kennicutt (1998)). Indeed, in studies of the outer disks of larger galaxies, star formation appears to cease below an H I surface density of $\sim 1 M_{\odot}/pc^2$ (Radburn-Smith et al., 2012; Hunter et al., 2013). The H I distributions of the sources in the HI1232+20 system are mostly below this surface density threshold, and only the peak of AGC 229385 substantially exceeds it.

The reasons behind the low gas surface density and over-extended H I distributions of these objects are not clear. In the case of AGC 229385 it is possible that feedback from the star formation (perhaps stronger in the past) has injected kinetic energy into the HI, and temporarily expanded it. Or, we may be seeing the results of a recent infall of cold gas into this system. However, these objects have significant amounts of HI, and it is difficult to justify an inflow scenario which could provide enough gas while maintaining a low gas density and in-

hibit star formation.

It is also possible that these objects may be the most massive knots in a system of smaller H I clouds which are in the midst of a tidal interaction or merger event. AGC 229385 and AGC 229384 may be the brightest H I peaks, and could be the products of recent mergers of smaller HI clumps. The extended nature of AGC 229383 and its two H I peaks are suggestive of an extended HI distribution with local peaks and clumps. However, the ALFALFA observations are very sensitive to faint H I emission, and given the good agreement between WSRT and ALFALFA H I fluxes for AGC 229385 and AGC 229384, it seems unlikely that there is a substantial amount of unseen extended gas in most of the system.

The HI1232+20 system does not seem to be a tidal feature or remnant of a larger object, based on the lack of a clear connection to any possible external perturbing object. However, tidal interactions between members of the system may be important to their individual star formation histories. The H I clouds in this system have extremely low star formation efficiencies and low gas densities. These low gas densities are especially difficult to reconcile with the significant H I masses of these sources. The H I mass of AGC 229385 is greater than that of the LMC, and AGC 229383 has more H I than some nearby star-forming dwarf irregular galaxies. Even if recent tidal interactions between the sources may have triggered a burst of star formation in AGC 229385, the overall properties of the HI1232+20 system are difficult to convincingly interpret and explain.

4.5 Summary

In this work we present the discovery of the HI1232+20 system of HI sources, drawn from the sample of (almost) dark extragalactic sources in ALFALFA. This system defies conventional explanations and our H I synthesis imaging and deep optical observations have revealed a set of objects with properties that are difficult to reconcile with typical scaling relations. The most massive of its members (AGC 229385, M_{HI}=7.2×10$^8 M_\odot$) has a weak stellar counterpart, detected in UV and ultra-deep optical imaging, with a peak surface brightness of $\mu_{g'}$=26.4 mag/arcsec^2. It has the most extreme well-measured gas mass-to-light ratio in the literature ($M_{HI}/L_B = 38$), and its absolute magnitude is only $M_{g'} = -12.9$ mag ($M_\star = 1.5\times10^6 M_\odot$), assuming a distance of 25 Mpc. We do not detect optical counterparts for the other two members, but place upper limits on their absolute magnitudes of $M_{g'} > -11.3$ mag ($M_\star < 3\times10^5 M_\odot$). The H I kinematics of the three objects in this system are inconsistent with typical galaxy scaling relations, with HI distributions that are too extended and too slowly rotating for their H I mass. This group appears on the sky just outside of the projected virial radius of the Virgo Cluster, but is otherwise isolated from any nearby galaxies.

The HI1232+20 system is difficult to explain completely, but may be an example of objects just above and just below a threshold for star formation. The most massive of the three sources is forming stars, but may have only recently started to do so. The other two sources have no observational signatures of star formation, so there may be some mechanism inhibiting this process. Sources like these are very rare in the ALFALFA survey, especially at such large HI masses. As observations of the HI1232+20 system continue we hope to learn more about

its history and role in galaxy formation and evolution.

CHAPTER 5

(ALMOST) DARK GALAXIES IN THE ALFALFA SURVEY: ISOLATED H I BEARING ULTRA DIFFUSE GALAXIES

5.1 Introduction

Recent advances in low optical surface brightness survey techniques (e.g., Abraham & van Dokkum, 2014) have unveiled substantial populations of very low surface brightness "ultra-diffuse" galaxies (UDGs), which have stellar masses of dwarfs ($\lesssim 10^8 M_\odot$), but sizes comparable to $L_\star$ galaxies (effective radii of several kpc; van Dokkum et al., 2015).

UDGs appear to be common in cluster environments (e.g., Koda et al., 2015; van der Burg et al., 2016), and have colors and morphologies consistent with extrapolation of early type galaxies on the red sequence (van Dokkum et al., 2015). But UDGs also appear to exist outside of clusters. Martínez-Delgado et al. (2016) report the discovery of a UDG in the Pisces-Perseus Filament, and Merritt et al. (2016) and Smith Castelli et al. (2016) report the discovery of UDGs in group environments. Román & Trujillo (2017a) statistically estimate the distribution of UDGs around Abell 168, and suggest that more than 50% of UDGs could exist outside of the cluster environment.

UDGs appear to have high dark matter fractions within their optical radii, but the distribution of their halo masses is still unclear. van Dokkum et al. (2015) suggest UDGs could be failed $L_\star$ galaxies, with star formation quenched early in their lifetime, and van Dokkum et al. (2016) use spectroscopy of globular

This chapter is an adapted version of the published article Leisman et al. (2017).

clusters to estimate the halo mass of the UDG Dragonfly 44 to be near that of the Milky Way ($\sim 10^{12} M_{\odot}$). However, Beasley et al. (2016) used similar techniques, and Peng & Lim (2016), Beasley & Trujillo (2016), and Amorisco et al. (2016) use globular cluster counts to suggest instead that UDGs are more likely to reside in dwarf halos similar to the Large Magellanic Cloud ($\lesssim 10^{11} M_{\odot}$). Zaritsky (2017) uses scaling relations to suggest that it is also possible that UDGs span a range of halo masses between these extremes.

Several hypotheses have been suggested to explain these enigmatic galaxies. Some mechanisms focus on environmental effects. Yozin & Bekki (2015) demonstrate that they can reproduce the properties of UDGs in simulations where UDGs are satellites of clusters, falling into the cluster early, around z~2, and Baushev (2016) and Burkert (2017) invoke 2-body tidal encounters in dense environments. Other explanations suggest that UDGs formed via internal mechanisms. Amorisco & Loeb (2016) suggest they likely represent sources in halos in the high end tail of the spin parameter distribution, and Di Cintio et al. (2017) reproduce the extended stellar distributions of UDGs in isolated dwarf halos using gas outflows.

These latter explanations predict that UDGs could potentially exist in isolated environments, contain large reservoirs of gas, and be actively forming stars. Di Cintio et al. (2017) explicitly predict non-negligible H I gas masses of $10^{7-9} M_{\odot}$, and that the gas plays an important role in creating large radii. But the H I contents of UDGs are uncertain; the best H I upper limits at the distances of most UDGs (~100 Mpc) are around $10^{9} M_{\odot}$ (Haynes et al., 2011; Martínez-Delgado et al., 2016).

Further, if there are isolated star forming UDGs, they may be difficult to rec-

ognize. UDGs are a subset of "classical" low surface brightness galaxies (e.g., Schombert et al., 1992), which are known to exist across a wide range of sizes (e.g. Zucker et al., 2006; Bothun et al., 1987) and environments (e.g. Impey et al., 1988; Impey et al., 1996), and range from star forming late type galaxies (McGaugh et al., 1995) to bulge dominated early types (Beijersbergen et al., 1999). While classical LSB galaxies are typically higher surface brightness or less extended than UDGs, Yagi et al. (2016) point out that a small number of these LSB sources fit the observationally defined selection criteria for UDGs, a few of which are late type and contain H I. However, they suggest that they must be rare in the field due to the small number of detected sources.

Yet, finding isolated low surface brightness ultra-diffuse sources optically in a systematic way is difficult due to the lack of easily attainable distance information, and often relies on color selection criteria. Still, these sources may be detectable at other wavelengths if they contain significant gas.

The largest volume blind H I survey to date, the Arecibo Legacy Fast ALFA (Arecibo L-band Feed Array) extragalactic H I survey (e.g., Giovanelli et al., 2005; Haynes et al., 2011) is well-positioned to locate low surface brightness sources missed by optical detection algorithms (Du et al., 2015). Here we explore isolated ultra-diffuse sources from the ALFALFA survey which match the optical selection criteria for previously reported UDGs, and present results on three ultra-diffuse ALFALFA sources that happened to be included in exploratory observations by the ALFALFA (Almost) Darks campaign (e.g. Cannon et al., 2015). This campaign has been exploring the 1% of sources not easily identified with optical counterparts in the Sloan Digital Sky Survey (SDSS) or Digitized Sky Survey 2 (DSS2). We note that these "(almost) dark" observa-

tions have already uncovered at least one ultra-diffuse source with a similarly large radius for its stellar mass. Janowiecki et al. (2015) report the detection of AGC 229385, which has a peak g-band surface brightness of 26.5 mag asec^{-2} and a half light radius of ~2.4 kpc (assuming a distance of 25 Mpc). This source appears even more diffuse than most other reported UDGs, though it also has a significant distance uncertainty.

The paper is outlined as follows: we describe the selection of H I-bearing UDGs from the overall ALFALFA population in section 5.2 and our data in section 5.3. We then present optical and H I results in section 5.4. We discuss the star formation and dark matter halos of these sources in section 5.5 and conclude in section 5.6. For all calculations, the assumed cosmology is $H_0 = 70$ kms^{-1}Mpc^{-1}, $\Omega_m = 0.3$, and $\Omega_\Lambda = 0.7$.

5.2 Sample Selection

There are 24,159 high signal-to-noise, clearly extragalactic sources in the ALFALFA 70% catalog, 22,940 of which fall within the SDSS footprint and are at least 10′ away from stars in the Yale Bright Star Catalog. We use this sample to search for H I-bearing, isolated, ultra-diffuse galaxies as described below.

5.2.1 Distance and Isolation Selection Criteria

Due to Arecibo's comparatively large beam size (3.5′), cross identification with optical surveys becomes more difficult at larger distances. We thus restrict our search for UDGs to sources within 120 Mpc, where the ALFALFA beam corre-

sponds to ~120 kpc, or about 3× the diameter of the detected sources discussed below. This distance cut is also important to maximize physical resolution for future follow up observations. We also set a minimum distance limit of 25 Mpc, since redshift-dependent distance estimates for sources closer than 25 Mpc are subject to significant uncertainty.

Most optically dark or (almost) dark H I features turn out to be tidal in origin. To eliminate potential confusion between satellites and central halos, we restrict our sample to isolated sources by requiring that the nearest neighbor within 500 km s^{-1} in the Arecibo General Catalog[i] has a projected separation of at least 350 kpc. This eliminates potential confusion with low surface brightness tidal dwarf galaxies (e.g., Lee-Waddell et al., 2016), and extended tidal debris (e.g., Leisman et al., 2016). These distance and isolation criteria reduce our potential sample to 5186 sources.

5.2.2 Optical Selection Criteria

Sources that fit the criteria for ultra-diffuse galaxies are barely detected at the depth of the SDSS data, and thus tend to have poor or missing measurements in the SDSS catalog. However, automated measurements from the SDSS catalog tend to be reasonably reliable for moderate to high surface brightness galaxies. Thus, we use a two step selection process to find ultra-diffuse sources.

First, we eliminate moderate or high surface brightness sources from our sample with matching SDSS DR12 catalog measurements in the most sensi-

[i]The Arecibo General Catalog is a private database maintained over the years by MPH and RG; within the ALFALFA volume it contains all bright galaxies and galaxies of known redshift as available in NED with cz < 18000 km s^{-1} (including all measurements from SDSS and ALFALFA), and additional unpublished H I results as they are acquired.

tive filters (g, r, and i bands). Specifically, we eliminate sources that have an average surface brightness within the measured exponential effective radius <23.8 mag arcsec^{-2} and an average Petrosian surface brightness within the 90% Petrosian radius <25.0 mag arcsec^{-2} in all 3 bands. This cut leaves 645 candidate sources that do not meet all 6 criteria. We visually inspect these sources to remove clear high surface brightness sources with bad catalog measurements, and sources with missing or bad SDSS data (due to, e.g., bright stars), leaving ~200 low surface brightness candidates.

Second, we perform our own photometry on SDSS images of the remaining sources, correcting for galactic extinction and the effects of the PSF, but not for cosmological dimming (see section 5.3.2). We use these measurements to select sources with similar absolute magnitude, surface brightnesses, and radii to previously reported UDGs. The definition of "ultra-diffuse" varies significantly in the literature. van Dokkum et al. (2015) originally define their sample as having central, g-band surface brightness $\mu_{g,0} \gtrsim$24 mags arcsec^{-2}, and 1.5< $r_{\rm eff}$ <4.6 kpc. However, other authors have explored a wider range of parameter space (see Yagi et al., 2016 for a useful summary). For example, van der Burg et al. (2016) use the average r-band surface brightness enclosed within the effective radius, $24.0 \leq \langle \mu(r, r_{\rm eff}) \rangle \leq 26.5$ mag arcsec^{-2} (note: $\langle \mu(r, r_{\rm eff}) \rangle$ is 1.12 mag arcsec^{-2} brighter than $\mu_{r,0}$ for an exponential profile, though for the average UDG g-r color of ~0.5, this approximately corresponds to $\mu_{g,0} \gtrsim$23.4 mag arcsec^{-2}). Some authors have also suggested restrictions in absolute magnitude, luminosity, or stellar mass (e.g., Mihos et al., 2015), explicitly limiting UDGs to dwarf mass stellar populations. Differences in color and profile shape further complicate the matter, since sources detected in H I are usually star forming, with bluer colors and clumpier morphologies than previously reported UDGs. Thus, we choose to

define a more restrictive and less restrictive sample, but note that our choice of what constitutes "ultra-diffuse" is somewhat arbitrary.

Specifically, we select a restrictive sample of 30 H I-bearing ultra-diffuse sources (HUDS-R), with half light radii $r_{g,\mathrm{eff}}$ >1.5 kpc, $\mu_{g,0} > 24$ mag arcsec^{-2}, and $M_g > -16.8$ mag, and a broader sample (HUDS-B) of 115 sources with $r_{r,\mathrm{eff}} > 1.5$ kpc, $\langle \mu(r, r_{\mathrm{eff}}) \rangle > 24$ mag arcsec^{-2}, and $M_r > -17.6$ (corresponding to the surface brightness and radius limits from van Dokkum et al., 2015 and van der Burg et al., 2016 respectively; since these papers do not give explicit absolute magnitude limits, we chose the restrictive and broad samples to include absolute magnitudes up to that of the Small Magellanic Cloud (SMC; see McConnachie, 2012) and 2× the SMC respectively, which are reasonable matches to other limits from the literature - see, e.g., Yagi et al., 2016). We note that while most authors fit Sersic profiles with *n* free, due to the low S/N of SDSS at these surface brightnesses, we have forced our fits to have exponential (n=1) profiles, in keeping with the average value found for UDGs and typical H I-rich galaxies.[i] We also define HUDS-BG to be the 30 HUDS-B sources that have GALEX UV observations and fall in the 40% ALFALFA survey analyzed by Huang et al. (2012a). We discuss this sample further in section 5.3.3.

Figure 5.1 illustrates the optical similarity of these samples to other reported UDGs, and their extreme nature relative to other dwarfs and isolated sources from the ALFALFA survey. The HUDS-R and HUDS-B samples (shown with light yellow and darker orange triangles respectively), occupy a similar portion of the plot to previously reported UDGs from van Dokkum et al. (2015) and Román & Trujillo (2017a) (dark purple squares). Other ALFALFA sources

[i]Note: some authors (e.g., Román & Trujillo, 2017a) have suggested that a sersic index <1 is more appropriate for UDGs - we find that fixing n to, e.g., n=0.7 does not improve our fits, so we elect to use n=1.0.

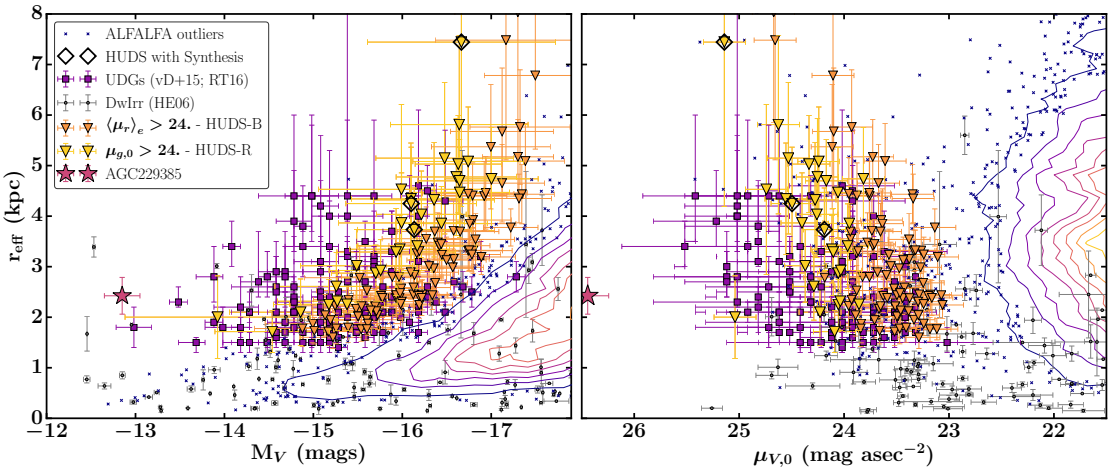

Figure 5.1: Optical properties of H I-bearing ultra-diffuse ALFALFA sources (HUDS) in comparison with other "ultra-diffuse" galaxies, showing that they fall in a similar part of parameter space to other UDGs. HUDS conforming to the stricter definition of "ultra-diffuse" (HUDS-R) are shown as lighter yellow triangles; those satisfying the broader criteria (HUDS-B) are shown with darker orange triangles. HUDS with existing synthesis observations are marked with black diamonds. Comparison samples of dwarf irregulars are small grey points (Hunter & Elmegreen, 2006), and UDGs are purple squares (van Dokkum et al., 2015; Román & Trujillo, 2017a). Other ALFALFA sources are shown by small dark blue points, and contours increasing in 10% intervals.

matching the distance and isolation criteria applied to the HUDS are shown with contours and small dark blue crosses. Dwarf irregulars from Hunter & Elmegreen (2006) are shown as small grey points, emphasizing the large extent of these sources relative to typical dwarfs. The HUDS for which we have existing synthesis observations (section 5.3) are marked with black diamonds. We note that all sources in the figure not observed in V-band have been transformed to V-band using the Lupton filter transformations from the SDSS website[i].

We emphasize that the sources selected here differ in important ways from, e.g., the population detected in Coma by van Dokkum et al. (2015). Most importantly, the isolation criteria restrict our sample to central halos. Thus, while some UDGs may be satellite galaxies or galaxies formed via tidal interactions,

[i] http://www.sdss.org/dr12/algorithms/sdssUBVRITransform/

this paper focuses on UDGs that are sufficiently isolated to be incompatible with these hypotheses. Further, as discussed in section 5.4, these HUDS tend to differ in both color and morphology from other reported UDGs. Thus, the HUDS discussed here are a specific subset of a growing population of extreme low surface brightness, "ultra diffuse" sources.

5.2.3 Sufficiency and Limitations of SDSS for Source Selection

Figure 5.1 also illustrates the limitations of using SDSS for optical measurements. The HUDS tend to fall toward the brighter side of the UDG distribution, which may be surprising given that the sources were identified by their H I content. Some of this bias is due to differences in the colors of the samples (discussed in section 5.4.1), since their bluer relative colors increase their V-band magnitude relative to the quiescent cluster UDGs. Much of it also may be due to the fact that HUDS are near the surface brightness limit of SDSS (which is somewhat variable, but, e.g., Trujillo & Fliri (2016) estimate $\langle \mu_r \rangle \geq$~26.5 mag arcsec^{-2} in a 10″ × 10″ region). Any sources with extended emission below the SDSS detection threshold but with central surface brightness just above it are likely to have their radii underestimated, and thus would be eliminated by the radius requirement. Indeed, several UDG candidates are sources without easily identified counterparts observed as part of the ALFALFA (almost) darks campaign.

However, the prior positional information from ALFALFA makes identification of UDGs in SDSS possible; sources not clearly visible in the SDSS finding chart images are in fact detected at reasonable significance in downloaded (and sometimes smoothed) images. The top panels of Figure 5.2 show SDSS imaging

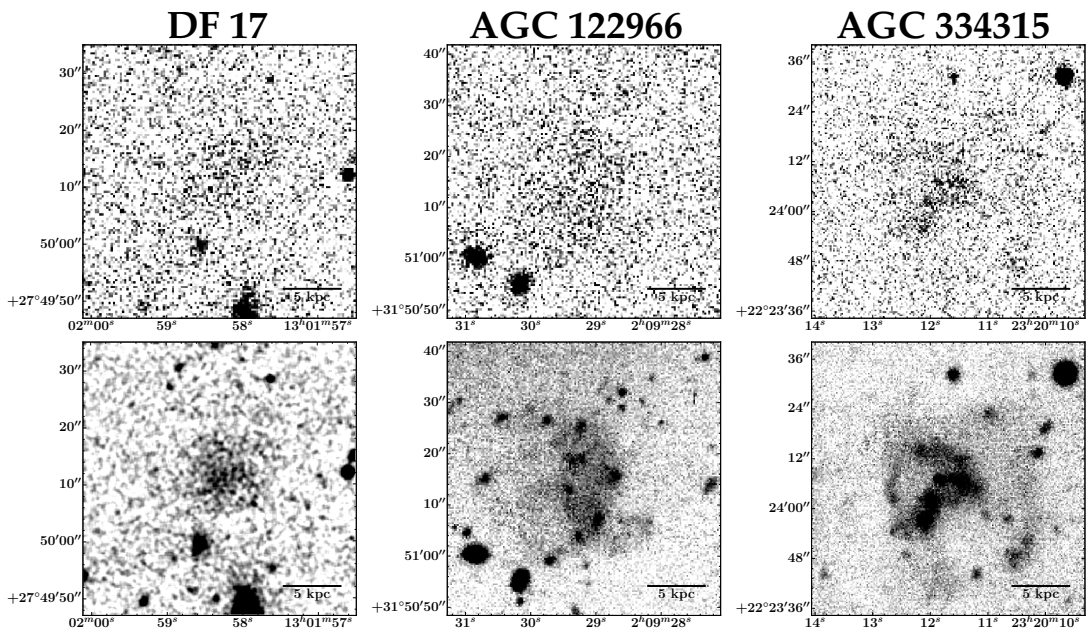

Figure 5.2: Comparison of SDSS and deeper imaging for a UDG and two HUDS; these sources are only barely detected in SDSS, but are located and confirmed by the position prior from ALFALFA. Left: SDSS (top) and CFHT (bottom) imaging of the Coma cluster UDG DF17. The UDG is visible in SDSS, and remains smooth in deeper imaging. Center and Right: SDSS (top) and WIYN pODI (bottom) imaging of two HUDS, AGC 122966 and 334315. The HUDS have a similar surface brightness to the Coma UDG, but have significantly more complicated morphologies in deeper optical imaging. RA and Dec are in J2000 coordinates.

of the UDG DF17 from van Dokkum et al. (2015), and of two HUDS from ALFALFA, shown at high contrast to emphasize low surface brightness details. The bottom panels show deep CFHT imaging of DF17, and deep pODI imaging with the WIYN 3.5m telescope of the two ALFALFA HUDS (see section 5.3.2). Of the 47 sources reported in van Dokkum et al. (2015), 46 are detected in downloaded SDSS imaging.

Further, though the estimated parameters from SDSS data have large uncertainties, they appear sufficient for our purposes. Applying our fitting procedure to SDSS data of the 46 detected sources from van Dokkum et al. (2015) produces values consistent with their measurements within estimated errors (the rms offset in central surface brightness (effective radius) is 0.4 mag (1.5 kpc), which is

less than the quadrature combined average error of 0.7 mag (2.2 kpc)). Further, the SDSS results are consistent with the results of deeper imaging in the two available cases (see section 5.3.2).

We emphasize that while the SDSS data demonstrate that these sources are very low surface brightness and very extended, they are too low signal-to-noise for detailed structural analysis, and that individual measurements are highly uncertain. Thus, this sample should only be thought of in a statistical sense. Indeed, a shift of 1σ would move an additional 30 sources into or out of the HUDS-B sample.

5.3 Observations and Data

All sources discussed here have available SDSS and ALFALFA data. However, three sources which meet the above criteria, AGC 122966, 334315, and 219533, were included in the ALFALFA (Almost) Darks campaign (e.g., Cannon et al., 2015), and thus have deep optical and H I synthesis imaging. Here we discuss the details of these observations.

5.3.1 HI Data

ALFALFA Data

The ALFALFA observations, data reduction, and catalog products are detailed elsewhere (e.g. Giovanelli et al., 2005; Saintonge, 2007; Haynes et al., 2011). Columns 1-8 of Table 5.1 give the H I data from the ALFALFA 70% catalog for

Table 5.1: Properties of HUDS

AGC ID	OC RA J2000	OC Dec J2000	cz km s^{-1}	W_{50} km s^{-1}	$\int S\,dV$ Jy-km s^{-1}	Dist[a] Mpc	log(M_{HI}) log $M_\odot$	$\mu_{g,0}$ mags/$''^2$	r_e kpc	M_g mag	g-r mag	Sample[b]
(1)	(2)	(3)	(4)	(5)	(6)	(7)	(8)	(9)	(10)	(11)	(12)	(13)
322019	344.6121	1.8497	4819	33±14	0.54±0.07	72	8.81±0.08	24.62±0.18	3.9±1.0	-15.8±0.7	0.36±0.25	R
103796	5.1650	6.9658	5647	31±7	0.48±0.04	80	8.86±0.06	24.23±0.14	3.9±0.7	-16.2±0.5	0.47±0.21	R
113790	18.2587	27.6369	4952	31±10	0.33±0.03	69	8.57±0.07	24.31±0.14	2.9±0.6	-15.4±0.5	0.42±0.19	R
114905	21.3271	7.3603	5435	27±3	0.96±0.04	76	9.11±0.06	24.85±0.19	5.1±1.5	-16.2±0.8	0.53±0.25	R
114943	26.7775	7.3311	8416	32±7	0.40±0.04	116	9.10±0.06	24.48±0.18	4.8±1.2	-16.4±0.7	0.36±0.28	R
113949	27.4108	30.6808	7380	44±7	0.44±0.05	102	9.03±0.07	24.29±0.18	3.4±0.8	-15.8±0.7	0.53±0.28	R
122966	32.3708	31.8528	6518	35±6	0.53±0.04	90	9.00±0.06	25.37±0.23	7.4±3.3	-16.4±1.1	0.38±0.41	R

Table 5.1 is published in its entirety in the machine-readable format. A portion is shown here for guidance regarding its form and content. H I and optical table parameters come from ALFALFA and SDSS, and are described in sections 5.3.1 and 5.3.2 of the text respectively. [a]: Distances from the ALFALFA flow model (see Haynes et al., 2011); distance depended quantities include an error of 5 Mpc due to peculiar velocities [b]: R = HUGS-R, B= HUGS-B

sources in the HUDS-R and HUDS-B samples. In brief, ID numbers (column 1) are taken from the Arecibo General Catalog (AGC), and the J2000 coordinates (columns 2 and 3) are those of the identified very low surface brightness optical source. Recessional velocities (column 4) are measured at the center of the H I line at the 50% flux level. W_{50} (column 5) is the width of the H I line measured at the 50% flux level, corrected for channel broadening. H I line fluxes (column 6) are calculated from fits to the spatially integrated line spectrum, Distances (column 7) are calculated using the ALFALFA flow model, which is simply Hubble Flow at $cz > 6000$ km s^{-1}; for sources in this velocity range (~2000-8000 km s^{-1}) distance uncertainties due to proper motions are $\lesssim$15%. H I masses (column 8) are calculated from the given integrated fluxes and distances assuming that the gas is optically thin.

Of particular relevance to this paper, optical identification is done by eye, matching sources in SDSS or DSS2 images with the ALFALFA position. We emphasize this visual identification, because extended nearby sources, including low surface brightness sources, are often shredded into multiple sources, and classified as more distant objects in automated catalogs. Further, we are able to identify a likely counterpart even in cases where the catalog does not include an entry due to a failure in the fit or proximity to a star. Without a corresponding optical redshift, identification necessarily relies on a small spatial offset between the optical source and the ALFALFA position. Though rare sources have been identified at large offsets from the ALFALFA centroid (Cannon et al., 2015), the average ALFALFA H I centroid accuracy is $\lesssim$20″, and confirmation observations have found the identifications to be quite reliable in almost all cases with an identified optical counterpart.

Synthesis Data

We observed AGC122966 and AGC 334315 with 2×12h pointings with WSRT as part of exploratory observations of (almost) dark sources in the ALFALFA survey (program R13B/001; PI Adams). The observations were centered on the central H I velocity measured in ALFALFA, with a 10 MHz bandpass with 1024 channels and 2 polarizations, leaving ample line-free channels for continuum subtraction, but still sufficient velocity resolution of 4.1 km s^{-1} after Hanning smoothing.

We observed AGC 219533 under a separate program (14B-243; P.I. Leisman) with the Karl G. Jansky Very Large Array (VLA) in 2014. We observed the source for two 3 hour observing blocks in C-configuration, using the WIDAR correlator in dual polarization mode with a single sub-band 8 MHz wide with 1024 channels, giving a native channel width of 1.7 km s^{-1}.

We reduced the WSRT data following the same process described in Janowiecki et al. (2015) and Leisman et al. (2016), using the automated pipeline of MIRIAD (Sault et al., 1995) data software wrapped with a Python script (see Serra et al., 2012; Wang et al., 2013). The pipeline automatically flags the data for RFI and iteratively deconvolves the data with the CLEAN algorithm after primary bandpass calibration, in order to apply a self-calibration. The calibration solution and continuum subtraction are applied in the visibility domain before inverting the data. The resulting data cubes are iteratively cleaned down to their rms noise, using CLEAN masks determined by clipping after filtering with Gaussian kernels. This process produces cubes with three different robustness weightings, r=0.0, r=0.4, and r=6.0, and bins the data to a velocity resolution of 6.0 km s^{-1} after Hanning smoothing.

We reduced the VLA data using standard procedures in the CASA package (Common Astronomy Software Applications; McMullin et al., 2007), including flagging of the visibilities, calibration, and continuum subtraction. We imaged the calibrated uv data following standard procedures, producing data cubes using the CLEAN task in CASA, with a Briggs robust weighting of 0.5. Since we expected the source to be extended, we used the multiscale clean option which improves localization of extended flux (Cornwell, 2008). It models the source as a collection of point sources and Gaussians of the beam width and several times the beam width.

For each source we created H I total intensity maps by creating a 3σ mask on images smoothed to 2x the beam size, applying the mask to the unsmoothed cubes, and then summing along the velocity axis. We convert these maps to H I column densities assuming optically thin H I gas that fills the beam, and also produce H I moment one maps (representing velocity fields) from the masked cubes. The resulting H I images and velocity maps are shown in Figure 5.3.

5.3.2 Optical Data

Archival SDSS Data

We obtained calibrated, background subtracted SDSS optical images in the g, r, and i bands for the full sample from the SDSS mosaic server described in Blanton et al. (2011). They estimate that the uncertainty in the background contributes a systematic uncertainty of up to ~10%.

Since the inclination is poorly constrained for the low surface brightness

sources in question, we measure the average flux in concentric circular annuli to approximate the surface brightness profile of the sources, using Python code we developed based on Astropy (Astropy Collaboration et al., 2013), and its affiliated package Photutils. We note that we chose the galaxy center to be the center of the extended optical flux, which, for sources with clumpy morphologies and significant evidence of star formation, may not be the location of the peak flux. We then fitted exponential functions to the surface brightness profiles, including a term to estimate a constant offset due to the background.

We correct our measured profiles for galactic extinction, but do not correct for cosmological surface brightness dimming for consistency with other local universe studies, and since the dimming corrections are small at the distances of our sample. We model the effect of the PSF on our fitted values by simulating model 1D profiles convolved with a 1D approximation of the SDSS PSF, and then applied our fitting method to both the true and convolved profiles to calculate analytic approximations of its effect. We then correct our measured parameters accordingly. We note that the sources in this sample are very extended relative to the SDSS PSF, so these corrections tend to be small.

We report the results of these fits in columns 9-12 of Table 5.1. Specifically, column 9 gives the measured central surface brightness from the exponential fit to the g-band data, and errors that are the quadrature sum of uncertainties from the fit and an assumed 10% uncertainty in the absolute background calibration. They do not account for additional systematic errors introduced from uncertainty in the inclination or galaxy centroid. Column 10 gives the effective radius, which is 1.68× the disk scale length from the exponential fit, and contains half the light from the galaxy. Column 11 gives the estimated absolute

magnitude derived from integration of the exponential fit and the assumed distance. We note that this total magnitude has not been truncated and should be used with caution: it is significantly brighter than measurements derived from aperture magnitudes, especially given the large estimated disk scale length for these extended sources. Column 12 gives the g-r color derived from the offset between the exponential fits, which is a better measurement than from using the absolute magnitude of these sources.

WIYN pODI Data

We observed AGC 122966 and AGC 334315 in October 2013 with the WIYN[i] 3.5-m telescope at Kitt Peak National Observatory[ii] using the partially populated One Degree Imager (pODI). At that time, pODI had a field of view of $24' \times 24'$, and we used a dithering sequence to eliminate chip gaps. We obtained nine 300s exposures in SDSS *g* and *r* filters (Gunn et al., 1998, Doi et al., 2010) for both targets. Due to unfavorable weather conditions, we did not observe AGC 219533. While faint, it is significantly detected in SDSS images and we use those in this analysis.

We reduced our observations using the QuickReduce (QR, Kotulla, 2014) data reduction pipeline via the ODI Pipeline, Portal, and Archive (ODI-PPA; Gopu et al., 2014, Young et al., 2014) at Indiana University. The QR pipeline removes instrumental signatures including bias, dark, flat, pupil ghost, nonlinearity, cosmic rays, and fringes. We also applied an iterative dark-sky illumina-

[i]The WIYN Observatory is a joint facility of the University of Wisconsin-Madison, Indiana University, the University of Missouri, and the National Optical Astronomy Observatory.

[ii]Kitt Peak National Observatory, National Optical Astronomy Observatory, which is operated by the Association of Universities for Research in Astronomy (AURA) under cooperative agreement with the National Science Foundation.

tion correction to produce very flat final stacked images, following the methods of Janesh et al. (2015) and Janowiecki et al. (2015), using the "odi-tools" package[iii]. Our final images are calibrated using catalog fluxes of SDSS stars in the frames (Alam et al., 2015) and our photometric zeropoints typically have rms errors $\leq$0.05 mag.

5.3.3 Archival UV Data

A subset of the HUDS samples fall within the footprint of archival GALEX near ultraviolet (NUV) and far ultraviolet (FUV) observations (Martin et al., 2005; Morrissey et al., 2007). The FUV bandpass ranges from 1344 to 1786 with a PSF of 4.3″ FWHM, and the NUV covers 1771 to 2831 with a 5.3″ FWHM. These bands are sensitive to the hard radiation from young stellar populations, and are thus useful in understanding recent star formation in these sources.

Specifically, Huang et al. (2012a) studied a sample of the 9417 galaxies in the 40% ALFALFA catalog with overlapping SDSS and GALEX coverage, and found SFRs and stellar masses via SED fitting for the sources in their ALFALFA-SDSS-GALEX sample. This includes 30 of the HUDS-B galaxies (the HUDS-BG sample). To avoid introducing systematic trends due to differences in methodology, we restrict our comparisons of stellar masses and SFRs to the larger ALFALFA-SDSS-GALEX sample to these 30 sources, but note that this is a sufficient quantity to understand trends in the HUDS-B sample. Importantly, the sources with available GALEX data - the HUDS-BG sample - have the same distribution of observed properties (color, H I mass, absolute magnitude) as the HUDS-B sample. Thus, any analysis using only the HUDS-BG sources does not introduce a

[iii] https://github.com/bjanesh/odi-tools

selection bias into our results.

Additionally, the three sources with H I synthesis observations are not in the 40% ALFALFA catalog analyzed by Huang et al. (2012a), but do fall within the GALEX footprint. AGC 219533 is clearly detected in medium-deep imaging. AGC 122966 and 334315 are only covered in the much shallower AIS survey, and thus are only marginally detected in smoothed images. We use these data to roughly estimate star formation rates for these sources using standard prescriptions from Kennicutt & Evans (2012), and report the results in Table 5.2.

5.3.4 A Note on Inclinations

Analysis of surface brightness, surface density, and rotational parameters depends in part on the source inclination. However, optical measurements of inclinations in star forming galaxies are difficult without clear near infrared detections of the older stellar populations, an issue compounded by the low S/N of HUDS in SDSS data.

Thus, we approach this issue in two ways. For the three sources with resolved H I data we estimate inclinations from the H I images, using the standard formula:

$$cos^2(i) = \frac{(b/a)^2 - q_0^2}{1 - q_0^2}$$

assuming that the gas forms a circular disk with an intrinsic axial ratio of q_0=0.2, and report the values in Table 5.2. For our sources, the dominant error in this calculation comes from the size of the H I beam; we calculate uncertainties assuming errors of half the beam width along the kinematic major and minor axes. This uncertainty contributes significantly to our estimates of dynamical masses

Table 5.2: Derived properties of HUDs with resolved H I imaging

AGC ID	$\log(M_\star)^a$	SFR^b	$M_{HI}/M_\star$	D^c_{max}	D^d_{HI}	$D^e_{HI,pred}$	S_{syn}/S^f_{ALFA}	i^g	$M^h_{Dyn,8kpc}$	$M^i_{Dyn,Max}$
	log $M_\odot$	$M_\odot$/yr		kpc	kpc	kpc		deg	10^9 $M_\odot$	10^{10} $M_\odot$
122966	8.1	0.022	8.3	44±7	21±7	18±2	1.08	52±19	5.1±3.2	1.0±0.6
219533	7.8	0.030	24	38±3	27±3	24±2	0.96	47±11	10.0±4.1	1.9±0.7
334315	7.8	0.045	23	38±6	26±6	22±2	0.97	52±9	5.2±1.4	1.0±0.3

[a]: Stellar mass calculated from in-house photometry on SDSS images and using the relations from Zibetti et al. (2009); typical errors are 0.3-0.4 dex. [b]: Star formation rate estimated from the FUV GALEX luminosity using the standard relation of Kennicutt & Evans (2012); errors are ~50%. [c]: Maximum extent of H I emission on the sky, uncorrected for beam smearing. [d]: H I diameter measured from 1D RADIAL models at a surface density of $1 M_\odot\ pc^{-2}$. [e] : Predicted H I diameter from Broeils & Rhee (1997). [f] : Ratio of flux recovered in WSRT or the VLA data versus the measured ALFALFA flux. [g] : The inclination, as measured from H I synthesis data. [h] : Dynamical mass with 8 kpc estimated from the H I velocity field. [i] : Dynamical mass estimated from maximum observed H I rotational velocity.

and spin parameters, but is still well enough constrained to provide significant constraints.

For sources without H I synthesis data, we assume that all sources are inclined at 45° for purposes of measuring rotational velocities and spin parameters, and we do not correct our surface brightness measurements for inclination. We assess the impact of these assumptions on our calculated distributions and sample selection by repeating the calculations assuming inclinations measured from the SDSS catalog (which are very uncertain for the HUDS). We find no significant differences in our results, and that our measured central surface brightnesses are consistent with those measured by van Dokkum et al. (2015) within our errors of ~0.2 mag arcsec^{-2}.

5.4 Results

Here we present the optical and H I properties of the HUDS from the ALFALFA survey. Section 5.4.1 describes the optical properties of the galaxies, emphasizing that while they have similarly large extents for their stellar mass, they differ from previously reported UDGs in color and morphology. Section 5.4.2 describes the H I properties of the sources, emphasizing their large H I masses and diameters given their stellar mass.

5.4.1 Optical Properties

The left hand panels of Figure 5.3 show SDSS and ODI color images of three HUDS with synthesis follow up observations. Comparing these images with

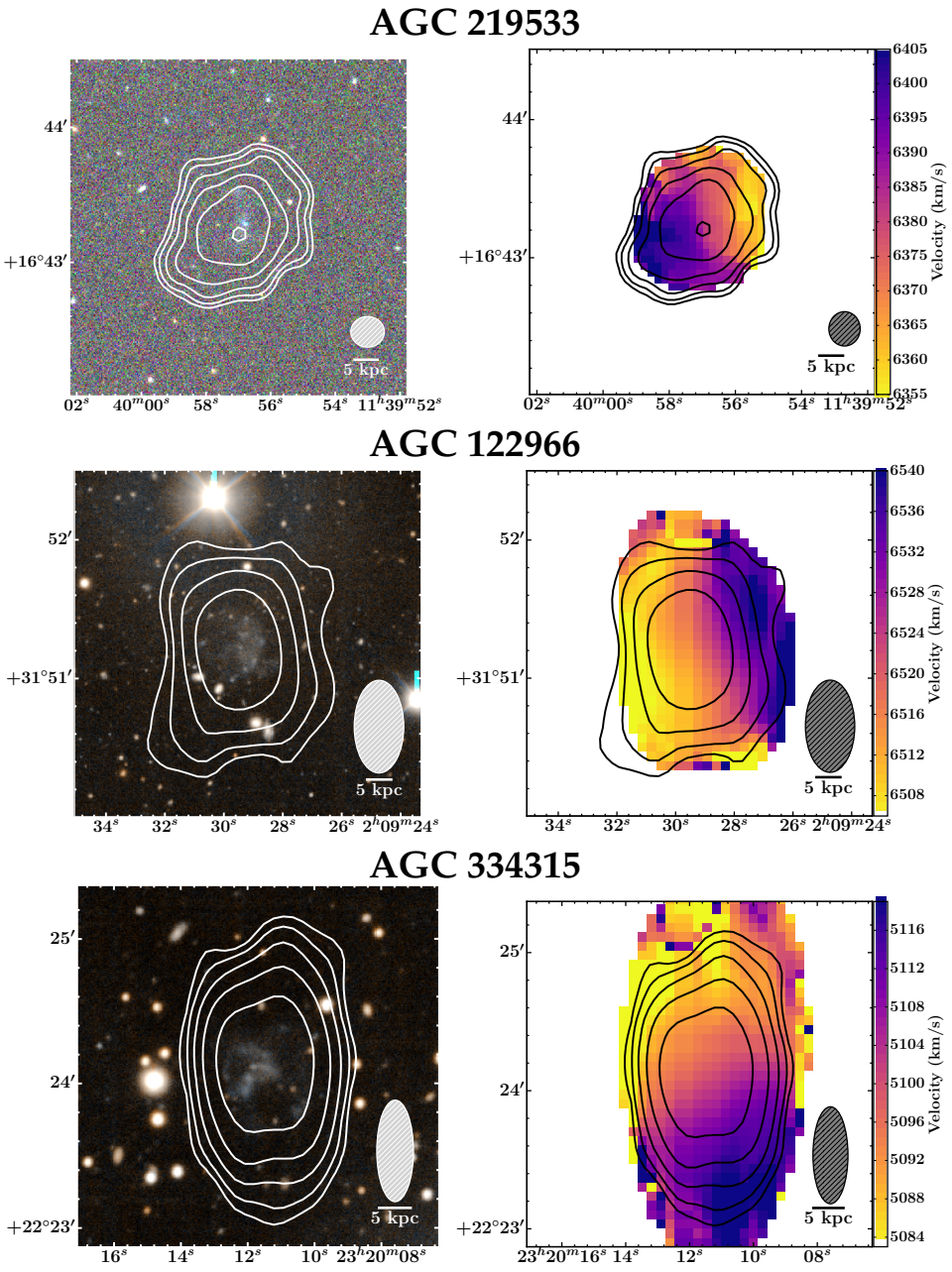

Figure 5.3: H I column density contours at 2, 4, 8, 16, 32, and 64×10^{19} atoms cm^{-2} overlaid on color optical images and moment 1 velocity maps for three HUDS, AGC 219533, 122966, and 334315 from top to bottom. For AGC 219533 the H I data is VLA C-array and the optical data is from SDSS; the others have H I data from WSRT, and optical data from pODI on the WIYN 3.5m. The optical emission is blue, diffuse, and shows irregular morphology. The H I is resolved even at this low physical resolution, is significantly extended relative to the diffuse optical emission, and shows evidence of ordered rotation. RA and Dec are in J2000 coordinates.

those of, e.g., the Coma UDG DF 17 pictured in Figure 5.2, emphasizes the morphological difference between the HUDS and other UDGs. While DF 17 shows a smooth stellar distribution even in deep CFHT imaging, deep WIYN imaging of two HUDS show clumpy, irregular morphologies, with knots of comparatively intense star formation. AGC 122966 shows two arcs superimposed on extended faint emission, while AGC 334315 similarly shows brighter arcs crisscrossing fainter extended emission. Both stellar populations appear quite disturbed, with the peak surface brightness offset from the center of the low surface brightness emission.

These morphological differences can have implications for the definition of "ultra-diffuse." That these sources are significantly extended and very low surface brightness is clear: SDSS and pODI imaging measure diameters ranging from 24 to 70 arcseconds, which translates to diameters between 11 and 25 kpc at their respective distances. However, profile fitting in the traditional sense is complicated by the lack of a smooth profile. While the central surface brightness measured from profile fitting corresponds well with the source peak surface brightness for smooth, quiescent sources, the peak surface brightness may be offset from the center of light in these patchy sources, making estimates of the surface brightness profile somewhat sensitive to the chosen aperture center.

The color images in Figure 5.3 also emphasize the blue nature of the stellar population of HUDS. The top panel of Figure 5.4 shows the color distribution of the HUDS-B and HUDS-R samples compared with other ALFALFA galaxies that meet matching distance and isolation criteria, and the average color estimate from van Dokkum et al. (2015). The average g-i color of HUDS-B is 0.45, with a standard error of 0.02, significantly bluer than the 0.8±0.1 estimated by

van Dokkum et al. (2015), and also bluer than the 0.65±0.02 estimated by Román & Trujillo (2017a) for UDGs outside of clusters. The color appears only slightly bluer than the color distribution of star forming ALFALFA sources within a similar mass range (see Figure 5.4), suggesting that their color is more directly tied to their H I than to their diffuse stellar distribution.

These differences in color again have important implications for the definition of an "ultra-diffuse" population. For example, in order to appropriately make the comparison between the samples plotted in Figure 5.1 we have converted sources observed in g and r to V band, which falls between the g and r filters. Thus, in plots made with g band values the HUDS would shift to brighter values relative to the UDG population, and would shift to fainter values for plots in r band.

A second, more striking implication, however, is that if the recently formed (bright, blue) stars were not present in these sources, the remaining stellar populations would be significantly fainter. Thus, the older stellar populations of optically selected UDGs are likely significantly brighter than any (currently invisible) older stellar populations in these HUDS. Thus, though they are similar sources in terms of measured parameters, these sources may have significant physical differences from other UDGs. However, their low surface brightness nature still implies a connection: it may be that these sources are progenitor UDGs, fainter and less evolved versions of their more evolved cluster counterparts.

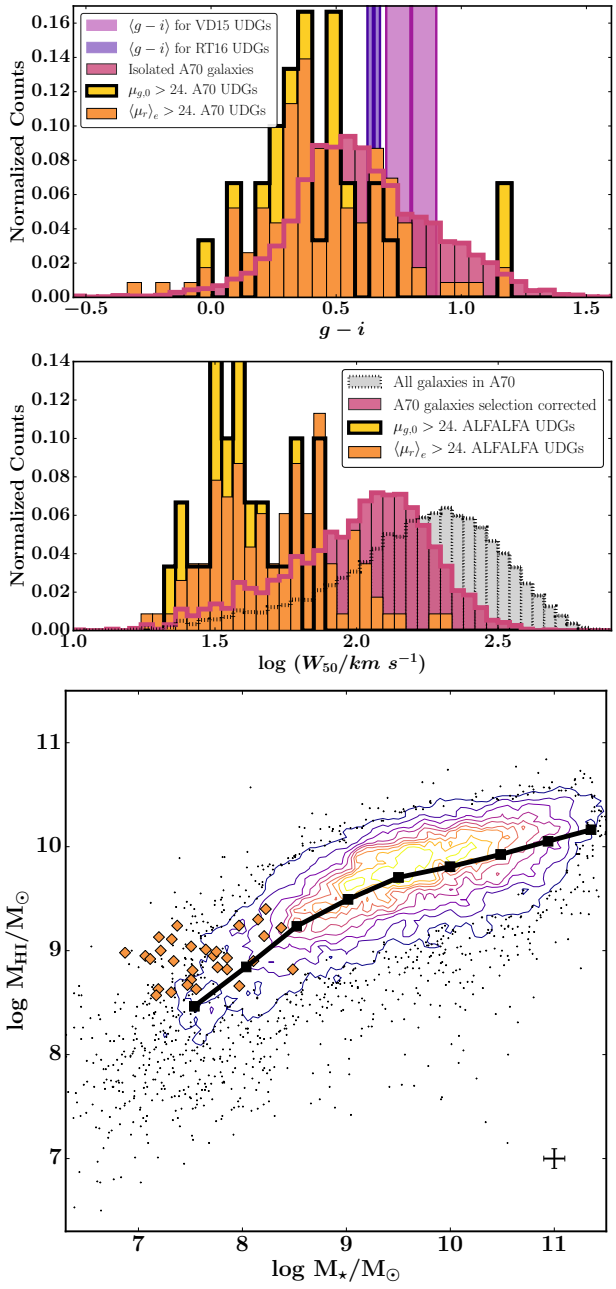

Figure 5.4: Top: The color distribution of HUDS (yellow and orange for HUDS-R and HUDS-B respectively), compared with the rest of the ALFALFA population matching similar isolation and distance selection criteria, the average value computed from stacking in van Dokkum et al. (2015), and the average value for the sources in filaments from Román & Trujillo (2017a). Middle: The distribution of H I velocity widths as measured at the 50% flux level of HUDS (yellow and orange for HUDS-R and HUDS-B respectively), compared with the rest of the ALFALFA population (light grey), and the the ALFALFA population corrected for inclination and mass selection effects (pink). HUDS tend to have quite narrow velocity widths, even when correcting for selection effects. Bottom: H I mass versus stellar mass for ALFALFA sources from Huang et al. (2012a), compared with the HUDS-BG sample. HUDS tend to be H I-rich relative to their stellar mass.

5.4.2 HI Properties

In contrast with optically selected UDGs in denser environments, the isolated HUDS are clearly detected in H I, with H I masses ranging from $10^{8.6}$-$10^{9.3} M_{\odot}$. In fact, these sources are gas rich, even relative to the normal gas-bearing galaxy population. The bottom panel of Figure 5.4 shows the H I mass - stellar mass scaling relation for H I selected galaxies from Huang et al. (2012a). For a given stellar mass, the HUDS have fairly high gas fractions relative to the rest of the ALFALFA population, similar to fainter and smaller dwarf irregulars (e.g., Lee et al., 2003), and pushing into a similar parameter space to (almost) dark sources like those reported in Janowiecki et al. (2015). This makes sense given our selection criteria: the minimum distance threshold eliminates sources with H I masses $\lesssim 10^{8} M_{\odot}$, and our absolute magnitude limit places a stellar mass threshold of $\sim 10^{9} M_{\odot}$. However, while this selection eliminates sources with gas fractions <0.1, the mean gas fraction M_{HI}/M_{*}=35 may suggest a potential connection between high gas fraction and the diffuseness of the stellar population. Regardless, the H I dominates the baryonic content of these galaxies. Whether we interpret them in terms of their stellar mass or their baryonic mass thus makes a significant difference, a point we return to in section 5.5.

The H I Distribution

While these HUDS appear to have large H I masses relative to their stellar mass, UDGs are optically defined by their large radii for their stellar masses. Thus, for the three sources with existing H I synthesis observations we analyze their H I radii and distribution. Estimates of their properties are limited by the low physical resolution of the data (6 - 14 kpc), but are still sufficient to constrain

their extended nature.

All three sources are resolved with multiple beams in H I, which allows us to estimate the radii of the sources, albeit with a fairly large uncertainty. As a first order estimate, we place an upper limit on the size of each source by measuring the largest projected extent on the sky, uncorrected for the effects of beam smearing. Specifically we measure largest extents of 44±7, 38±3, and 38±6 kpc for AGC 122966, 219533, and 334315 respectively, assuming uncertainties of half the beam width along the major axis. We next estimate radii by fitting the observed H I profile with tilted rings every half beam width using the GIPSY task ELLINT, assuming a constant position angle and inclination, and then estimating radii at a surface density of 1 $M_\odot$ pc^{-2} to compare to measurements from The H I In Nearby Galaxies Survey (THINGS; Walter et al., 2008) described below. We choose the major axis to be the kinematic major axis (see section 5.4.2), which approximately corresponds to the morphological major axis, except in the case of AGC 122966, where the morphological major axis is poorly determined due to the elongated WSRT beam.

However, fitting flux in rings is limited by the minor axis resolution, so we additionally estimate the surface density profile using Lucy-Richardson deconvolution (Lucy, 1974; Warmels, 1988), which collapses the flux to a 1D profile along the major axis, and then models that profile as a disk of uniform coplanar rings. This method has the advantage of not requiring an estimate of the inclination of the sources, and is insensitive to low resolution along the minor axis, but is still limited by the resolution along the major axis. Outside of the central beamwidth, Warmels (1988) estimate the uncertainty in the modeling as ~25%. The surface density profiles estimated from the Lucy method are consis-

tently higher than those from the 2D modeling with ELLINT by ~25%, but the measured radii are consistent within half the beam width, our estimated error.

We then use these radial models to estimate the radii at 1 $M_\odot$ pc^{-2} to roughly compare to the expected radii from standard scaling relations. Using the H I mass-radius relation from Broeils & Rhee (1997) (which is similar to the relation from Wang et al., 2016) we compute expected H I diameters from the measured H I masses. The ratios of the measured diameters to the predicted diameters are given in Table 5.2. All of the sources lie above the relation, i.e., their H I radius is extended for their H I mass. However, this comparison is still limited by the effect of the beam, which tends to push flux to larger radii, exaggerating the size of a galaxy, while reducing the measured column density, which can underestimate the size of the galaxy for low density systems. Thus, given the uncertainties in the radius measurements, all three sources are consistent with the scatter in the relation. We note that while the H I radii appear to be consistent with the expected radii for their H I mass, as noted above, all three sources have large H I masses relative to their stellar populations. Thus, these sources are significantly more extended than typical H I-rich sources with comparable stellar mass.

As a suggestive exercise, we compute the median H I profile of 4 dwarf galaxies and 4 ~L$_\star$ galaxies from the THINGS sample (Walter et al., 2008), and compare the results to the results for HUDS. We used profiles fitted using the tilted rings method from Leroy et al. (2008), and smoothed them to a physical resolution of 7 kpc to approximately compare with the physical resolution of the measured HUDS. The results of this exercise are shown in Figure 5.5. The beam smeared profiles of the HUDS are shown as thick colored lines, and the

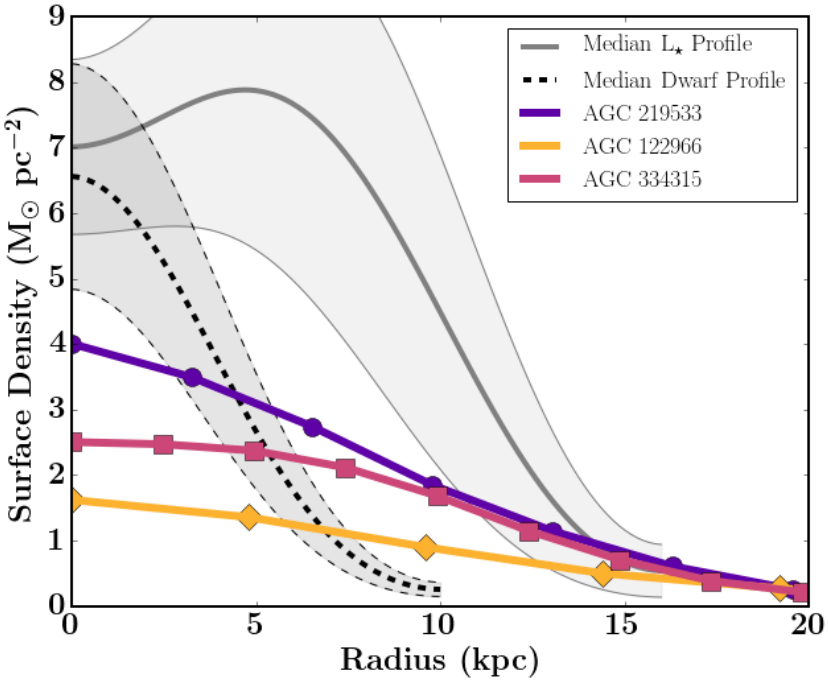

Figure 5.5: Low resolution surface density profiles of HUDS with resolved H I-synthesis imaging, compared with the median profiles of the dwarf galaxies and ~L$_\star$ galaxies from THINGS (Leroy et al., 2008), smoothed to a physical beam resolution of 7 kpc, to match the resolution of the observed HUDS. The three HUDS are significantly more extended than the typical H I-rich dwarf, which is approximately a point source at 7 kpc resolution, and appear to be somewhat lower column density than the typical L$_\star$ galaxy, though beam smearing limits interpretation of the surface density within the central beam.

smoothed median profiles and their spread are shown as grey shaded regions. Importantly, the H I disks are more extended than typical dwarf galaxies which are point sources at 7 kpc resolution, and more consistent with H I disks of L$_\star$ spirals. The average surface density seems to be somewhat lower than the typical THINGS galaxies, suggesting that these sources may be somewhat more diffuse in H I than typical H I sources. However, we emphasize that this result is at best suggestive due to the small number statistics and low resolution; higher resolution observations of a larger sample will be required to confirm this suggestion.

The H I Rotation Velocities

The right hand panels of Figure 5.3 shows the H I velocity fields for the three sources with resolved synthesis observations. All the sources show signs of ordered motions, and evidence of a significant velocity gradient, though the gradient is only over a relatively narrow range. Indeed, AGC 219533 has the largest velocity width of 66 km s^{-1}. The relatively narrow velocity widths of the three resolved sources, however, are consistent with the ALFALFA velocity widths for the entire H I-bearing UDG sample. The center panel of Figure 5.4 shows the velocity distribution of HUDS compared with a similarly selected ALFALFA sample. The mean velocity width of the HUDS-B (HUDS-R) sample is 59 (44) km s^{-1}, compared to 194 km s^{-1} for all ALFALFA galaxies, and 119 km s^{-1} for ALFALFA galaxies with similar selection criteria. Specifically, we expect lower velocity widths for HUDS given their lower baryonic masses, and also due to the fact that surface brightness is a function of inclination. However, even after removing sources with H I mass (log ($M_{\rm H\,I}/M_{\odot}$)>9.5) and with inclinations >66 degrees (approximating the inclination distribution of HUDS), the HUDS still populate the low velocity width part of the distribution. This result is not entirely unexpected, due to their lower mass and a surface brightness selection against edge-on galaxies. We return to this in section 5.5.2.

Since the sources are only resolved with a few beams along the major and minor axes, traditional fitting of tilted ring models to the 2D velocity profile tend to overestimate the dispersion and underestimate the rotational velocities due to the many velocities along the lines of sight contained within the beam. Thus we instead estimate the rotation curve of the sources by fitting the "envelope" of velocities observed at each position in a position-velocity (PV) diagram (e.g.,

Sancisi & Allen, 1979). We follow the methods of Hallenbeck et al. (2014), using the GIPSY task ROTCUR to estimate the position angle of the velocity field (using tilted ring models), and then extract a position velocity field using a slice 2 beams wide along the major rotational axis. We then extract the spectrum at each position and fit a 3rd order Gauss-Hermite polynomial, and estimate the final rotation curve as the velocity where the integrated area under the curve is 3.3% from the approaching or receding edge. We then average the rotation values from the approaching and receding envelope, and correct for inclination by dividing by sin(i).

We note that the inclination uncertainty contributes significantly to the rotational uncertainty (section 5.3.4), and that our estimated rotation velocity could be biased by gas inflow or outflow, enhanced velocity dispersion, and the assumptions of a disk like structure with a negligible disk scale height. In spite of these limitations, however, the data are still sufficient to constrain the allowed parameter space, as we discuss below.

5.5 Discussion

In section 5.4 we emphasized that while the HUDS have similar surface brightnesses, optical radii, and magnitudes to UDGs, they have very different colors and morphologies, are all very isolated, and all have significant H I. Thus, their relationship to quiescent UDGs is unclear. Like other UDGs, they may be star-poor, failed ~$L_\star$ galaxies with suppressed star formation laws, or they may be H I-rich, extended dwarfs that only recently acquired their gas. Here we consider the star formation laws and velocity width and rotation curves of HUDS

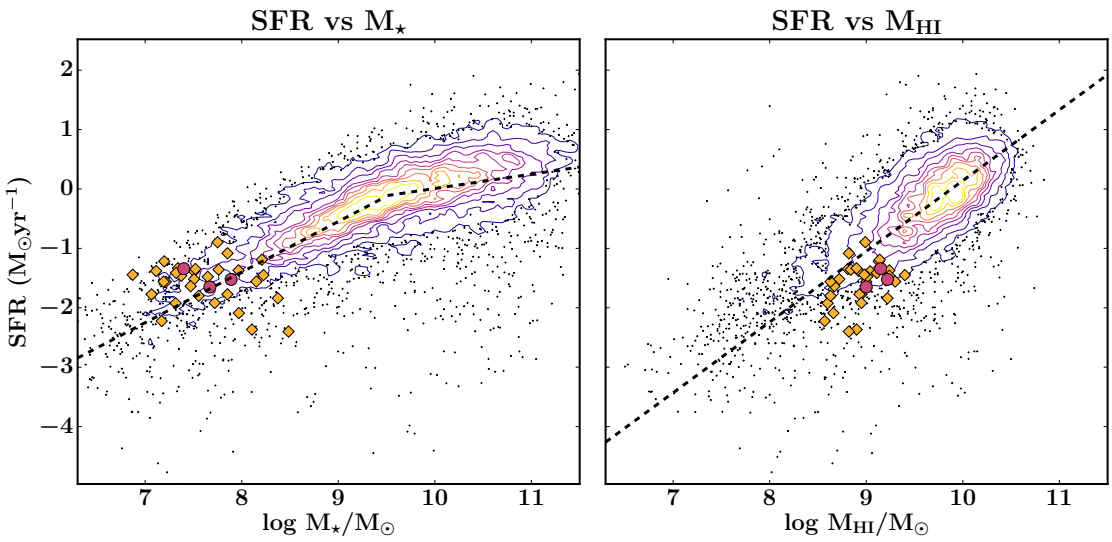

Figure 5.6: SFR versus stellar and H I mass of the HUDS-BG galaxies (yellow diamonds), plotted against the full Huang et al. (2012a) sample. The star formation rate of these sources seems typical of H I selected sources of the given stellar mass, but low for galaxies with the given H I mass. SFRs are taken from Huang et al. (2012a), and are calculated by SED fitting to GALEX+SDSS UV broadband data. The dashed lines represent the fitted trends from Huang et al. (2012a). The three HUDS with follow up observations are shown by pink circles.

as potential evidence that they are extended dwarfs in high angular momentum halos.

5.5.1 Star Formation in H I-bearing UDGs

H I selected galaxies are well known to be blue, and undergoing recent star formation (e.g., Huang et al., 2012a). The HUDS are no exception. Figure 5.6 shows the SFR versus stellar and H I mass of the 33 HUDS-BG galaxies (section 5.3.3) plotted against the full ALFALFA-SDSS-GALEX sample from Huang et al. (2012a). The HUDS-BG sample has moderate SFRs ranging from 0.01-0.1 $M_\odot$ yr^{-1}. Indeed, in spite of their low surface brightness, the HUDS appear to have normal star formation rates for their stellar mass, i.e., their specific star

formation rates are consistent with the overall ALFALFA sample.

However, the right hand panel of Figure 5.6 shows the SFRs compared with the H I mass. Though the SFRs for the HUDS fall within the range covered by the ALFALFA sample, they are low compared to the average ALFALFA galaxy for a given H I-mass, i.e., that they have very low star formation efficiency (SFE=SFR/M_{HI}). The low SFE of these galaxies indicates that their current gas consumption time (the Roberts time, $t_R = M_{HI}/SFR$) is very long, even relative to a H I selected population. The average t_R, for the HUDS is 35 Gyr, compared to 3 Gyr for the optically selected GASS sample (Schiminovich et al., 2010), and 8.9 Gyr for ALFALFA. This is not simply a selection effect: t_R is nearly independent of stellar or H I mass (Huang et al., 2012a).

There are at least two potential explanations for the long gas consumption time. If these galaxies continue to form stars at the same rate, they may be, in some sense, "failed" galaxies with unusually stable disks and highly inefficient star formation. Whether they are "failed" $L_\star$ galaxies or "failed" smaller galaxies (like the Large Magellanic Cloud) depends on their estimated halo masses (see section 5.5.2). In the latter case, these sources may be thought of as "failed" dwarfs, and may suggest a link between the inefficiency of their star formation and their large optical radii. It may also be that these sources are selected, by means of their surface brightness and isolation, to be observed in a special time in their history. If, as Di Cintio et al. (2017) suggest, UDGs have bursty SF histories, we may be observing the HUDS during a period of significant gas infall, before they experience a significant increase in their star formation rate. While the resolved H I imaging of these sources is smooth at the current resolution, there are not enough beams across the sources to definitively search for signs

of inflow or outflow. Moreover, a moderate enhancement in SFR would make these galaxies appear brighter, and therefore too high surface brightness to be selected as "ultra-diffuse," since observations of the older stellar populations under starbursts are difficult (Janowiecki & Salzer, 2014).

5.5.2 The Dark Matter Halo

The properties of the host dark matter halos of UDGs are poorly understood. As discussed in section 5.1, the strongest constraints come from dynamical studies of globular clusters and from scaling relations with globular cluster counts, but are limited by the spatial extent of the globular cluster distribution. Here we attempt to constrain the properties of the dark matter halos of the HUDS. While the three sources observed with synthesis telescopes are only resolved with 3-6 beams, the large extent of the sources still allows us to significantly constrain the halos out to ~20 kpc.

The Halo Profile and Mass

The right hand panel of Figure 5.7 shows the dynamical mass of the HUDS as inferred from the H I rotation curves estimated in section 5.4.2 (black squares, pentagons, and hexagons), compared with the dynamical mass estimates from globular cluster spectroscopy for UDGs from van Dokkum et al. (2016) (DF 44; grey triangle) and Beasley et al. (2016) (VCC 1287; grey circles), and predicted models from Di Cintio et al. (2017) (colored lines). The uncertainties in geometry dominate the uncertainties in estimating the rotation velocity. However, even accounting for these, the H I data provides significant constraints on the

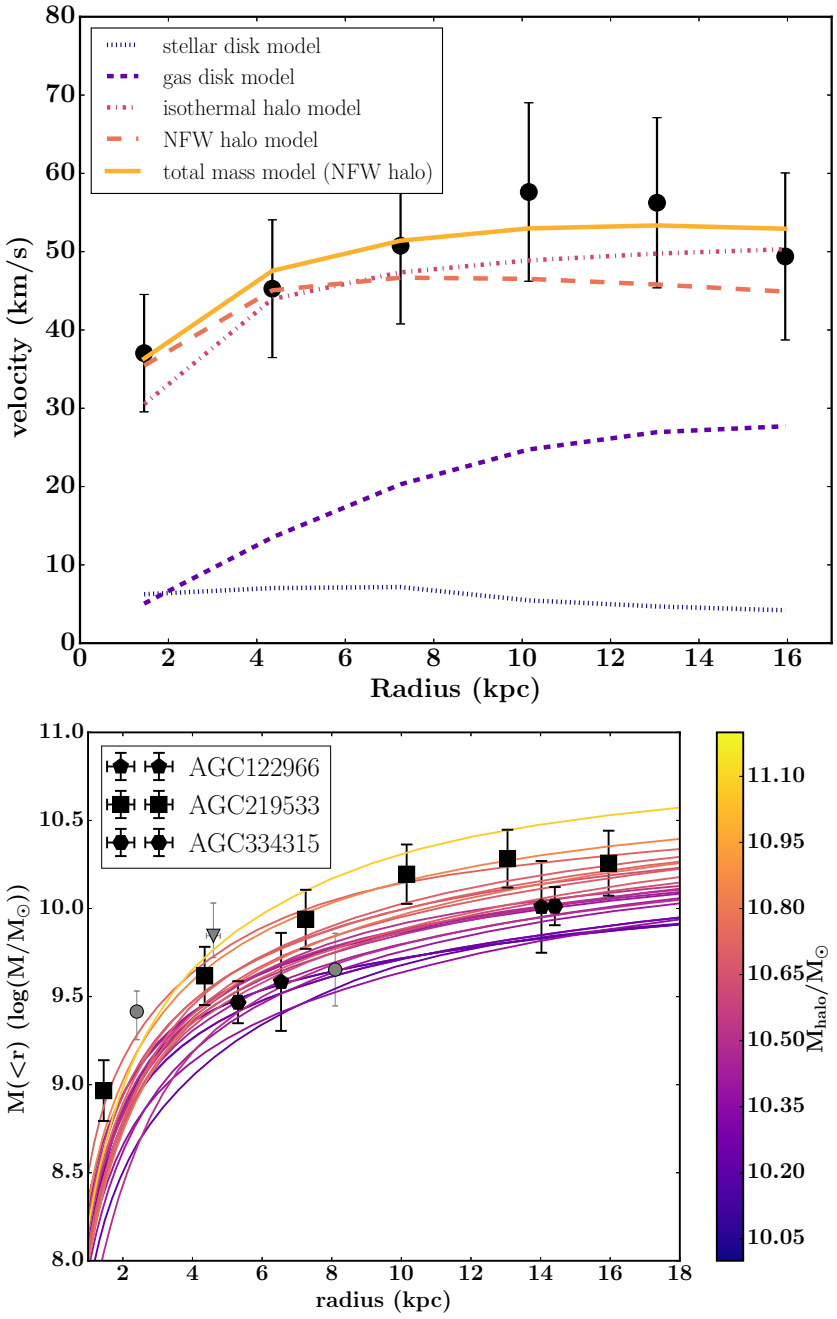

Figure 5.7: Top: Rotation curve decomposition for AGC 219533. The modeled H I disk accounts for a large portion of the assumed rotation, and suggests a halo with a low concentration parameter. Bottom: Comparison of calculated mass profiles for the sources with resolved synthesis imaging (black squares, pentagons, and hexagons), versus the predicted profiles from Di Cintio et al. (2017) based on NIHAO simulations (Wang et al., 2015). The dynamical mass estimates from Beasley et al. (2016) and van Dokkum et al. (2016) are marked by grey circles and a grey triangle respectively. The measured and predicted profiles show good agreement, suggesting halo masses below $10^{11} M_\odot$.

dark matter masses. All three sources have measured dynamical masses consistent with or slightly larger than the measurements from Beasley et al. (2016) of VCC 1287, and slightly smaller than the measurement from van Dokkum et al. (2016). Specifically, Beasley et al. (2016) find a dynamical mass of 4.5±2.8×$10^9 M_\odot$ within 8.1 kpc, while the HUDS give values ranging from 5-10×$10^9 M_\odot$ within a similar radius (and with similar errors - see Table 5.2). These dynamical estimates yield dynamical to stellar mass ratios for these sources consistent with those reported in Beasley et al. (2016), though the error bars are large. The dynamical to baryonic mass ratios are significantly smaller, however, since the H I mass is large compared with the stellar mass.

The HUDS also match reasonably well with the predicted profiles from Di Cintio et al. (2017), though for the best resolved source AGC 219533, the measured rotation curve appears somewhat flatter than those predicted. We estimate a halo mass from the best fitting profiles from Di Cintio et al. (2017) of ~$10^{10.7} M_\odot$for AGC 219533, and somewhat smaller masses of $10^{10.4}$ and $10^{10.3} M_\odot$for AGC 334315 and 122966 respectively. However, the extrapolation from dynamical mass to total halo mass necessarily relies on the type of model fit. We note that abundance matching (using the data from Papastergis et al., 2012) implies that galaxies with the baryonic masses of these sources should live in halos with log $M_{halo}/M_\odot \gtrsim$11.1. However, this estimate seems unreasonably large given the dark matter mass estimated within r=20 kpc.

As an instructive exercise, we attempt to model the rotation curve as composed of a gaseous disk, stellar disk, and dark matter halo using the GIPSY task ROTMAS for AGC 219533. The left hand panel of Figure 5.7 shows the best fitting model stellar and gas disk contributions to the rotation, assuming the mass

surface density distributions shown in Figure 5.5, multiplied by 1.3 to account for the presence of helium (and assuming an infinitely thin disk, an assumption that has little effect on the analysis given the size of the errors). The remaining rotation is modeled as the result of either an pseudo-isothermal or Navarro–Frenk–White (NFW; Navarro et al., 1997) halo (shown as dash-dotted and long dashed lines respectively), such that $V_{obs}^2 = V_{\rm gas}^2 + V_*^2 + V_{\rm DM}^2$.

We also note that while low surface brightness galaxies usually exhibit steadily rising rotation curves that are not well fit by NFW profiles (e.g., McGaugh & de Blok, 1998), AGC 219533 appears to flatten out, potentially suggesting that is is more consistent with the NFW profile, similar to the extreme gas-rich, high spin parameter, low surface brightness galaxy UGC 12506 (Hallenbeck et al., 2014). However, while these results are suggestive, the limited resolution of our current observations cautions against over interpreting these results.

The Halo Spin Parameter

While the analysis in section 5.5.2 indicates that HUDS are likely to occupy dwarf halos, it does not explain the mechanism for the extended radii. Here we attempt to estimate the spin parameters of the dark matter halos of HUDS, to test the prediction that "ultra-diffuse" sources are spatially extended due to large halo spin parameters (Amorisco & Loeb, 2016).

The spin parameter is a dimensionless quantity that describes the angular momentum in the halo:

$$\lambda = \frac{J * |E|^{1/2}}{G * M^{5/2}}$$

where J is the halo angular momentum, E is the energy, and M is the halo mass. The halo spin parameter is difficult to constrain observationally, since almost any λ can fit a halo with given parameters from rotation curve fitting. Instead, we employ the common practice of simplifying the calculations by assuming that the dark and baryonic matter are coupled such that their angular momentum per unit mass (j and j_b respectively) are equal (e.g., Mo et al., 1998). Thus we are technically calculating the modified spin parameter $\lambda' = j_b/j \times \lambda$ (henceforth, we will drop the prime).

Under this assumption, we approach the calculation of λ two different ways. We first follow Huang et al. (2012a), measuring the exponential disk scale length R_d from SDSS and the rotation velocity V_{rot} from the ALFALFA H I line width ($V_{rot} = W_{50}/2/sin(i)$), and adopting the λ estimator from Hernandez et al. (2007):

$$\lambda = 21.8 \frac{R_d[kpc]}{V_{rot}[km/s]^{3/2}}$$

This estimator further assumes self-gravitating, virialized, isothermal dark matter halos that dominate the galaxy's potential energy, flat rotation curves, and, importantly, a constant disk mass fraction M_*/M_{total} of 0.04. We assume that all sources are inclined at 45°, as discussed in section 5.3.4.

The left panel of Figure 5.8 shows the results of this analysis. The distribution for all galaxies in the ALFALFA 70% sample is shown in dark pink. The distribution for the HUDS-R and HUDS-B samples are show in yellow and orange respectively, and appear to be significantly elevated relative to the rest of the ALFALFA distribution, i.e., the the radii of these sources are large given the rotation velocities of their disks. A K-S test estimates a probability that they are drawn from the same distribution as 10^{-18} and 10^{-34}.

To better understand the potential impact of selection effects and our other

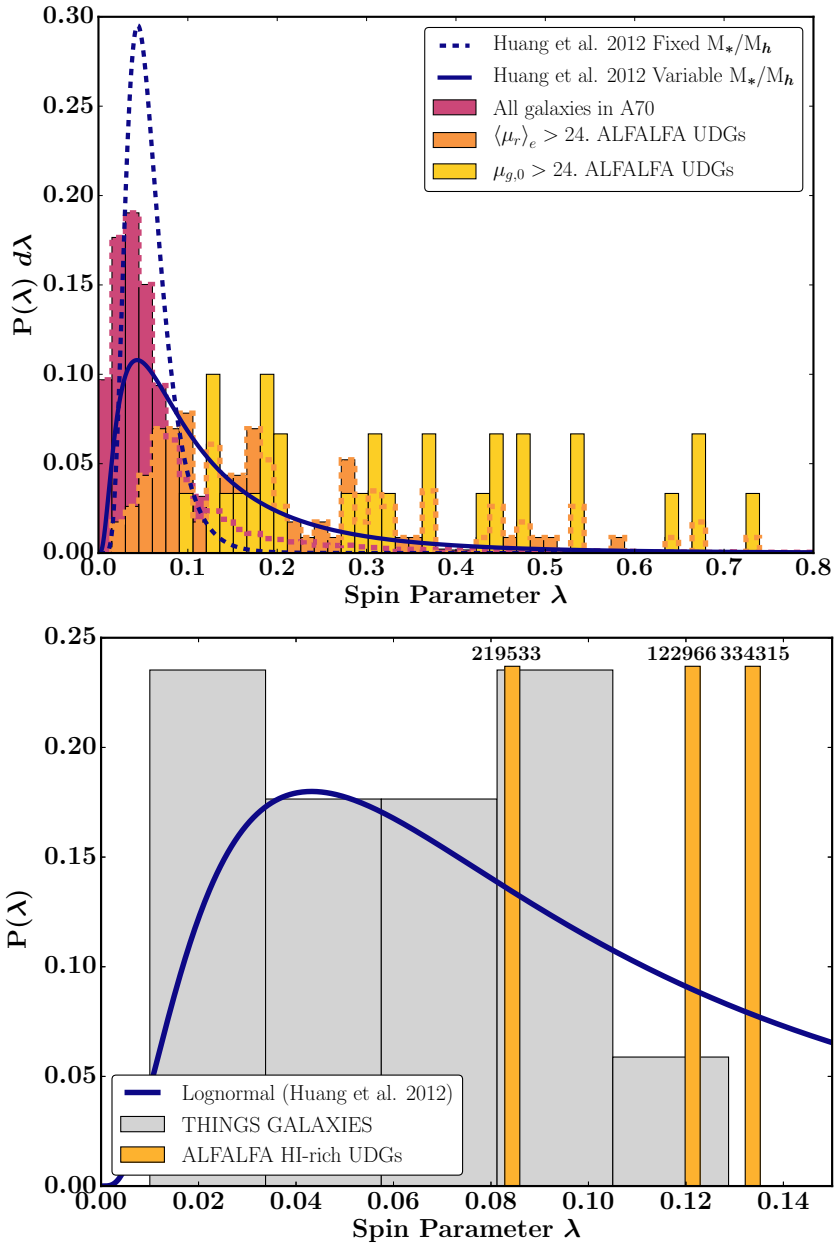

Figure 5.8: Top: Spin parameter distribution of the HUDS-B and HUDS-R samples compared with the distribution for all ALFALFA sources. Spin parameters are calculated assuming an inclination of 45° following Huang et al. (2012a). The blue dashed curve shows the distribution from Huang et al. (2012a) for a volume limited H I selected sample, and the blue solid curve shows the result from Huang et al. (2012a) under the assumption of a variable halo mass fraction. Bottom: Comparison of the spin parameters for the three resolved HUDS to the THINGS sample, calculated using the method from Hallenbeck et al. (2014). The solid blue curve is the same as in the left hand panel. These results may suggest that these isolated, HUDS preferentially reside in high spin parameter halos.

assumptions, the left hand panel also shows the lognormal fit to the spin parameter distribution of H I selected sources derived by Huang et al. (2012a) through similar analysis (blue dashed curve). Like the spin parameters derived by Huang et al. (2012a), the ALFALFA 70% spin parameters follow a lognormal distribution, but have a lower mean and wider dispersion, demonstrating the impact of source selection. The distribution shown in pink includes the entire ALFALFA sample, whereas the blue dashed curve is restricted to a volume limited sample from the ALFALFA 40% catalog, and only includes sources over the absolute magnitude range -20 > M_r > -23 mag. The difference between the distributions is also in part due to the assumption of constant inclination.

Further, the left hand panel also shows the lognormal distribution derived by Huang et al. (2012a) under the assumption the sources do not have a constant halo mass fraction, but instead have mass fractions derived from abundance matching (dark blue solid curve). As discussed in Huang et al. (2012a), allowing the mass fraction to vary can have a large impact on the distribution. Still, the calculated spin parameters for the HUDS are large compared to the overall sample in all three cases, though we note that if the HUDS reside in large halos for their stellar masses as predicted through abundance matching, their estimated spin parameters would be significantly lower.

The trend to high spin parameters is perhaps not entirely unexpected given our selection of extended sources, and the observation that they have high gas fractions relative to the ALFALFA sample (section 5.4.2). Indeed, Huang et al. (2012a) showed that sources with high gas fractions tend to have high spin parameters for a given stellar mass, and Obreschkow et al. (2016) suggest that gas fraction depends on a global stability parameter which scales linearly with the

angular momentum of the disk. Thus, the high estimated spin parameters make sense in light of the sample's observed gas fractions.

For resolved sources we can do a somewhat more detailed estimate of the modified halo spin parameter. We follow the procedure detailed in Hallenbeck et al. (2014), which, in brief, estimates the angular momentum of the halo by summing the product of the H I disk mass, velocity, and radius at each point on the rotation curve, and assuming the angular momentum of the halo scales with that of the baryons. The energy is calculated from the maximum velocity from the isothermal halo fit, and the halo mass is estimated from abundance matching. We note that, as discussed in section 5.5.2, abundance matching poorly estimates the total halo mass for these sources. Thus we also estimate spin parameters assuming the halo masses derived from comparison to the models from Di Cintio et al. (2017), and discuss the effect on the results below.

The right hand panel of Figure 5.8 shows the distribution of spin parameters for resolved THINGS galaxies computed by Hallenbeck et al. (2014), which approximately follow the lognormal distribution for the 40% ALFALFA sample (also plotted in the left panel) from Huang et al. (2012a). The three HUDS with synthesis observations, assuming the halo masses from Di Cintio et al. (2017), are overplotted as yellow bars. Though this analysis uses resolved rotation curve fitting rather than SDSS radii and ALFALFA linewidths, the 3 sources again appear to have higher spin parameters than most of the THINGS galaxies.

However, it is important to note that if one instead assumes the halo masses from abundance matching, which are larger by a factor of ~4, the spin parameters are reduced by the same factor, and fall squarely within the THINGS distribution. Also, for 2 of the 3 sources, the values estimated from our resolved

analysis are significantly lower than those estimated from the velocity width and optical radius. This is likely due to the low physical resolution relative to the sources from Hallenbeck et al. (2014), which tends to suppress the j value, and the comparatively large $r_{optical}/r_{HI}$, which increases the spin parameter measurement in the unresolved method (which relies on optical radii) relative to the resolved method (which relies on H I radii measurements). With only 3 sources, we hesitate to read more into this.

With these caveats in mind, the results in this section still suggest that if the assumptions used to calculate the spin parameters are valid and the halo masses are indeed more consistent with dwarfs, then HUDS may reside in high spin parameter halos.

5.5.3 The Nature of Isolated HI-bearing Ultra-Diffuse Sources

While further observations will be necessary to fully understand the connection between HUDS and other UDGs, the observations presented here are consistent with the predicted population of reasonably isolated UDGs with large gas fractions from Di Cintio et al. (2017). More, these data begin to paint a picture of isolated HUDS as extremes in the dwarf galaxy population. Their dynamical mass estimates suggest that at least the 3 resolved HUDS are inconsistent with being failed $L_\star$ galaxies. While this result necessarily relies on assumptions about the disk thickness, and the effects of the beam, in general, these systematic uncertainties would tend to reduce the estimated halo mass. The effect of a thick disk would be to underestimate the inclination, thus overestimating our rotational velocities. Additionally, though beam smearing can tend to underes-

timate velocity gradients and overestimate velocity width, our envelope fitting technique (section 5.4.2) functions as an effective upper limit on the velocity gradient.

Further, while the large H I masses and correspondingly large radii are consistent with a range of halos, the large gas fractions and the star forming characteristics of the HUDS seem more consistent with sources of their stellar mass than their H I mass. Though their low SFE is what we might expect if these sources were failed $L_\star$ galaxies, it also consistent with low density dwarfs or sources that have recently experienced gas accretion.

These results, in turn, support potential scenarios that connect HUDS to other UDGs in dwarf halos. One potential scenario is one where isolated gas-bearing "ultra-diffuse" sources continue to inefficiently form stars until they fall into clusters or groups and have their gas stripped, quenching star formation. In time, the blue colors would fade and the clumpy morphologies would disappear. Indeed, Román & Trujillo (2017b) recently estimate that 6 "progenitor" UDG sources on the edges of groups (with properties somewhat similar to the HUDS-B sample), might fade ~1.5 mag arcsec^{-2} if they evolve passively for 6 Gyr.

Then again, it is also possible that HUDS are an independent population. In this scenario, we may be observing them at a particularly interesting period of gas accretion before they are transformed by significant star formation. Thus, it would undergo a significant increase in surface brightness as it evolves. Detailed, high resolution study of the gas dynamics of these sources will be necessary to explore this possibility further.

Yet another possibility is that the HUDS are not a uniform physical population, and instead result from multiple independent mechanisms. During the review process for this work, Trujillo et al. (2017) and Papastergis et al. (2017) have also reported the detection of H I-bearing "ultra-diffuse" sources, but their connection to the HUDS presented here is not yet clear. The source from Trujillo et al. (2017), UGC 2162 appears smaller and brighter than the sources in this sample - perhaps suggesting some connection to the smaller SHIELD galaxies (e.g., Cannon et al., 2011; McQuinn et al., 2015; Teich et al., 2016), and Papastergis et al. (2017) suggest the possibility of at least two populations of isolated UDGs, pointing to the need for significant future work in this field.

5.6 Conclusions

Here we investigate the properties of isolated, very low surface brightness, "ultra-diffuse" galaxies detected in the ALFALFA survey, and present follow up observations of three of these extreme sources. The main conclusions of this paper are:

1. There exists a substantial population of H I-bearing ultra-diffuse sources (HUDS) with similar surface brightnesses, masses, and radii to recently reported "ultra-diffuse galaxies." We select samples of sources from ALFALFA to match optical selection criteria of "ultra-diffuse" galaxies and find 30-115 HUDS (depending on where we define the surface brightness cut) in the ~5000 isolated ALFALFA galaxies with 25< Dist <120 Mpc.
2. The HUDS are significantly bluer and have more irregular morphologies than their non-isolated counterparts. They appear to be forming stars at

typical rates of H I-selected galaxies for their stellar mass.

3. The HUDS are H I-rich for their stellar mass; the sources have elevated M_{HI}/M_* ratios. Thus, these galaxies have very low star formation efficiencies, with gas consumption timescales longer than a Hubble time.

4. The three resolved HUDS have large H I disks, that extend well beyond their diffuse stellar counterparts, and are similar to the H I radii measured for $L_\star$ spiral galaxies. The H I appears to be relatively "diffuse" and low column density, but it is not "ultra-diffuse"; its extent is only slightly larger than predicted by H I mass-radius scaling relations.

5. HUDS have relatively narrow velocity widths compared with the rest of the ALFALFA sample, even when correcting for inclination and mass selection effects. This, coupled with rough dynamical modeling of the three resolved HUDS, suggests that though their H I and optical diameters are similar to $L_\star$ galaxies, they have dynamical masses consistent with the smaller dwarf halos expected given their stellar mass. However, we note that given the poor resolution of the current observations, it is not possible to disentangle possible effects of gas infall and non-standard disk geometry.

6. The combination of large radii and low rotation velocities suggests, under the assumption that the angular momentum of the disk traces the angular momentum of the halo, that these HUDS reside in high spin parameter halos, potentially implying that the high angular momentum of the halos is responsible for their "ultra-diffuse" nature.

Together, these observations suggest that these isolated HUDS are gas-rich, low density, extended dwarfs, in unusual lower mass halos. Therefore they may

be related to gas poor, non-isolated UDGs with similar halo masses. However, further observations and modeling will be required to understand the nature of that connection, and their place in the evolutionary history of very low surface brightness galaxies.

CHAPTER 6

SUMMARY AND CONCLUSIONS

The ALFALFA survey represents a major advance in both volume and resolution of blind H I surveys. These improvements have enabled the work of this thesis, an examination of potential optically "dark" and "almost dark" galaxies, i.e., galaxies that contain significant H I but no, or very few stars. In addition to providing uniform data across an increased search volume, ALFALFA allows for higher accuracy cross identification between H I and optical sources due to its improved resolution – only ~1% of the ~30,000 clearly extragalactic sources detected in ALFALFA do not have a clear stellar counterpart. Most of these H I sources with no detected stellar counterpart in the SDSS are spurious or tidal debris, but a few have ordered gas and very faint or very low surface brightness stellar populations detected in deep follow up imaging. These sources are thus dubbed "almost dark," and are important for understanding when standard star formation laws in galaxies break down.

This thesis studies the H I sources in ALFALFA without identified stellar counterparts in the SDSS and DSS2 surveys in an attempt to find, characterize, and understand these "almost dark" galaxies. In this chapter we present a brief summary of the conclusions from this work before presenting potential future directions for this research in chapter 7.

In chapter 2 we summarize ALFALFA's contribution to studies of H I rich galaxies without detectable stellar counterparts. We describe the challenges associated with identifying optically dark H I sources, including decreased reliability, confusion with other spectral lines, and misidentification due to large pointing errors. We show that dark sources in ALFALFA are located at signif-

icantly smaller nearest neighbor separations than typical ALFALFA galaxies, and that ALFALFA does not detect isolated dark sources: almost all ALFALFA "dark" sources have spectroscopically identified neighbors with projected separations <300 kpc. This suggests that the formation of "dark" H I clouds is tied to their local environment.

We further present results from H I synthesis follow up observations with WSRT and the VLA. These observations imaged some of the best candidate "almost dark" sources across a range of environments, masses, and velocity widths. We demonstrate that most of these "dark" sources appear to have some sort of tidal origin, but that they are not a uniform population. Indeed, they represent a heterogeneous collection of sources with extreme gas fractions, examples of which are given in chapters 3-5.

In chapter 3 we present ALFALFA and WSRT synthesis maps of interesting "dark" systems from a 2x2 Mpc region in the Leo Cloud of galaxies. We report the detection of multiple >300 kpc H I plumes, and an intra-group plume that may extend ~600 kpc. In particular, we show that the plumes in the NGC 3227 and NGC 3190 groups extend well beyond the areas studied in previous synthesis observations, suggesting connections between galaxies on larger scales than previously thought. Further, we show that these H I features without associated stellar counterparts make up a significant fraction of the atomic hydrogen in these groups. Finally, we suggest that the NGC 3190 group and the NGC 3227 group may be part of a larger region experiencing active infall. We emphasize the importance of surveys that cover wide fields at high sensitivity to effectively trace H I plumes at these scales, and in reaching a full understand of the importance of interactions in group environments.

In chapter 4 we present the discovery of one of the most extreme "almost dark" systems detected in ALFALFA. The HI1232+20 system contains three strong ALFALFA sources that are not detected in SDSS and that lack obvious tidal companions. These three sources are all within 70 km s^{-1} and 20′ of each other, but appear to be isolated from other sources of similar redshift (though their distances from recessional velocities are somewhat uncertain due to their projected location ~8 degrees north of the center of the Virgo Cluster). Deep optical imaging with pODI on the WIYN 3.5m at KPNO reveals an ultra-low surface brightness stellar counterpart (peak μ_g= 26.4 mag arcsec^{-2}) to the brightest source in the system, AGC 229385. This very blue stellar population is detected in archival mid-depth GALEX NUV and FUV data, but is not seen in 2MASS or WISE NIR imaging, nor deep WIYN narrow-band Hα imaging. The other ALFALFA sources in the HI1232+20 system show no trace of any optical emission, with upper-limits to their surface brightnesses of 27.8 mag arcsec^{-2}.

WSRT H I synthesis maps of HI1232+20 reveal very high mass, highly spatially extended cold gas distributions. The largest, AGC 229385, is $10^{8.9} M_\odot$ assuming a distance of 25 Mpc. Thus, this galaxy has the largest accurately measured H I mass-to-light ratio of any known (non-tidal) galaxy, $M_{\rm H\,I}/{\rm L}_B$ = 38 $M_\odot/L_\odot$, placing it far off H I -stellar mass scaling relations. Further, the H I velocity fields of the sources appear inconsistent with standard scaling relations like the Baryonic Tully Fisher relation; though the spatial extent and gas mass of AGC 229385 are very large, the velocity field is indicative of rotation at only a very low amplitude of ~10 km s^{-1}. These sources may be examples of objects near star formation thresholds; understanding these enigmatic sources, as well as placing more stringent constraints on their distance, is active future work.

In chapter 5 we extended the concept of "almost dark" to encompass sources with surface brightnesses that are only barely detected in SDSS. We specifically focus on sources with properties similar to recently reported "ultra-diffuse" galaxies (UDGs): galaxies with stellar masses of dwarf galaxies, but radii of $L_\star$ galaxies. While previously reported UDGs tend to be in cluster environments and do not have detected H I, we show that a substantial population of "H I-bearing ultra diffuse" sources (HUDS) exist in isolation in ALFALFA. We find that these isolated HUDS are bluer and have more irregular morphologies than cluster UDGs, and that they appear to be gas rich for their stellar mass, with low star formation efficiencies.

We further present resolved H I imaging of three HUDS originally included in the ALFALFA "darks" sample. We show that their H I extends to radii typical of H I in $L_\star$ galaxies, but that they do not appear to lie far off the H I mass-H I radius scaling relation. We estimate inclinations and dynamical masses for these resolved HUDS assuming well behaved thin disks, and suggest that they have dynamical masses consistent with smaller dwarf halos ($M_{halo} < 10^{11} M_\odot$). We also note that the HUDS have narrower velocity widths when compared to the ALFALFA sample, even after correcting for selection effects. This, coupled with their large radii, suggests that these HUDS may live in high spin parameter halos, a potential explanation for their "ultra-diffuse" nature.

Taken together this work demonstrates the importance of the ALFALFA survey in furthering our understanding of "dark" and "almost dark" galaxies, and thus our understanding of the extremes in star and galaxy formation. It emphasizes the importance of future deep, wide field blind surveys for detecting H I emission otherwise missed in pointed surveys. Further, while it appears that

there is not a substantial population of nearly starless, gas rich galaxies at the detection limits of ALFALFA, there are a few rare "almost dark" galaxies and a substantial number of barely visible very low surface brightness "ultra-diffuse" galaxies that challenge our understanding, and provide an opportunity for advancing our knowledge of galaxy formation for years to come.

CHAPTER 7

FUTURE WORK

While the ALFALFA survey has advanced our understanding of extreme gas rich but star poor "almost dark" galaxies, its contribution brings up as many questions as it answers. Here we briefly outline some of these questions, along with plans to begin to answer them.

7.1 The Nature of HI1232+20

One of the main questions that results from this work is the reason for the exceptionally high gas fractions in the HI1232+20 system. While current observations are sufficient to identify this system as extreme, they are not yet able to distinguish between multiple plausible explanations for its apparent suppression of star formation. It may be that these objects previously existed below detection limits, and have just recently accreted their gas. Or, it may be that these sources are condensing for the first time as recent accretion from the cosmic web, possibly as a condensation infalling into Virgo. It also could be that AGC 229385 is a newly forming TDG from an extreme high speed tidal encounter - its apparent isolation argues against this, but without a well constrained distance, we cannot rule this hypothesis out. Or it could be something else. Thus, without a more detailed characterization of the stellar population, higher resolution H I measurements, and a stellar measurement of the distance, the large amount of gas and lack of stars in this system remains an enigma.

To better answer these questions we have recently obtained high resolution optical imaging with the Hubble Space Telescope (HST) and high resolution (B-

array) VLA imaging of AGC 229385, the largest and most enigmatic source in this system.

With the HST observations we hope to determine the distance to AGC 229385 by resolving its evolved stellar population, and then measuring the brightness of the tip of the red giant branch (TRGB; e.g., Sakai et al., 1997; McQuinn et al., 2014). Under the assumption that AGC 229385 possesses an older population we can to detect the upper portion of the RGB for distances as large as 15-17 Mpc. If the distance to AGC 229385 is much beyond the Virgo Cluster, the RGB will become inaccessible without a large investment of telescope time, but we can still constrain the distance using fitting of model isochrones to the brightest resolved stars to estimate the distance, helping us understand whether AGC 229385 is in front of, behind, or at the distance of the Virgo Cluster. Further, analysis of the resolved stars in AGC 229385 will help us better understand its stellar population and star formation history by comparing to model color magnitude diagrams for different age stellar populations.

With the H I observations we hope to better resolve the H I disk to distinguish between three different potential scenarios: 1) the H I is part of a single, high dispersion, slightly rotating disk; 2) the H I is part of a single halo experiencing significant infall; or 3) the H I is two interacting dwarf galaxies. These high resolution VLA observations should map the H I distribution and the H I velocity field at sufficient resolutions and sensitivities to differentiate between models of these three scenarios. More specifically, we expect high enough resolution to better model the deprojected surface density profile, along with the peak H I column density, and the column density threshold for star formation. Using 3D modeling software like TiRiFiC (Józsa et al., 2007), we will be able to

model the rotational, radial, and turbulent components of the velocity field, and determine which model scenario best fits the data.

Taken together, these observations will better constrain our understanding of this extreme system. Analysis is currently underway, and the results should appear in publications around the end of this year.

7.2 Individual Peculiar Sources

A number of sources in the ALFALFA "darks" sample seem to have peculiar combinations of properties that are poorly understood and worth further study. Here we give a few examples of these sources, and the ongoing work to understand their physical properties and origins.

One particularly interesting but pooly understood system appears to have an H I extent of nearly 80 kpc, and is likely two very large H I sources. The system has a total H I mass of $10^{9.3} M_{\odot}$, however, its total velocity width is only ~48 km s^{-1}, and it is undetected in SDSS imaging. We have obtained deep WIYN imaging of this system where we detect a very faint stellar counterpart, giving a total $M_{\rm H\,I}/{\rm L}_B$ of the system of ~50. We also have obtained high resolution B-array H I imaging, which we have combined with lower resolution WSRT H I imaging. Interpreting this enigmatic sources, and whether it is separate merging sources, or has a tidal origin is current active work.

Another intriguing pair of detections is AGC 229360 and AGC 229361. These sources may be the most isolated candidate "dark" galaxies in ALFALFA, and seem to have somewhat similar properties to the HI1232+20 system. This pair

has two bright H I sources undetected in SDSS at a similar recessional velocity (~1500 km s^{-1}), and at a similar separation from the Virgo cluster. Additionally, WSRT imaging suggests ordered gas dynamics, with a similarly shallow velocity gradient. Yet, like HI1232+20, its signifcant distance uncertainty due to its proximity to the Virgo Cluster limits current interpretation. We have only recently obtained deep WIYN optical imaging of this source, and more analysis is underway.

A third interesting system to explore is AGC 208399. One of the most extreme low surface brightness sources in the ALFALFA sample, it is only barely visible in enhanced SDSS imaging, and was observed as an "almost dark" source by Cannon et al. (2015). In that paper we found that AGC 208399 is very gas rich ($M_{HI}/L_g = 6$; $M_{HI}/L_B = 5$; $M_{HI}/M_\star = 15$), but quiescent ($SFR_{FUV} = 5\times10^{-5}$ $M_\odot$ yr^{-1}). Further, deep archival CFHT imaging reveals a g-i color of 0.7, much redder than other detected "almost dark" galaxies. Thus this source seems to be in a transitional state of star formation. Its H I appears to be ordered, and rotationally supported, but with a very small velocity gradient like other small mass galaxies. Further, it has the smallest recessional velocity of non-tidal "almost" dark sources in ALFALFA, which makes it a prime candidate for detailed study of its stellar populations. Yet this source currently needs deeper and higher resolution H I and optical observations, which we hope to propose for in the future.

We also hope to better explore the potential candidate tidal galaxies in this sample, to determine if they are indeed tidal in origin, and the potential OHMs, to confirm that they are indeed OHMs. By studying these individual sources in detail we hope to, over time, build up a better understanding of the types and

context of the "almost dark" galaxies in the local universe.

7.3 The Role of H I-bearing UDGs in Galaxy Evolution

As discussed in chapter 5, there has been significant debate about the role of UDGs in galactic evolution and their place in a ΛCDM cosmology, and the the ALFALFA "H I-bearing ultra-diffuse" sources (HUDS) may be an important piece to the puzzle. Yet, though HUDS have similarly large radii for their stellar mass, they differ from other UDGs in that they are more gas rich and bluer than other UDGs, with irregular morphologies and knots of apparent star formation (in contrast with the apparently smooth, quiescent stellar distributions of other UDGs). Yet, with the current optical and H I data, the detailed properties of this extreme population, and whether or not the HUDS are in some way connected to quiescent UDGs is still unclear.

Thus, one important question that results from this thesis is: what are the "H I-bearing ultra-diffuse" sources (HUDS), and what is their relationship, if any, to other UDGs? Are they potential progenitors to cluster UDGs caught in a special phase of gas accretion? Or are they a separate population of long lived isolated, stable disks that are unable to efficiently convert their gas into stars? Answering this question will require deep multiwavelength follow up observations of a significant sample of HUDS, and detailed comparison of these observations with simulations and samples of quiescent UDGs. More specifically, approaching this broad question will first require answers to the following pieces (which we discuss in more detail below):

1. What are the properties of the dark matter halos of HUDS?

2. What are the properties and components of their stellar populations?
3. What are the star formation laws in these sources?
4. What are the metal contents of these sources?
5. What environmental factors could influence their evolution?

7.3.1 Dark Matter Halos of H I-bearing UDGs

The first question to answer about HUDS is the question of their halo mass. Are they extended galaxies in small dwarf halos, or are they "failed" galaxies that reside in larger halos? While optical studies of cluster UDGs have been limited to dynamical studies of globular clusters, for H I-bearing UDGs, resolved H I imaging should be able to significantly constrain the masses of the halos. To this end, we hope to use the VLA to obtain low and mid-resolution (D and C configuration) H I imaging of ~10 HUDS, significantly increasing our resolved sample. These observations should give us enough morphological information to determine whether or not the gas is confined to a disk-like distribution, and, if so, to constrain the inclination of the disk. This information combined with rough measurements of the galaxies' velocity fields, can place significant constraints on the halo masses by comparing the observed rotation velocities with those predicted by different dark matter distributions.

While mid-resolution H I imaging will provide sparse rotation curves that constrain the halo masses, high resolution imaging will be necessary to fully model the rotation curve, and distinguish rotational and radial velocities. Thus, we will also propose for high resolution (B-configuration) VLA imaging in a future semester. In addition to improving constraints on the halo models, this

high resolution H I imaging should be able to distinguish between proposed formation mechanisms. For example, Amorisco & Loeb (2016) predict that star forming UDGs are spatially extended because they reside in halos with large angular momentum for their stellar mass, whereas Di Cintio et al. (2017) predict that the spatial extent is the result of gas outflows. High resolution imaging will resolve radial outflows, if they exist, and constrain the disk angular momenta, potentially suggesting a constraint on the halo spin if we assume that the angular momentum of the disk scales with that of the halo. With measurements of the halo properties of a significant sample of H I-bearing UDGs, we will be able to compare the distribution of halo parameters with ongoing work on the halos of cluster UDGs, arguing for or against a potential common origin.

Moreover, one of the more interesting observations about the HUDS is that they appear to have very narrow H I velocity widths. With measurements of the inclination, we will be able to estimate the position of these sources relative to, e.g., the baryonic Tully-Fisher relation, to see if this population indeed falls off the relation.

7.3.2 Stellar Populations of H I-bearing UDGs

Another way to explore the origins of HUDS, and thus their connection to gas-poor UDGs is through multi-band observations of their current stellar populations, coupled with both global and spatially resolved broadband modeling of the spectral energy distribution (SED). To do this I plan to use Indiana University's guaranteed access to the WIYN 3.5m telescope at Kitt Peak National Observatory to obtain deep imaging in several bands of the 13 sources we have

proposed to observe with the VLA.

Moreover, by analyzing the isophotal structure of the H I-bearing UDGs in red and near infrared bands compared with bluer bands we should be able to distinguish between a younger and older stellar population, if they exist (Janowiecki & Salzer, 2014). This analysis should allow us to begin to explore what these galaxies looked like without their star formation, and answer questions like: do these galaxies have an older stellar population? If so, what are its properties? What is its stellar mass? What is its stellar surface density profile? How do these properties relate to cluster UDGs?

7.3.3 Star Formation Law in H I-bearing UDGs

A third way of exploring the evolution of these HUDS is to study their star formation laws in detail. This is important because by modeling the star formation in the source we can extrapolate what the sources would look like in the future in several scenarios, including if they fell into a cluster and were stripped of gas, or if they continued to form stars at a steady rate, or if they have just recently experienced significant gas infall and began to form stars at a dramatically increased rate. We then can compare these model sources with observed properties of UDGs, to determine if it is possible that they are connected.

Understanding the star formation laws in these sources will have three specific observational components. First, I plan to analyze publicly available GALEX FUV and NUV data for these sources to constrain the star formation within the last 100 Myr, and to add additional points to the SED models discussed above. The initial sample of 13 sources we propose to observe with the

VLA all have medium depth GALEX data available. In compelling cases, we may also propose to observe these sources with HST in the UV. Second, I plan to use Indiana's access to both the WIYN 0.9m and 3.5m telescopes at KPNO to observe the sources in Hα. These measurements will constrain the most recent star formation in these sources, and identify any potential H II regions for spectroscopic follow up. Third, I will compare these measurements of the star formation rate in H I-bearing UDGs with the measured gas density distribution in the high resolution VLA data. This comparison will allow us to compare these sources with standard star formation laws, like the Kennicutt-Schmidt relation (e.g. Kennicutt & Evans, 2012). Understanding whether or not these galaxies follow the same star formation law as normal dwarfs or spiral galaxies will be an important constraint on their potential relationship to other "ultra-diffuse" sources.

7.3.4 Metallicities of H I-bearing UDGs

Hα identification of H II regions will also be important for constraining the gas phase metallicity of the galaxies. While SED fitting may provide loose constraints on stellar metallicity, in sources with identified H II regions we will be able to obtain high resolution spectra by, e.g. using collaborator access to the Large Binocular Telescope, and thus constrain the gas metallicity. We also can search for QSOs in the vicinity of the H I-bearing UDGs to observe in the UV with HST to look for absorption from metals in the gas. This analysis will be important in understanding the amount of galactic processing in these extreme sources, and in differentiating between hypotheses for their formation. If the galaxy is experiencing significant infall, we may expect the gas to be pristine,

whereas if it is outflowing after a recent starburst, we may expect a higher metal content.

7.3.5 Environment of H I-bearing UDGs

The ALFALFA HUDS were selected to be isolated: we eliminated all objects that had another source with a measured redshift within 500 km s^{-1} and a projected separation of 350 kpc. While this implies that these sources are central halos that are not interacting with other galaxies, we will want to use the wide field of view of the One Degree Imager on the WIYN 3.5m to look for other low surface brightness or irregular sources that did not get assigned a fiber in the SDSS spectroscopic survey, or are too distant to be included in the Zwicky catalogs. Further, we will likely want to probe sources as a function of both local and large scale environment. This will likely require observing a comparison sample with a less strict local isolation criteria, and sorting the observed sources by large scale structure.

7.4 The Future of "Almost Dark" Galaxies

Astronomy is well positioned to make significant progress on the role of gas in galaxy formation in the coming years. A number of next generation radio arrays equipped to observe gas emission lines are currently, or soon to be, in commissioning. Hydrodynamic simulations which incorporate gas dynamics are beginning to probe physically interesting regimes. Thus, there is an exciting future in continuing to observe and better understand extreme, enigmatic gas

rich sources as clues to better understanding galaxy formation.

The immediate next steps, as outlined above, involve detailed follow up observations of the remaining most interesting "almost dark" galaxy candidates detected in ALFALFA, and placing these sources in context by observing sources at a range of masses and surface brightnesses. However, in the long term ALFALFA will eventually draw to close, and will give way for next generation legacy surveys. These surveys will push to new levels in terms of H I content and optical surface brightness, allowing for a full characterization of the limits of star formation. Through future study of the things that we still cannot see, we will be able to continue to better understand the formation and evolution of galaxies, furthering our understanding of where we came from, and our place in the universe.

APPENDIX A

APPENDIX TO CHAPTER 5

A.1 Comparison of 1D Profiles from SDSS and WIYN Images

Since the sources in the HUDS samples are only barely detected in SDSS, here we explore the reliability of the SDSS measurements by comparing our measured profiles to deeper WIYN imaging. While it is clearly true that these galaxies are very low surface brightness and very extended from visual inspection, this comparison provides a rough test of our quantitative estimates of surface brightness and radius for purposes of sample selection.

Specifically, for both sources with deep WIYN imaging we apply our simple 1D fitting procedure using identical apertures to both the SDSS and WIYN images. Figure A.1 shows the resulting profiles and 1D fits for both sources.

The profiles show g-band data, and cut off the profile fits when the signal drops to 0. For AGC 122966 the fits are almost entirely consistent within

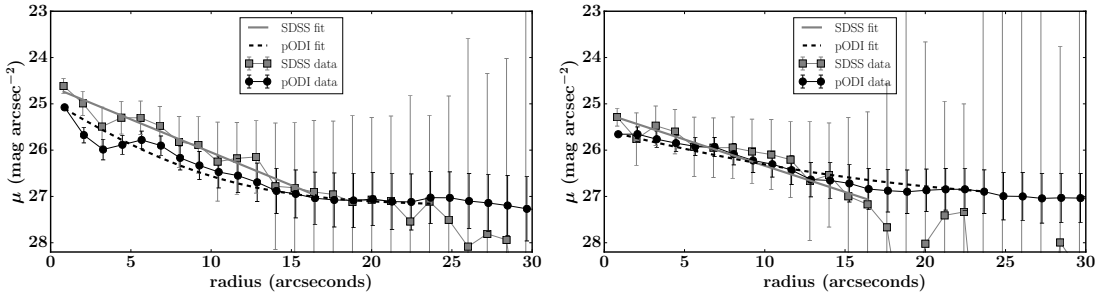

Figure A.1: Comparison of 1D profiles derived from circular apertures on SDSS and deep WIYN images for AGC 334315 (left) and AGC 122966 (right). These profiles demonstrate the rough reliability of the SDSS data for sample selection, and the need for deeper data to obtain detailed structural information about these very low surface brightness, irregular sources.

the errors. For AGC 334315 the SDSS data is systematically offset to brighter values than the ODI data. This is because AGC 334315 is very close to a bright star, which significantly affects its flux measurement, and creates significant uncertainty in measurements of the local background. This, combined with AGC 334315's relatively low surface brightness makes it a "worst case" scenario, but even in this case the measurements are reasonably consistent. For AGC 334315 (122966) we find a central surface brightness of 24.6+/-0.2 (25.2+/-0.2) mag arcsec^{-2} using the SDSS image, and 24.8+/-0.1 (25.5+/-0.1) mag arcsec^{-2} using the WIYN image. We derive effective radii if 7.6+/-2.1 (9.6+/-4.2) kpc from SDSS, and 4.6+/-0.6 (9.9+/-2.1) kpc from WIYN. This agreement seems especially good given the irregularity morphology of the stellar disks and uncertainties in the background subtraction.

Still, we emphasize that the main point of this paper is not an in depth study of the detailed structural parameters of these sources - the SDSS data are insufficient for this purpose. Thus, these profiles are not intended to provide detailed structural information, but rather to show the rough reliability of the data for purposes of sample selection, and also to qualitatively demonstrate our uncertainties.

A.2 Table 5.1

This section contains the full version of Table 5.1, which is also published in a machine readable version in Leisman et al. (2017).

Table A.1: Properties of HUDS

AGC ID	OC RA J2000	OC Dec J2000	cz km s^{-1}	W_{50} km s^{-1}	$\int S\,dV$ Jy-km s^{-1}	Dist[a] Mpc	log(M_{HI}) log $M_\odot$	$\mu_{g,0}$ mags/$''^2$	r_e kpc	M_g mag	g-r mag	Sample[b]
(1)	(2)	(3)	(4)	(5)	(6)	(7)	(8)	(9)	(10)	(11)	(12)	(13)
322019	344.6121	1.8497	4819	33±14	0.54±0.07	72	8.81±0.08	24.62±0.18	3.9±1.0	-15.8±0.7	0.36±0.25	R
103796	5.1650	6.9658	5647	31±7	0.48±0.04	80	8.86±0.06	24.23±0.14	3.9±0.7	-16.2±0.5	0.47±0.21	R
113790	18.2587	27.6369	4952	31±10	0.33±0.03	69	8.57±0.07	24.31±0.14	2.9±0.6	-15.4±0.5	0.42±0.19	R
114905	21.3271	7.3603	5435	27±3	0.96±0.04	76	9.11±0.06	24.85±0.19	5.1±1.5	-16.2±0.8	0.53±0.25	R
114943	26.7775	7.3311	8416	32±7	0.40±0.04	116	9.10±0.06	24.48±0.18	4.8±1.2	-16.4±0.7	0.36±0.28	R
113949	27.4108	30.6808	7380	44±7	0.44±0.05	102	9.03±0.07	24.29±0.18	3.4±0.8	-15.8±0.7	0.53±0.28	R
122966	32.3708	31.8528	6518	35±6	0.53±0.04	90	9.00±0.06	25.37±0.23	7.4±3.3	-16.4±1.1	0.38±0.41	R
749376	119.5371	25.8306	4743	33±7	0.41±0.04	69	8.66±0.08	24.25±0.18	2.3±0.5	-15.0±0.6	0.64±0.24	R
749290	139.0046	26.6497	6510	39±12	0.40±0.04	97	8.95±0.06	24.12±0.16	3.3±0.7	-16.0±0.6	-0.01±0.24	R
198452	139.1729	6.4353	5619	63±21	0.56±0.05	83	8.96±0.06	24.30±0.14	4.7±0.8	-16.5±0.5	0.20±0.20	R
749401	141.0862	25.6611	2750	75±3	1.71±0.05	41	8.84±0.11	24.44±0.13	4.0±0.9	-16.0±0.5	0.29±0.19	R
198596	147.0300	16.2606	3797	48±5	0.62±0.04	57	8.68±0.08	24.80±0.17	5.8±1.8	-16.5±0.8	0.28±0.25	R
193841	149.1125	10.9056	5421	51±5	0.58±0.05	80	8.94±0.07	25.15±0.22	4.5±1.7	-15.6±0.9	0.68±0.31	R
208769	162.4729	21.6383	5930	57±12	0.57±0.04	89	9.03±0.06	24.68±0.17	4.3±1.1	-16.0±0.7	0.67±0.26	R
238764	204.9062	6.9961	7001	38±8	0.46±0.04	104	9.07±0.06	24.57±0.17	4.3±1.1	-16.1±0.7	0.02±0.34	R
232008	209.4404	7.8356	4394	30±3	1.10±0.04	65	9.04±0.07	24.40±0.15	5.1±1.1	-16.6±0.6	0.25±0.21	R
249428	217.7967	0.9519	4070	40±5	0.63±0.05	60	8.72±0.08	24.22±0.33	2.9±0.6	-15.6±0.6	0.30±1.92	R
242019	218.4717	1.4850	1830	71±5	3.42±0.07	29	8.83±0.15	24.27±0.14	3.3±0.9	-15.8±0.7	0.26±0.20	R
749488	223.3033	25.2986	4151	45±7	0.46±0.04	63	8.63±0.08	24.16±0.17	2.3±0.5	-15.1±0.6	0.16±0.23	R
258471	230.6613	5.8292	1796	24±4	0.44±0.03	29	7.94±0.15	25.05±0.23	2.0±0.8	-13.9±1.0	-0.00±0.32	R
257918	233.6442	16.0086	4191	36±8	0.37±0.04	63	8.54±0.08	24.53±0.18	2.6±0.7	-15.0±0.7	0.39±0.25	R
253920	237.9925	11.4175	4673	21±8	0.32±0.03	70	8.57±0.07	24.57±0.17	3.0±0.7	-15.3±0.6	0.33±0.22	R
749352	238.0942	26.4997	6480	38±6	0.66±0.04	94	9.14±0.05	24.51±0.14	5.0±1.0	-16.5±0.5	0.28±0.20	R
268200	243.1867	5.7678	5593	59±6	0.60±0.05	83	8.98±0.06	24.26±0.19	2.3±0.6	-15.0±0.7	0.36±0.32	R
749366	245.8188	25.8453	4314	34±8	0.36±0.04	66	8.57±0.08	24.68±0.20	2.1±0.7	-14.4±0.8	0.75±0.27	R
111947	27.5037	28.9150	3844	37±2	1.12±0.05	52	8.86±0.08	24.30±0.14	4.5±0.9	-16.4±0.6	0.40±0.20	R
121790	42.2837	1.9650	2935	60±4	2.65±0.07	40	9.00±0.11	24.29±0.13	4.7±1.0	-16.5±0.5	0.78±0.18	R

219533	174.9867	16.7214	6381	77±18	0.76±0.06	96	9.22±0.06	24.22±0.18	3.7±0.8	-16.1±0.6	0.04±0.27	R
103435	3.8383	1.0750	2048	24±2	0.99±0.05	28	8.28±0.15	24.12±0.15	1.7±0.4	-14.5±0.6	0.04±0.21	R
334315	350.0492	22.4019	5102	44±3	1.12±0.04	73	9.15±0.06	24.60±0.18	4.2±1.1	-16.0±0.7	0.16±0.28	R
310858	327.6679	28.5908	3476	28±6	0.39±0.03	53	8.41±0.09	24.14±0.15	2.2±0.4	-15.1±0.5	0.29±0.30	B
748702	334.6958	15.7000	7941	72±4	0.87±0.05	108	9.38±0.05	24.40±1.57	5.4±1.2	-16.7±0.7	0.48±14.82	B
321215	337.3817	26.9714	4231	70±7	0.84±0.05	62	8.89±0.07	23.75±0.13	2.6±0.4	-15.8±0.4	0.37±0.19	B
322320	341.4121	7.6647	7615	61±3	1.25±0.06	104	9.50±0.05	24.05±0.14	3.7±0.6	-16.3±0.5	0.51±0.20	B
321442	343.4109	31.9961	3932	57±11	0.57±0.05	57	8.65±0.08	23.45±0.12	1.6±0.2	-15.1±0.4	0.26±0.18	B
333357	345.9771	30.5169	6949	27±4	0.43±0.03	94	8.96±0.05	24.07±0.14	3.5±0.6	-16.1±0.5	0.48±0.21	B
748738	346.2167	14.0181	3896	27±4	0.54±0.04	56	8.61±0.08	24.17±0.15	1.9±0.4	-14.7±0.5	0.55±0.20	B
333366	348.1284	29.8778	7108	186±14	0.91±0.07	97	9.30±0.06	23.57±0.13	2.4±0.3	-15.8±0.4	0.21±0.19	B
333375	349.4354	30.6125	6213	35±5	0.37±0.03	89	8.84±0.06	24.04±0.14	4.7±0.8	-16.8±0.5	0.61±0.20	B
333549	353.1429	29.6678	3813	32±3	0.86±0.05	55	8.78±0.08	23.64±0.12	2.4±0.3	-15.7±0.4	0.43±0.18	B
333298	353.9842	25.3094	5059	31±14	0.44±0.04	72	8.73±0.07	24.64±0.15	5.7±1.3	-16.6±0.6	0.89±0.20	B
333410	354.3000	31.4550	4754	23±11	0.74±0.04	68	8.91±0.07	23.99±0.12	2.3±0.4	-15.3±0.4	0.09±0.18	B
333214	357.9079	27.4694	2836	20±2	0.52±0.03	40	8.30±0.11	23.91±0.13	1.9±0.4	-15.0±0.5	0.33±0.20	B
332328	359.6246	30.6717	4801	74±6	0.61±0.05	68	8.82±0.07	24.16±0.12	4.4±0.6	-16.5±0.4	0.47±0.17	B
103797	6.0308	5.9417	7242	94±39	0.79±0.09	98	9.26±0.07	23.84±0.14	3.2±0.5	-16.2±0.5	0.44±0.21	B
748801	15.2196	16.0825	4369	104±2	1.43±0.06	60	9.09±0.07	23.55±0.13	3.3±0.5	-16.5±0.4	0.47±0.18	B
114882	18.3563	6.3439	7811	141±33	1.03±0.07	107	9.44±0.05	24.11±0.16	2.8±0.6	-15.6±0.6	-0.14±0.27	B
748816	21.9867	14.5019	6407	77±6	1.41±0.06	87	9.40±0.05	24.52±0.15	6.8±1.5	-17.1±0.6	0.68±0.21	B
122791	30.8700	26.6972	4951	71±7	0.56±0.05	69	8.80±0.07	24.20±0.14	3.6±0.6	-16.0±0.5	0.43±0.20	B
123953	44.0146	1.9697	5267	39±9	0.72±0.06	73	8.96±0.07	23.60±0.13	2.0±0.3	-15.3±0.4	0.44±0.20	B
749251	113.7513	26.6589	7261	37±10	0.41±0.04	106	9.04±0.06	24.06±0.14	3.3±0.6	-16.0±0.5	0.29±0.24	B
174593	115.6325	10.3214	4834	52±15	0.58±0.05	71	8.84±0.07	23.75±0.18	3.5±0.5	-16.5±0.4	0.61±0.42	B
188768	127.1575	14.9731	5864	40±17	0.36±0.04	87	8.81±0.07	24.07±0.15	3.3±0.6	-16.0±0.5	0.33±0.22	B
189096	131.7650	0.1667	3964	63±5	0.93±0.07	60	8.90±0.08	23.43±0.12	2.4±0.3	-16.0±0.4	0.42±0.18	B
189167	133.5454	28.9678	3945	32±7	0.40±0.04	58	8.50±0.09	23.81±0.15	2.2±0.4	-15.3±0.5	0.23±0.20	B
182467	134.2733	9.1183	3970	34±8	0.55±0.05	60	8.66±0.08	23.61±0.12	2.4±0.3	-15.8±0.4	-0.04±0.18	B
198563	138.6675	28.5108	6413	83±13	0.70±0.06	95	9.18±0.06	24.07±0.16	2.8±0.6	-15.6±0.6	0.39±0.25	B
193800	139.4371	10.5044	5191	98±18	0.72±0.06	77	9.00±0.07	23.73±0.14	2.2±0.3	-15.5±0.4	0.35±0.20	B
198540	141.3079	3.3131	4209	36±3	1.41±0.05	63	9.13±0.07	23.53±0.12	2.5±0.3	-15.9±0.4	0.40±0.18	B

193798	149.8658	16.0078	4175	62±5	0.97±0.06	62	8.95±0.07	24.01±0.17	2.0±0.4	-15.0±0.6	0.19±0.25	B
205072	150.6617	12.1558	2965	26±6	0.36±0.04	45	8.24±0.11	23.74±0.13	2.0±0.3	-15.3±0.4	0.41±0.19	B
208764	156.8192	20.2153	7195	35±4	0.39±0.03	107	9.03±0.05	23.20±0.13	2.2±0.3	-16.1±0.4	0.21±0.19	B
749425	166.6633	24.0336	5689	96±9	0.65±0.06	86	9.05±0.06	23.55±0.15	1.7±0.3	-15.1±0.5	0.03±0.23	B
215277	168.0308	12.6333	3257	68±7	0.70±0.04	49	8.60±0.09	24.06±0.15	1.8±0.4	-14.7±0.5	0.35±0.20	B
749196	169.0579	27.1806	3970	62±10	0.64±0.05	59	8.72±0.08	23.43±0.12	2.4±0.3	-16.0±0.3	0.38±0.17	B
219672	172.8821	21.5411	6483	97±7	0.70±0.06	97	9.19±0.06	23.46±0.13	2.6±0.4	-16.1±0.4	0.05±0.19	B
219150	174.9175	19.5889	7378	55±10	0.63±0.04	98	9.15±0.05	24.83±0.17	8.0±2.2	-17.1±0.7	0.25±0.25	B
215141	176.1904	11.8156	6010	59±5	0.57±0.04	91	9.04±0.06	23.95±0.15	4.4±0.7	-16.8±0.5	-0.03±0.21	B
219493	177.6429	29.6589	5775	73±8	0.52±0.05	87	8.96±0.07	23.49±0.13	2.7±0.3	-16.1±0.4	0.39±0.18	B
227957	185.7329	6.1553	5303	55±16	0.59±0.06	78	8.92±0.07	23.28±0.12	1.9±0.2	-15.6±0.4	0.04±0.19	B
223760	187.5667	13.3075	4431	108±25	1.30±0.10	66	9.12±0.07	23.79±0.14	1.8±0.3	-14.9±0.5	0.52±0.20	B
229110	191.5362	28.7508	7539	57±8	0.42±0.04	112	9.09±0.06	23.88±0.16	3.4±0.6	-16.3±0.6	0.24±0.23	B
227878	192.3900	9.1033	7327	48±12	0.36±0.04	109	9.01±0.06	23.76±0.15	2.8±0.5	-16.0±0.5	-0.02±0.22	B
233778	196.1425	10.5294	7245	72±5	1.10±0.06	108	9.48±0.05	23.90±0.14	5.1±0.7	-17.1±0.4	0.47±0.19	B
233610	197.0713	11.8061	7515	71±20	0.75±0.05	112	9.34±0.05	23.25±0.12	3.8±0.4	-17.1±0.3	0.19±0.17	B
238692	201.6542	5.7436	7493	83±9	0.60±0.06	111	9.24±0.06	23.38±0.15	2.4±0.3	-16.0±0.5	0.35±0.21	B
239040	203.4829	28.1706	7784	73±7	0.44±0.04	115	9.14±0.05	23.96±0.14	4.4±0.7	-16.7±0.4	0.33±0.19	B
233836	206.7983	8.0022	6993	71±11	0.63±0.05	104	9.20±0.05	23.52±0.13	3.3±0.4	-16.6±0.4	0.29±0.19	B
239133	206.8904	20.4478	8133	51±7	0.43±0.04	120	9.16±0.05	23.95±0.13	5.2±0.7	-17.1±0.4	0.37±0.19	B
239062	207.0492	16.4233	7982	83±6	0.77±0.06	118	9.40±0.05	24.95±0.23	7.5±2.4	-16.9±0.8	0.48±0.53	B
238636	208.4754	9.5044	4872	45±5	0.66±0.05	72	8.90±0.07	23.27±0.14	1.8±0.2	-15.4±0.4	0.14±0.23	B
243835	210.5338	11.1175	6036	58±4	0.88±0.05	90	9.22±0.05	24.35±0.15	5.8±1.1	-16.9±0.6	0.70±0.21	B
249569	213.7571	21.1975	4665	28±7	0.50±0.04	70	8.76±0.07	23.57±0.13	2.3±0.3	-15.7±0.4	0.45±0.19	B
248937	216.4779	12.9189	8041	40±5	0.61±0.05	118	9.30±0.05	23.81±0.14	3.9±0.6	-16.6±0.4	0.26±0.20	B
248981	220.5275	12.4928	5691	66±6	0.54±0.05	84	8.95±0.07	23.80±0.14	2.4±0.4	-15.6±0.5	0.34±0.20	B
249542	224.9542	19.3833	6454	65±4	1.05±0.06	95	9.35±0.05	24.01±0.13	3.7±0.6	-16.3±0.4	0.11±0.20	B
749343	226.9908	25.8253	6606	38±11	0.61±0.05	96	9.13±0.06	23.57±0.13	3.3±0.4	-16.5±0.4	0.41±0.18	B
258576	238.3838	0.3947	5414	118±5	1.42±0.08	79	9.32±0.06	23.73±0.14	3.0±0.4	-16.1±0.4	0.42±0.20	B
749368	248.1012	25.8003	4188	51±3	1.30±0.06	65	9.11±0.07	23.70±0.14	2.2±0.3	-15.5±0.4	0.07±0.19	B
748765	350.9312	14.4278	3472	32±3	0.72±0.04	50	8.63±0.09	23.62±0.12	2.0±0.3	-15.4±0.4	0.54±0.18	B
102907	4.4429	28.7494	6300	87±5	1.05±0.06	89	9.30±0.05	23.43±0.12	3.2±0.3	-16.6±0.3	0.30±0.18	B

102791	10.2404	31.9064	5370	97±4	1.42±0.05	75	9.28±0.06	23.86±0.13	3.4±0.5	-16.3±0.4	0.24±0.19	B
103857	14.8067	6.2733	4589	120±18	0.88±0.08	64	8.93±0.08	23.77±0.14	3.0±0.5	-16.1±0.5	0.35±0.19	B
114607	29.5296	0.8781	5753	28±14	0.54±0.06	80	8.91±0.07	23.84±0.13	2.8±0.4	-15.9±0.4	0.40±0.18	B
123863	35.3867	23.1983	5217	45±6	0.48±0.04	72	8.77±0.07	23.84±0.12	2.0±0.3	-15.2±0.4	0.57±0.17	B
749388	128.2971	24.5719	5409	56±7	0.45±0.05	79	8.82±0.07	23.59±0.12	3.0±0.4	-16.2±0.3	0.52±0.18	B
749279	128.7841	26.8819	7301	69±11	0.49±0.05	108	9.13±0.06	23.38±0.15	1.8±0.3	-15.4±0.5	-0.06±0.23	B
193833	145.0550	9.9253	3381	44±3	0.73±0.03	51	8.66±0.09	23.51±0.12	2.1±0.3	-15.6±0.4	0.20±0.17	B
208759	157.2821	20.2467	3928	19±3	0.38±0.02	59	8.49±0.08	23.62±0.13	1.7±0.3	-15.0±0.4	-0.08±0.20	B
215283	168.8267	12.8986	6015	109±3	0.81±0.05	91	9.20±0.05	23.62±0.13	3.2±0.4	-16.3±0.4	0.40±0.19	B
219487	174.4367	28.1958	5539	41±4	0.51±0.03	81	8.90±0.06	23.67±30.38	4.4±0.6	-17.0±0.4	0.54±77.91	B
219247	177.7763	7.4000	5552	215±6	1.12±0.08	81	9.24±0.06	23.28±0.12	2.4±0.3	-16.1±0.3	0.33±0.17	B
215218	179.5650	15.9256	6806	59±8	0.46±0.04	102	9.05±0.06	23.80±0.15	2.4±0.4	-15.6±0.5	0.50±0.21	B
229376	181.5129	20.9033	2996	45±7	0.52±0.05	46	8.40±0.11	23.59±0.13	2.1±0.3	-15.5±0.4	0.21±0.18	B
223555	186.1067	7.1314	4220	80±8	0.76±0.06	62	8.84±0.08	23.75±0.13	3.1±0.5	-16.2±0.4	0.52±0.18	B
226136	188.1025	10.4844	7249	60±7	0.71±0.05	108	9.29±0.05	23.18±0.13	3.2±0.3	-16.8±0.4	0.11±0.19	B
226721	193.6354	1.1086	2921	68±13	1.14±0.06	44	8.71±0.10	23.43±0.11	2.3±0.3	-15.8±0.3	0.30±0.17	B
238961	206.3763	1.2556	4650	35±7	0.74±0.05	68	8.90±0.07	23.64±0.13	2.5±0.4	-15.8±0.4	0.29±0.18	B
238984	208.5000	3.2319	7215	95±9	0.67±0.06	107	9.26±0.06	23.60±0.13	4.3±0.5	-17.1±0.4	0.42±0.18	B
248887	212.3000	13.3147	4703	43±8	0.41±0.04	70	8.67±0.08	23.26±0.12	1.8±0.2	-15.5±0.4	0.22±0.18	B
749329	212.9921	27.4928	5325	76±7	0.58±0.05	79	8.93±0.07	24.07±0.16	2.5±0.5	-15.4±0.6	0.30±0.22	B
248945	221.7479	13.1697	5680	70±8	0.62±0.05	84	9.01±0.06	23.97±0.16	2.9±0.5	-15.8±0.5	0.46±0.22	B
258600	239.0038	3.6183	7627	45±12	0.77±0.06	111	9.35±0.05	24.05±0.15	3.9±0.7	-16.3±0.5	0.69±0.21	B
223471	185.3538	9.6208	6375	126±7	0.64±0.05	96	9.14±0.06	23.89±0.14	3.7±0.6	-16.4±0.4	0.38±0.19	B
253921	237.7179	11.2175	4636	109±59	0.86±0.06	69	8.99±0.07	24.13±0.14	4.5±0.7	-16.6±0.5	0.61±0.19	B

Notes: H I and optical table parameters come from ALFALFA and SDSS, and are described in sections 5.3.1 and 5.3.2 of the text respectively. [a]: Distances from the ALFALFA flow model (see Haynes et al., 2011); distance depended quantities include an error of 5 Mpc due to peculiar velocities [b]: R = HUGS-R, B= HUGS-B

BIBLIOGRAPHY

Abraham, R. G., & van Dokkum, P. G. 2014, PASP, 126, 55

Adams, E. A. K., Giovanelli, R., & Haynes, M. P. 2013, ApJ, 768, 77

Ahn, C. P., Alexandroff, R., Allende Prieto, C., et al. 2012, ApJS, 203, 21

Alam, S., Albareti, F. D., Allende Prieto, C., et al. 2015, ApJS, 219, 12

Amanullah, R., Lidman, C., Rubin, D., et al. 2010, ApJ, 716, 712

Amorisco, N. C., & Loeb, A. 2016, MNRAS, 459, L51

Amorisco, N. C., Monachesi, A., & White, S. D. M. 2016, ArXiv e-prints, arXiv:1610.01595

Appleton, P. N., Mundell, C., Bitsakis, T., et al. 2014, ApJ, 797, 117

Astropy Collaboration, Robitaille, T. P., Tollerud, E. J., et al. 2013, A&A, 558, A33

Barnes, D. G., Staveley-Smith, L., de Blok, W. J. G., et al. 2001, MNRAS, 322, 486

Baushev, A. N. 2016, ArXiv e-prints, arXiv:1608.04356

Beasley, M. A., Romanowsky, A. J., Pota, V., et al. 2016, ApJ, 819, L20

Beasley, M. A., & Trujillo, I. 2016, ApJ, 830, 23

Begum, A., Chengalur, J. N., & Karachentsev, I. D. 2005, A&A, 433, L1

Beijersbergen, M., de Blok, W. J. G., & van der Hulst, J. M. 1999, A&A, 351, 903

Bekki, K., & Couch, W. J. 2011, MNRAS, 415, 1783

Bellazzini, M., Magrini, L., Mucciarelli, A., et al. 2015, ApJ, 800, L15

Benítez-Llambay, A., Navarro, J. F., Frenk, C. S., et al. 2017, MNRAS, 465, 3913

Bernstein-Cooper, E. Z., Cannon, J. M., Elson, E. C., et al. 2014, AJ, 148, 35

Bianchi, L., Conti, A., & Shiao, B. 2014, Advances in Space Research, 53, 900

Binggeli, B., Sandage, A., & Tammann, G. A. 1985, AJ, 90, 1681

Blakeslee, J. P., Lucey, J. R., Barris, B. J., Hudson, M. J., & Tonry, J. L. 2001, MNRAS, 327, 1004

Blanton, M. R., Kazin, E., Muna, D., Weaver, B. A., & Price-Whelan, A. 2011, AJ, 142, 31

Borthakur, S., Yun, M. S., & Verdes-Montenegro, L. 2010, ApJ, 710, 385

Borthakur, S., Yun, M. S., Verdes-Montenegro, L., et al. 2015, ApJ, 812, 78

Bothun, G. D., Impey, C. D., Malin, D. F., & Mould, J. R. 1987, AJ, 94, 23

Bothun, G. D., Schombert, J. M., Impey, C. D., & Schneider, S. E. 1990, ApJ, 360, 427

Bournaud, F., & Duc, P.-A. 2006, A&A, 456, 481

Bressan, A., Marigo, P., Girardi, L., et al. 2012, MNRAS, 427, 127

Briggs, F. H. 1998, A&A, 336, 815

Brinchmann, J., Charlot, S., White, S. D. M., et al. 2004, MNRAS, 351, 1151

Broeils, A. H., & Rhee, M.-H. 1997, A&A, 324, 877

Burkert, A. 2017, ApJ, 838, 93

Cannon, J. M., Giovanelli, R., Haynes, M. P., et al. 2011, ApJ, 739, L22

Cannon, J. M., Martinkus, C. P., Leisman, L., et al. 2015, AJ, 149, 72

Chengalur, J. N., Giovanelli, R., & Haynes, M. P. 1995, AJ, 109, 2415

Cornwell, T. J. 2008, IEEE Journal of Selected Topics in Signal Processing, 2, 793

Crain, R. A., Bahé, Y. M., Lagos, C. d. P., et al. 2017, MNRAS, 464, 4204

Dabringhausen, J., & Kroupa, P. 2013, MNRAS, 429, 1858

Darling, J., & Giovanelli, R. 2002, AJ, 124, 100

de Blok, W. J. G., & Walter, F. 2000, in Astronomical Society of the Pacific Conference Series, Vol. 218, Mapping the Hidden Universe: The Universe behind the Mily Way - The Universe in HI, ed. R. C. Kraan-Korteweg, P. A. Henning, & H. Andernach, 357

Di Cintio, A., Brook, C. B., Dutton, A. A., et al. 2017, MNRAS, 466, L1

Disney, M., & Phillipps, S. 1983, MNRAS, 205, 1253

Disney, M. J. 1976, Nature, 263, 573

Disney, M. J., & Lang, R. H. 2012, MNRAS, 426, 1731

Doi, M., Tanaka, M., Fukugita, M., et al. 2010, AJ, 139, 1628

Doyle, M. T., Drinkwater, M. J., Rohde, D. J., et al. 2005, MNRAS, 361, 34

Du, W., Wu, H., Lam, M. I., et al. 2015, AJ, 149, 199

Duc, P.-A. 2012, Astrophysics and Space Science Proceedings, 28, 305

Duc, P.-A., & Bournaud, F. 2008, ApJ, 673, 787

Duc, P.-A., Paudel, S., McDermid, R. M., et al. 2014, MNRAS, 440, 1458

Dutton, A. A., van den Bosch, F. C., Dekel, A., & Courteau, S. 2007, ApJ, 654, 27

Elmegreen, B. G. 2015, ApJ, 814, L30

Elmegreen, B. G., & Hunter, D. A. 2016, ArXiv e-prints, arXiv:1612.05615

Falco, E. E., Kurtz, M. J., Geller, M. J., et al. 1999, PASP, 111, 438

Ferrarese, L., Côté, P., Cuillandre, J.-C., et al. 2012, ApJS, 200, 4

Garcia, A. M. 1993, A&AS, 100, 47

Geha, M., Blanton, M. R., Masjedi, M., & West, A. A. 2006, ApJ, 653, 240

Geller, M. J., & Huchra, J. P. 1983, ApJS, 52, 61

Giovanelli, R., & Haynes, M. P. 1989, ApJ, 346, L5

—. 2016, A&A Rev., 24, 1

Giovanelli, R., Haynes, M. P., da Costa, L. N., et al. 1997a, ApJ, 477, L1

Giovanelli, R., Haynes, M. P., Herter, T., et al. 1997b, AJ, 113, 53

—. 1997c, AJ, 113, 22

Giovanelli, R., Haynes, M. P., Kent, B. R., & Adams, E. A. K. 2010, ApJ, 708, L22

Giovanelli, R., Haynes, M. P., Kent, B. R., et al. 2005, AJ, 130, 2598

Giovanelli, R., Haynes, M. P., Adams, E. A. K., et al. 2013, AJ, 146, 15

Gopu, A., Hayashi, S., Young, M. D., et al. 2014, in Proc. SPIE, Vol. 9152, Software and Cyberinfrastructure for Astronomy III, 91520E

Gratier, P., Braine, J., Rodriguez-Fernandez, N. J., et al. 2010, A&A, 522, A3

Gunn, J. E., Carr, M., Rockosi, C., et al. 1998, AJ, 116, 3040

Hallenbeck, G., Huang, S., Spekkens, K., et al. 2014, AJ, 148, 69

Hao, C.-N., Kennicutt, R. C., Johnson, B. D., et al. 2011, ApJ, 741, 124

Haynes, M. P. 1979, AJ, 84, 1830

—. 1981, AJ, 86, 1126

Haynes, M. P., Giovanelli, R., & Chincarini, G. L. 1984, ARA&A, 22, 445

Haynes, M. P., Giovanelli, R., & Kent, B. R. 2007, ApJ, 665, L19

Haynes, M. P., Giovanelli, R., Martin, A. M., et al. 2011, AJ, 142, 170

Heisler, J., Tremaine, S., & Bahcall, J. N. 1985, ApJ, 298, 8

Hernandez, X., Park, C., Cervantes-Sodi, B., & Choi, Y.-Y. 2007, MNRAS, 375, 163

Hess, K. M., Cluver, M. E., Yahya, S., et al. 2017, MNRAS, 464, 957

Hess, K. M., & Wilcots, E. M. 2013, AJ, 146, 124

Hibbard, J. E., van der Hulst, J. M., Barnes, J. E., & Rich, R. M. 2001a, AJ, 122, 2969

Hibbard, J. E., van Gorkom, J. H., Rupen, M. P., & Schiminovich, D. 2001b, in Astronomical Society of the Pacific Conference Series, Vol. 240, Gas and Galaxy Evolution, ed. J. E. Hibbard, M. Rupen, & J. H. van Gorkom, 657

Hopkins, A. M., & Beacom, J. F. 2006, ApJ, 651, 142

Huang, S., Haynes, M. P., Giovanelli, R., & Brinchmann, J. 2012a, ApJ, 756, 113

Huang, S., Haynes, M. P., Giovanelli, R., et al. 2012b, AJ, 143, 133

Huchra, J. P., & Geller, M. J. 1982, ApJ, 257, 423

Hunter, D. A., & Elmegreen, B. G. 2006, ApJS, 162, 49

Hunter, D. A., Elmegreen, B. G., Rubin, V. C., et al. 2013, AJ, 146, 92

Impey, C., Bothun, G., & Malin, D. 1988, ApJ, 330, 634

Impey, C. D., Sprayberry, D., Irwin, M. J., & Bothun, G. D. 1996, ApJS, 105, 209

Janesh, W., Rhode, K. L., Salzer, J. J., et al. 2017, ApJ, 837, L16

—. 2015, ApJ, 811, 35

Janowiecki, S., & Salzer, J. J. 2014, ApJ, 793, 109

Janowiecki, S., Leisman, L., Józsa, G., et al. 2015, ApJ, 801, 96

Jester, S., Schneider, D. P., Richards, G. T., et al. 2005, AJ, 130, 873

Jones, M. G., Papastergis, E., Haynes, M. P., & Giovanelli, R. 2016, MNRAS, arXiv:1510.07050

Józsa, G. I. G., Kenn, F., Klein, U., & Oosterloo, T. A. 2007, A&A, 468, 731

Karachentsev, I. D., & Nasonova, O. G. 2010, MNRAS, 405, 1075

Karachentsev, I. D., Nasonova, O. G., & Courtois, H. M. 2011, ApJ, 743, 123

Karachentsev, I. D., Nasonova, O. G., & Karachentseva, V. E. 2015a, Astrophysical Bulletin, 70, 1

Karachentsev, I. D., Tully, R. B., Makarova, L. N., Makarov, D. I., & Rizzi, L. 2015b, ApJ, 805, 144

Karachentsev, I. D., Tully, R. B., Wu, P.-F., Shaya, E. J., & Dolphin, A. E. 2014, ApJ, 782, 4

Kennicutt, R. C., & Evans, N. J. 2012, ARA&A, 50, 531

Kennicutt, Jr., R. C. 1998, ApJ, 498, 541

Kent, B. R. 2010, ApJ, 725, 2333

Kent, B. R., Spekkens, K., Giovanelli, R., et al. 2009, ApJ, 691, 1595

Kent, B. R., Giovanelli, R., Haynes, M. P., et al. 2007, ApJ, 665, L15

Kim, S., Staveley-Smith, L., Dopita, M. A., et al. 1998, ApJ, 503, 674

Koda, J., Yagi, M., Yamanoi, H., & Komiyama, Y. 2015, ApJ, 807, L2

Koopmann, R. A., Giovanelli, R., Haynes, M. P., et al. 2008, ApJ, 682, L85

Kotulla, R. 2014, in Astronomical Society of the Pacific Conference Series, Vol. 485, Astronomical Data Analysis Software and Systems XXIII, ed. N. Manset & P. Forshay, 375

Krumholz, M. R. 2013, MNRAS, 436, 2747

—. 2015, ArXiv e-prints, arXiv:1511.03457

Lee, H., McCall, M. L., Kingsburgh, R. L., Ross, R., & Stevenson, C. C. 2003, AJ, 125, 146

Lee-Waddell, K., Spekkens, K., Haynes, M. P., et al. 2012, MNRAS, 427, 2314

Lee-Waddell, K., Spekkens, K., Cuillandre, J.-C., et al. 2014, MNRAS, 443, 3601

Lee-Waddell, K., Spekkens, K., Chandra, P., et al. 2016, MNRAS, 460, 2945

Leisman, L., Haynes, M. P., Giovanelli, R., et al. 2016, MNRAS, 463, 1692

Leisman, L., Haynes, M. P., Janowiecki, S., et al. 2017, ApJ, 842, 133

Lelli, F., Fraternali, F., & Sancisi, R. 2010, A&A, 516, A11

Lelli, F., Duc, P.-A., Brinks, E., et al. 2015, A&A, 584, A113

Leroy, A. K., Walter, F., Brinks, E., et al. 2008, AJ, 136, 2782

Lucy, L. B. 1974, AJ, 79, 745

Madau, P., Pozzetti, L., & Dickinson, M. 1998, ApJ, 498, 106

Makarov, D., & Karachentsev, I. 2011, MNRAS, 412, 2498

Martin, A. M., Giovanelli, R., Haynes, M. P., et al. 2009, ApJS, 183, 214

Martin, A. M., Papastergis, E., Giovanelli, R., et al. 2010, ApJ, 723, 1359

Martin, D. C., Fanson, J., Schiminovich, D., et al. 2005, ApJ, 619, L1

Martínez-Delgado, D., Läsker, R., Sharina, M., et al. 2016, AJ, 151, 96

Masters, C. E. 2005, PhD thesis, University of Missouri - Kansas City

Matsuoka, Y., Ienaka, N., Oyabu, S., Wada, K., & Takino, S. 2012, AJ, 144, 159

McConnachie, A. W. 2012, AJ, 144, 4

McGaugh, S. S. 2005, ApJ, 632, 859

—. 2012, AJ, 143, 40

McGaugh, S. S., & de Blok, W. J. G. 1997, ApJ, 481, 689

—. 1998, ApJ, 499, 41

McGaugh, S. S., & Schombert, J. M. 2014, AJ, 148, 77

McGaugh, S. S., Schombert, J. M., & Bothun, G. D. 1995, AJ, 109, 2019

McGaugh, S. S., Schombert, J. M., Bothun, G. D., & de Blok, W. J. G. 2000, ApJ, 533, L99

McMullin, J. P., Waters, B., Schiebel, D., Young, W., & Golap, K. 2007, in Astronomical Society of the Pacific Conference Series, Vol. 376, Astronomical Data Analysis Software and Systems XVI, ed. R. A. Shaw, F. Hill, & D. J. Bell, 127

McQuinn, K. B. W., Cannon, J. M., Dolphin, A. E., et al. 2014, ApJ, 785, 3

—. 2015, ApJ, 802, 66

Merritt, A., van Dokkum, P., Danieli, S., et al. 2016, ApJ, 833, 168

Mihos, J. C., Durrell, P. R., Ferrarese, L., et al. 2015, ApJ, 809, L21

Minchin, R., Davies, J., Disney, M., et al. 2005, ApJ, 622, L21

Mo, H. J., Mao, S., & White, S. D. M. 1998, MNRAS, 295, 319

Morrissey, P., Conrow, T., Barlow, T. A., et al. 2007, ApJS, 173, 682

Mould, J. R., Huchra, J. P., Freedman, W. L., et al. 2000, ApJ, 529, 786

Mundell, C. G., James, P. A., Loiseau, N., Schinnerer, E., & Forbes, D. A. 2004, ApJ, 614, 648

Mundell, C. G., Pedlar, A., Axon, D. J., Meaburn, J., & Unger, S. W. 1995, MNRAS, 277, 641

Murphy, E. J., Condon, J. J., Schinnerer, E., et al. 2011, ApJ, 737, 67

Navarro, J. F., Frenk, C. S., & White, S. D. M. 1997, ApJ, 490, 493

Nidever, D. L., Ashley, T., Slater, C. T., et al. 2013, ApJ, 779, L15

Obreschkow, D., Glazebrook, K., Kilborn, V., & Lutz, K. 2016, ApJ, 824, L26

Papastergis, E., Adams, E. A. K., & Romanowsky, A. J. 2017, ArXiv e-prints, arXiv:1703.05610

Papastergis, E., Cattaneo, A., Huang, S., Giovanelli, R., & Haynes, M. P. 2012, ApJ, 759, 138

Papastergis, E., Martin, A. M., Giovanelli, R., & Haynes, M. P. 2011, ApJ, 739, 38

Peng, E. W., & Lim, S. 2016, ApJ, 822, L31

Postman, M., & Geller, M. J. 1984, ApJ, 281, 95

Radburn-Smith, D. J., Roškar, R., Debattista, V. P., et al. 2012, ApJ, 753, 138

Rand, R. J. 1994, A&A, 285

Rhode, K. L., Salzer, J. J., Haurberg, N. C., et al. 2013, AJ, 145, 149

Roberts, M. S., & Haynes, M. P. 1994, ARA&A, 32, 115

Román, J., & Trujillo, I. 2017a, MNRAS, 468, 703

—. 2017b, MNRAS, 468, 4039

Rosenberg, J. L., & Schneider, S. E. 2003, ApJ, 585, 256

Rudick, C. S., Mihos, J. C., Harding, P., et al. 2010, ApJ, 720, 569

Saintonge, A. 2007, AJ, 133, 2087

Sakai, S., Madore, B. F., Freedman, W. L., et al. 1997, ApJ, 478, 49

Salim, S., Rich, R. M., Charlot, S., et al. 2007, ApJS, 173, 267

Salpeter, E. E., & Hoffman, G. L. 1995, ApJ, 441, 51

Sancisi, R., & Allen, R. J. 1979, A&A, 74, 73

Sancisi, R., Broeils, A., Kamphuis, J., & van der Hulst, T. 1990, Observed gas infall into galaxies., ed. R. Wielen, 304–307

Sancisi, R., Fraternali, F., Oosterloo, T., & van der Hulst, T. 2008, A&A Rev., 15, 189

Sandage, A. 1976, AJ, 81, 954

Sault, R. J., Teuben, P. J., & Wright, M. C. H. 1995, in Astronomical Society of the Pacific Conference Series, Vol. 77, Astronomical Data Analysis Software and Systems IV, ed. R. A. Shaw, H. E. Payne, & J. J. E. Hayes, 433

Schaye, J. 2004, ApJ, 609, 667

Schiminovich, D., Catinella, B., Kauffmann, G., et al. 2010, MNRAS, 408, 919

Schlafly, E. F., & Finkbeiner, D. P. 2011, ApJ, 737, 103

Schlegel, D., Finkbeiner, D., & Davis, M. 1998, in Wide Field Surveys in Cosmology, ed. S. Colombi, Y. Mellier, & B. Raban, 297

Schombert, J., Maciel, T., & McGaugh, S. 2011, Advances in Astronomy, 2011, 143698

Schombert, J., & McGaugh, S. 2014, PASA, 31, e036

Schombert, J. M., Bothun, G. D., Schneider, S. E., & McGaugh, S. S. 1992, AJ, 103, 1107

Serra, P., Oosterloo, T., Morganti, R., et al. 2012, MNRAS, 422, 1835

Serra, P., Koribalski, B., Duc, P.-A., et al. 2013, MNRAS, 428, 370

Serra, P., Koribalski, B., Kilborn, V., et al. 2015, MNRAS, 452, 2680

Shostak, G. S., & Allen, R. J. 1980, A&A, 81, 167

Smith Castelli, A. V., Faifer, F. R., & Escudero, C. G. 2016, A&A, 596, A23

Stierwalt, S., Haynes, M. P., Giovanelli, R., et al. 2009, AJ, 138, 338

Stil, J. M., & Israel, F. P. 2002, A&A, 389, 29

Suess, K. A., Darling, J., Haynes, M. P., & Giovanelli, R. 2016, MNRAS, 459, 220

Swaters, R. A., van Albada, T. S., van der Hulst, J. M., & Sancisi, R. 2002, A&A, 390, 829

Szabó, G. M., Sárneczky, K., Vinkó, J., et al. 2003, A&A, 408, 915

Tago, E., Einasto, J., Saar, E., et al. 2008, A&A, 479, 927

Taylor, E. N., & Webster, R. L. 2005, ApJ, 634, 1067

Teich, Y. G., McNichols, A. T., Nims, E., et al. 2016, ApJ, 832, 85

Tonry, J. L., Dressler, A., Blakeslee, J. P., et al. 2001, ApJ, 546, 681

Toomre, A., & Toomre, J. 1972, ApJ, 178, 623

Toribio, M. C., Solanes, J. M., Giovanelli, R., Haynes, M. P., & Martin, A. M. 2011, ApJ, 732, 93

Trujillo, I., & Fliri, J. 2016, ApJ, 823, 123

Trujillo, I., Roman, J., Filho, M., & Sánchez Almeida, J. 2017, ApJ, 836, 191

Tully, R. B. 1987, ApJ, 321, 280

Tully, R. B., & Fisher, J. R. 1987, Atlas of Nearby Galaxies

Turner, E. L., & Gott, III, J. R. 1976, ApJS, 32, 409

van der Burg, R. F. J., Muzzin, A., & Hoekstra, H. 2016, A&A, 590, A20

van Dokkum, P., Abraham, R., Brodie, J., et al. 2016, ApJ, 828, L6

van Dokkum, P. G., Abraham, R., Merritt, A., et al. 2015, ApJ, 798, L45

van Eymeren, J., Marcelin, M., Koribalski, B. S., et al. 2009, A&A, 505, 105

van Zee, L., Haynes, M. P., Salzer, J. J., & Broeils, A. H. 1997, AJ, 113, 1618

Verde, L., Oh, S. P., & Jimenez, R. 2002, MNRAS, 336, 541

Verdes-Montenegro, L., Yun, M. S., Williams, B. A., et al. 2001, A&A, 377, 812

Walker, L. M., Johnson, K. E., Gallagher, S. C., et al. 2016, AJ, 151, 30

Walter, F., Brinks, E., de Blok, W. J. G., et al. 2008, AJ, 136, 2563

Wang, J., Koribalski, B. S., Serra, P., et al. 2016, MNRAS, 460, 2143

Wang, J., Kauffmann, G., Józsa, G. I. G., et al. 2013, MNRAS, 433, 270

Wang, L., Dutton, A. A., Stinson, G. S., et al. 2015, MNRAS, 454, 83

Warmels, R. H. 1988, A&AS, 72, 427

Warren, B. E., Jerjen, H., & Koribalski, B. S. 2004, AJ, 128, 1152

—. 2007, AJ, 134, 1849

Williams, R. E., Blacker, B., Dickinson, M., et al. 1996, AJ, 112, 1335

Witt, A. N., Mandel, S., Sell, P. H., Dixon, T., & Vijh, U. P. 2008, ApJ, 679, 497

Wright, E. L., Eisenhardt, P. R. M., Mainzer, A. K., et al. 2010, AJ, 140, 1868

Yagi, M., Koda, J., Komiyama, Y., & Yamanoi, H. 2016, ApJS, 225, 11

Yang, Y., Hammer, F., Fouquet, S., et al. 2014, MNRAS, 442, 2419

York, D. G., Adelman, J., Anderson, Jr., J. E., et al. 2000, AJ, 120, 1579

Yoshii, Y., Kobayashi, Y., Minezaki, T., Koshida, S., & Peterson, B. A. 2014, ApJ, 784, L11

Young, M. D., Gopu, A., Hayashi, S., & Cox, J. A. 2013, in Astronomical Society of the Pacific Conference Series, Vol. 475, Astronomical Data Analysis Software and Systems XXII, ed. D. N. Friedel, 337

Young, M. D., Kotulla, R., Gopu, A., & Liu, W. 2014, in Proc. SPIE, Vol. 9152, Software and Cyberinfrastructure for Astronomy III, 91522U

Yozin, C., & Bekki, K. 2015, MNRAS, 452, 937

Yun, M. S., Ho, P. T. P., & Lo, K. Y. 1994, Nature, 372, 530

Zaritsky, D. 2017, MNRAS, 464, L110

Zibetti, S., Charlot, S., & Rix, H.-W. 2009, MNRAS, 400, 1181

Zucker, D. B., Belokurov, V., Evans, N. W., et al. 2006, ApJ, 650, L41